Peter Krabb, BSc

Sub-wavelength structured metal films for applications in organic optoelectronic devices

MASTER THESIS

For obtaining the academic degree
Diplom-Ingenieur

Master Programme of
Technical Physics

Graz University of Technology

Supervisor:

Ao.Univ.-Prof. Dipl.-Ing. Dr.techn. Emil J. W. List

Institute of Solid State Physics

Graz, Dezember 2011

Deutsche Fassung:
Beschluss der Curricula-Kommission für Bachelor-, Master- und Diplomstudien vom 10.11.2008
Genehmigung des Senates am 1.12.2008

EIDESSTATTLICHE ERKLÄRUNG

Ich erkläre an Eides statt, dass ich die vorliegende Arbeit selbstständig verfasst, andere als die angegebenen Quellen/Hilfsmittel nicht benutzt, und die den benutzten Quellen wörtlich und inhaltlich entnommene Stellen als solche kenntlich gemacht habe.

Graz, am …… ……..
(Unterschrift)

Englische Fassung:

STATUTORY DECLARATION

I declare that I have authored this thesis independently, that I have not used other than the declared sources / resources, and that I have explicitly marked all material which has been quoted either literally or by content from the used sources.

…… ……..
date (signature)

Acknowledgements

First of all I would like to thank my supervisor Prof. Emil J. W. List for giving me the opportunity to work in his team at the NanoTecCenter Weiz and for his creative guiding ideas.

I want to thank the whole NanoTecCenter team for the great time and cooperativeness.

I would like to thank Stefan Sax for various discussions concerning the e-Line and experimental issues. Special thanks goes to Alexander Blümel for the various AFM measurements and other inputs concerning the e-Line.

Thanks to Gernot Mauthner for teaching me the theoretical background of bulk heterojunction solar cells. Roman Trattnig and Monika Jäger for building the OSCs with the plasmonic structure inside and especially Markus Seidl for showing me how to buid OSCs in the laboratory.

I also have to thank Sebastian Schuh, Sebastian Nau, Kerstin Schmoltner and Johannes Kofler for various discussions and help. Moreover I have to thank Hannes Holl for the car-pool and the administrative issues.

Last but not least I want to thank Agustina for her limitless love and understanding, supporting me even when I had bad mood because things were not working well.

Abstract

Periodically sub-wavelength structured films show special optical properties. In particular thin perforated metal films are known for Extra Ordinary Transmission (EOT) due to contributions of surface plasmons. A periodic arrangement of holes in the metal film allows the excitation of surface plasmons, with the property of strong electric fields in the vicinity of the surface. This can be used for light management to improve in- or outcoupling of light to thin film devices as Organic Solar Cells (OSC) or Organic Light Emitting Diodes (OLED).

The first part of this thesis treats the fabrication of sub-wavelength structured metal films with a lift-off technique. Therefore negative resists are structured via Electron Beam Lithography (EBL). The main issue here is the optimization concerning the exposure time of the EBL system leading to a special fast exposure for sub-μm hole arrays. Structuring areas over 3x3mm^2 in about 10h is possible. Gold films perforated with different periodic holes arrays, with periods down to 400nm and hole diameters down to 100nm as well as 2 dim. photonic crystals with these scales were prepared.
The second part of this thesis treats the characterization of structured and unstructured gold/chrome films performed by atomic force microscopy, scanning electron microscopy and optical spectroscopy. Different thick gold films and the influence of the chrome adhesion layer as well as variable geometric values of periodic hole arrays in metal films are investigated by transmission measurements. Optical thin structured metal films show resonances depending on the period of the array. In optical thick structured metal films EOT was measured and assigned to plasmonic resonances excited by the array. The optical properties of the metal films are also investigated in combination with the low-band-gap polymer PTB7. A 30nm thin gold film gets more transparent at certain wavelength if coated with a layer of PTB7. Structured gold films coated with PTB7 show a similar behavior at increased wavelength. Further photoluminescence is enhanced with a gold film in contact with the polymer. This enhanced signal is produced mainly by diffuse reflection at the metal. For sub-wavelength structured metals coated with PTB7 the photoluminescence further increases. It shows that periodic structured metal films can change the photo physical properties of proximate molecules and this could be used in OLEDs. Further the positive effect of plasmonic nanostructures incorporated in OSCs is demonstrated. The increase in power conversation efficiencies points out the potential and importance of further investigations in this field.

Kurzfassung

Im Sub-Wellenlängenbereich strukturierte Filme weisen spezielle optische Eigenschaften auf. Dünne perforierte Metallfilme sind bekannt für erhöhte optische Transmission (EOT) durch Beiträge von Oberflächen Plasmonen. Eine periodische Anordnung der Löcher im Metall ermöglicht die Anregung von Oberflächen Plasmonen mit der Eigenschaft von starken elektrischen Feldern in der Nähe der Oberfläche. Dies kann für eine Licht Steuerung zur verbesserten Ein- oder Auskopplung von Licht in Dünnschichtbauelementen wie organischen Solarzellen (OSC) oder organischen Licht emittierenden Dioden (OLED) genutzt werden.

Der erste Teil dieser Masterarbeit behandelt die Herstellung von Sub-Wellenlängen strukturierter Metallfilme durch eine lift-off Technik. Dafür werden negative Photolacke mittels Elektronenstrahl Lithographie (EBL) strukturiert. Den Kernpunkt hierbei bildet die Optimierung der Belichtungszeit am EBL System, welche zu einer sehr schnellen Belichtung für sub-μm Loch Arrays führt. Dadurch wird die Strukturierung von Flächen über 3x3mm^2 in etwa 10h möglich. Gold Schichten perforiert mit verschiedenen periodischen Loch Arrays mit minimal 400nm Periode und 100nm Lochdurchmesser, sowie 2dim. photonische Kristalle mit diesen Abmessungen wurden hergestellt.
Der zweite Teil dieser Masterarbeit behandelt die Charakterisierung von strukturierten und unstrukturierten Gold/Chrom Schichten mittels Rasterkraftmikroskop, Rasterelektronenmikroskop und optischer Spektroskopie. Verschieden dicke Gold Schichten und der Einfluss der Chrome Adhäsionsschicht sowie verschiedene Geometrien der periodischen Loch Arrays werden mittels Transmissionsmessungen untersucht. Strukturierte, optisch dünne Metallschichten weisen Resonanzen in Abhängigkeit von der Periode des Arrays auf. In optisch dicken strukturierten Metallschichten wurde EOT gemessen und plasmonischen Resonanzen zugeordnet die durch das Array angeregt werden. Die optischen Eigenschaften der metallischen Schichten werden auch in Kombination mit PTB7, einem halbleitenden Polymer mit kleiner Bandlücke untersucht. Eine 30nm dünne Gold Schicht wird bei gewissen Wellenlängen transparenter, wenn sie mit dem Polymer PTB7 beschichtet ist. Strukturierte Goldschichten weisen ein ähnliches Verhalten bei vergrößerten Wellenlängen auf. Des Weiteren erhöht eine Gold Schicht in Verbindung mit dem Polymer die Photolumineszenz. Dieses verstärkte Signal wird hauptsächlich durch diffuse Reflexion am Metall erzeugt. Wenn das Metall zusätzlich strukturiert ist, wird die Photolumineszenz weiter verstärkt. Das zeigt, dass periodisch strukturierte Metalle die photo-physikalischen Eigenschaften von benachbarten Molekülen ändern können. Dies könnte in OLEDs Anwendung finden. Zusätzlich wird der positive Effekt von plasmonischen Nanostrukturen in OSCs gezeigt. Die Effizienzsteigerung zeigt das Potential dieser Anwendung und die Wichtigkeit von weiterführenden Experimenten.

Table of Contents

List of Abbreviations

Ag	Silver
AIT	Absorption Induced Transparency
Al	Aluminum
Au	Gold
BHJ	Bulk Heterojunction
Cr	Chrome
EBL	Electron Beam Lithography
EOT	Extraordinary Optical Transmission
FF	Fill Factor
IPCE	Incident Photon to Charge Carrier Efficiency
IQE	Internal Quantum Efficiency
IS	Integrating Sphere
ITO	Indium Thin Oxide
LSP	Localized Surface Plasmon
NIR	Near Infrared
NTC	NanoTecCenter
OLED	Organic Light Emitting Diode
OSC	Organic Solar Cell
PEB	Post Exposure Bake
PhC	Photonic Crystal
PL	Photoluminescence
RDE	Radiative Decay Engineering
SE	Secondary Electrons
SEM	Scanning Electron Microscope
SP	Surface Plasmon
SPP	Surface Plasmon Polariton
UHV	Ultra High Vacuum
UV	Ultraviolet
VIS	Visible
WF	Write Field

Chapter 1

Motivation and Introduction

Nanotechnology is the study of manipulating matter down to the nm scale. With the nowadays available methods e.g. ultraviolet or X-ray lithography, electron beam lithography, focused ion beam milling or nanoimprint lithography, sub-100nm patterning is possible. For this work the method of electron beam lithography was used to fabricate sub-wavelength structures. The optical properties of sub-wavelength structured metal films have been intensively investigated, since Extraordinary Optical Transmission (EOT) was reported by Ebbesen *et al.* in 1998 [1]. The unexpected high transmission in the optical regime is supported by electromagnetic modes bound to the metal surface known as Surface Plasmon Polaritons (SPPs) [2].

The aim of this work is to produce sub-wavelength hole arrays in metal films via Electron Beam Lithography (EBL) and a lift-off technique. This periodic structure enables the excitation of SPPs by photons. SPPs are known for high electrical fields near the surface, offering a broad spectrum of applications. These can be molecular sensing applications [3], enhanced and high fidelity raman spectroscopy [4] or enhanced fluorescence spectroscopy [5]. Further efficiency enhancement of Organic Light Emitting Diodes (OLED) with a sub-wavelength structured cathode [6] and surface plasmon enhanced photoconversion in Organic Solar Cells (OSC) [7] are feasible as well.

In this work these arrays are structured in a macroscopic area to investigate them in combination with thin-film photovoltaic cells. Thin-film technology has an enormous potential in reducing the cost of photovoltaic devices. Especially OSCs are of interest because of their advantages of low cost of fabrication, easy solution based processability and mechanical flexibility [8]. The sub-wavelength structured metal films should serve as transparent electrodes. More precisely they are used as anode for OSCs, primarily to replace Indium Tin Oxide (ITO), the standard transparent electrode. ITO limits reliability and costs of OSCs because it is a brittle and expensive material [9]. Compared to noble metals

it has a low conductivity of $10^4 \frac{S}{cm}$ [10], which increases ohmic losses for large area single cells [11]. Further Indium is a rare metal and is limited in the earth crust. Without a good recycling infrastructure in the future, indium price explosion and shortage are expected [12]. Price and performance are the key parameters for successful commercialization of OSCs, which makes the replacement of ITO by a cheaper and high performance alternative important.

Moreover the poor conductivity of organic semiconducting materials makes a tradeoff between collection of photogenerated charge carriers and sufficient light absorption in the active material necessary. Photon management, which refers to the control of photon propagation and the energy distribution in the active layer, can increase the absorption. Plasmonics has emerged as a promising route to advanced photon management [13]. Light trapping with metallic nanostructures, where incoming light scatters and excites surface plasmons (**Figure 1.1**) is a possibility to improve light incoupling into the active layer.

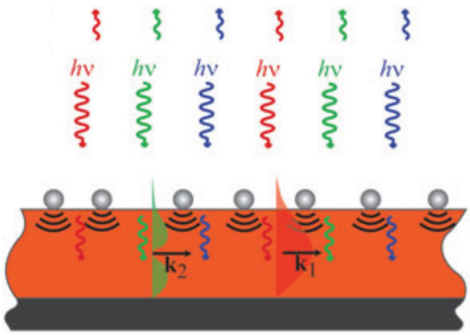

Figure 1.1 – Metal nanostructure on the device surface can scatter light and enhance photo conversion in a solar cells. Taken from [13].

Sub-wavelength structured metal films are promising candidates for plasmonic electrodes, which can replace ITO as transparent electrode material and additionally enhance light incoupling into the active layer and therefore efficiencies of organic photovoltaic devices.

Based on the fundamentals of electrodynamics, surface plasmons with its properties are introduced in chapter 2. The following chapter treats the fundamentals of electron beam lithography and the lift-off technique as well as the sample preparation and the characterization methods. In chapter 4 the fabrication of sub-wavelength structured films for plasmonic electrodes through a lithographic process is explained. This includes the optimization of the exposure time on the EBL system, two different lift-off methods and a thermal treatment step. In chapter 5 the results of topographical and optical characterization will be presented. The application of plasmonic structures on OSCs will be treated in chapter 6 and 8.

Chapter 2

Theoretical Aspects

This chapter summarizes the theoretical fundamentals for this work. First the idea of resonant incoupling by means of structured electrodes in an organic solar cell is presented. Starting from the Maxwell equations, the bulk plasma frequency and the dielectric function of a metal are deduced and compared with experimental data from literature for gold and chrome. The following sections introduce surface plasmons on flat surfaces as well as localized on nanoparticles. When photons couple with surface plasmons a hybrid wave is excited called Surface Plasmon Polariton (SPP). The dispersion relation and an insight to typical length scales and coupling mechanism of SPPs will be given. Finally the resonance wavelength of SPPs on sub-wavelength hole arrays is deduced.

2.1 Resonant light incoupling into the active layer

Photon management can improve the incoupling of light into the active layer. This should be possible with a structured metal electrode for OSC. Adjusting the geometrical factors of a sub-wavelength hole array in a metal film changes the transmission property. Due to the periodicity of the array, resonances are excited. If this resonances overlap with the resonances of the molecules in the active layer a resonant incoupling of light should be possible.

There is experimental evidence that nanoparticles embedded between the ITO and the active layer enhance efficiency. Incident light excite Localized Surface Plasmons (LSP) on the nanoparticle. The strong local enhancement of the electromagnetic field surrounding the nanoparticle increases the rate of exciton generation or exciton dissociation [14, 15, 16]. Sub-wavelength hole arrays can excite SPPs. In the holes there are localized modes present like the LSP on nanoparticles [17]. This localized modes can provide the same effect as the aforementioned nanoparticles.

2.2 Maxwell's equations

The theoretical framework for all electromagnetic phenomena is given by the Maxwell's equations. These fundamental equations describe electromagnetic fields and how they evolve over time. The differential form in matter is the following:

$$\nabla \cdot \mathbf{D} = \rho_f \tag{2.1}$$

$$\nabla \cdot \mathbf{B} = 0 \tag{2.2}$$

$$\nabla \times \mathbf{E} = -\frac{\partial \mathbf{B}}{\partial t} \tag{2.3}$$

$$\nabla \times \mathbf{H} = \frac{\partial \mathbf{D}}{\partial t} + \mathbf{j}_f \tag{2.4}$$

$\mathbf{E}$ and $\mathbf{H}$ are the electric and magnetic field intensities. ρ_f is the free charge density and $\mathbf{j}_f$ is the free current density with the distinction of free (conduction band) and bound (valence band) charge carrier. The other parameters $\mathbf{D}$ and $\mathbf{B}$, are the electric flux density and the magnetic flux density. They are connected to the fields like:

$$\mathbf{D} = \epsilon_0 \mathbf{E} + \mathbf{P} \tag{2.5}$$

$$\mathbf{B} = \mu_0 \mathbf{H} + \mu_0 \mathbf{M} \tag{2.6}$$

Where $\mathbf{P}$ is the polarization and $\mathbf{M}$ is the magnetization. The electrical and magnetic constants are ϵ_0 the permittivity and μ_0 the permeability of free space. A polarization is caused by an electrical field and the magnetization is caused by a magnetic field, this correlation has to be described with a proper model. Fortunately in most substances a linear correlation is a sufficient accurate description. This means for the electric part, that the polarization $\mathbf{P}$ is proportional to the electric field $\mathbf{E}$:

$$\mathbf{P} = \epsilon_0 \chi_e \mathbf{E} \tag{2.7}$$

With χ_e the electric susceptibility of a material. This simplifies (2.5) to

$$\mathbf{D} = \epsilon \mathbf{E} \tag{2.8}$$

With ϵ the dielectric function being:

$$\epsilon = (1 + \chi_e)\epsilon_0 \tag{2.9}$$

On the other hand the dielectric function is defined as:

$$\epsilon = \epsilon_r \epsilon_0 \tag{2.10}$$

2.3 Plasma frequency and dielectric function of a metal

Understanding the optical properties of metals, means modeling the dielectric function by means of a solid state theory. The first theory and simplest model was based on kinetic gas theory developed by Drude who assumed the electrons to act like a free electron gas. The electrons are treated like a ideal gas, this means they are independent and quasi-free dot charges. These charges can be accelerated by an applied field and damped by collisions. This damping is incorporated by a damping constant Γ and can be taken as the reciprocal value of the electron relaxation time T, which is the time between two scatter events of an electron. Later Sommerfeld incorporated corrections coming from the Pauli-exclusion principle, considering only electrons near the Fermi level, because deeper lying electrons are not allowed to change their electronic state. Further the band structure of matter was respected by assigning the electron an effective mass m*.

To derive the plasma frequency and the dielectric function the starting point is the microscopic equation of a moving electron. An applied electric field $E = E_0 \cdot e^{-i\omega t}$ accelerates the electrons which have the mass m_e and the charge e. The conduction electrons are quasi-free which means there is no restoring force and the motion is only damped by scattering, described by the differential equation

$$\frac{\partial^2 x}{\partial t^2} + \Gamma \frac{\partial x}{\partial t} = \frac{e}{m_e} E_0 \cdot e^{-i\omega t} \tag{2.11}$$

The solution of this differential equation with an exponential ansatz for x gives:

$$x = \frac{e}{m_e} \frac{E_0}{\omega^2 + i\Gamma\omega} \tag{2.12}$$

To come from this microscopic equations of one electron to the macroscopic property, first we identify the dipole moment of one electron $p = -ex$. The dipole moment multiplied with the electron density n gives the macroscopic polarization $P = np$. With the before stated expressions (2.5), (2.8) and (2.10) the dielectric function can be obtained:

$$\epsilon_r(\omega) = 1 - \frac{ne^2}{m_e \epsilon_0} \frac{1}{\omega^2 + i\Gamma\omega} \tag{2.13}$$

Where the plasma frequency w_p can be identified:

$$\omega_p^2 = \frac{ne^2}{m_e \epsilon_0} \tag{2.14}$$

This is the eigenfrequency of an electron gas without any damping ($\Gamma = 0$) assumed. Since the conduction electrons in a metal are quasi free this plasma frequency describes well the transition where the electrons are not able anymore to follow the applied electric field. This

means by illuminating a metal with light of a higher frequency than ω_p, that the photons cannot be absorbed and the metal gets transparent. For metals this frequency is in the UV spectral range. The dielectric function is split into real and imaginary part ($\epsilon = \epsilon' + i\epsilon''$) and for small damping ($w \gg \Gamma$) it simplifies to:

$$\epsilon(\omega) \approx 1 - \frac{\omega_p^2}{\omega^2} + i\Gamma\frac{\omega_p^2}{\omega^3} \tag{2.15}$$

To determine the dielectric function experimentally, reflection and transmission measurements or ellipsometry can be done. Thereby first the optical constants, the refractive index n and the extinction coefficient k have to be obtained. Together they form the complex refractive index:

$$\tilde{n} = n + ik \tag{2.16}$$

The complex dielectric function $\epsilon(\omega)$ in a non magnetic medium ($\mu_r = 1$) is connected with the complex refractive index:

$$\epsilon(\omega) = \tilde{n}^2 \tag{2.17}$$

This leads to the connection of the observable optical constants with the real and imaginary part of the dielectric function:

$$\epsilon' = n^2 - k^2 \tag{2.18}$$

$$\epsilon'' = 2nk \tag{2.19}$$

Experimental data of the optical constants from reflection and transmission measurements for thin films are taken from [18] for gold and from [19] for chrome (**Figure 2.1**).

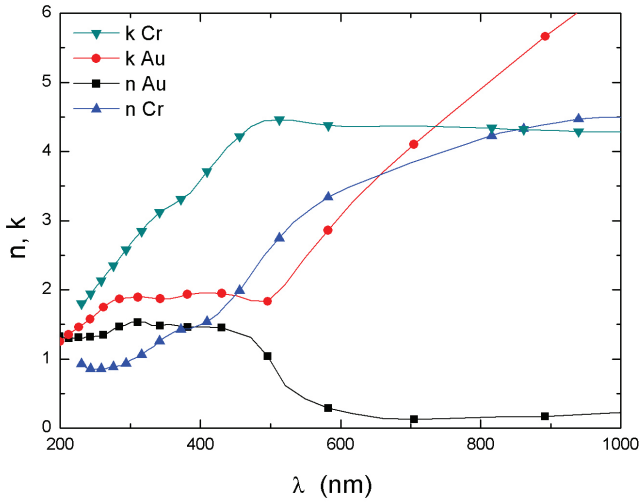

Figure 2.1 – Refractive index n and extinction coefficient k for gold and chrome with the data from [18] for gold and from [19] for chrome.

The real and the imaginary part of the dielectric function are calculated with (2.18) and (2.19) from the optical constants. The dielectric functions are shown in **Figure 2.2**.

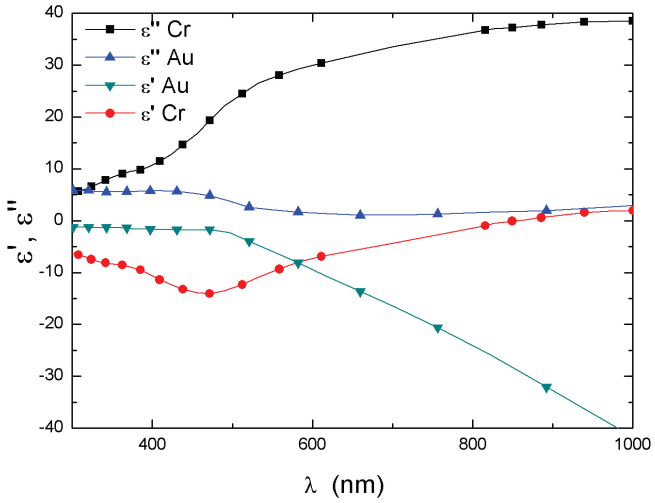

Figure 2.2 – Real ϵ' and imaginary part ϵ'' of the dielectric function for gold and chrome calculated from the optical constants from **Figure 2.1**.

The comparison of the quite simple Drude-Sommerfeld model with the experimental data is done by using the dielectric function (2.15) for gold. The energy of the plasma frequency of gold was taken as $\hbar w_p$=9.01eV the damping constant was set to $\Gamma = T^{-1}$ with $T = 30 \cdot 10^{-15}$ the relaxation time calculated from the Fermi velocity v_F and the mean free path l_f in gold, all values taken from [52].

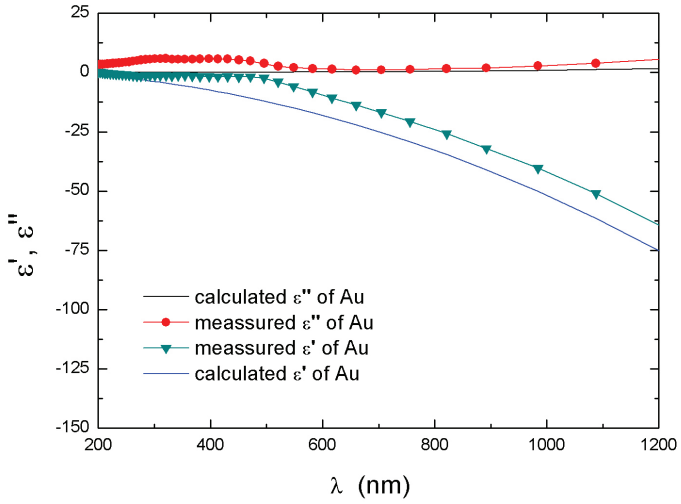

Figure 2.3 – Comparison of the calculated dielectric function of gold with the Drude-Sommerfeld model (2.15) and experimental data from literature.

The discrepancy between the experimental data and the Drude-Sommerfeld model illustrated in **Figure 2.3** in the visible spectral range can be assigned to interband transitions which occur from filled d-bands into the sp conduction bands at a maximum wavelength of 539nm [18]. The simple Drude-Sommerfeld model doesn't account the specific contribution of the valence band electrons.

2.4 Surface Plasmons (SPs)

The plasma frequency in (2.14) describes a longitudinal plasma oscillation in the bulk. The quasi-particle resulting from quantization of these oscillations is called the *bulk plasmon*. At the plasma frequency all the electrons are oscillating in phase. A metal responds to an electromagnetic wave with frequencies $\omega > \omega_p$ like a dielectric due to the disability of the electrons to follow this fast oscillations. This property is reflected in the real part of the dielectric function (2.15) for a metal, which gets positive and propagating waves are possible.

The different situation at the surface results in the *surface plasmon*. As illustrated in **Figure 2.4** oscillating positive and negative surface charges are present. More precisely these are coherent oscillations of mainly the conduction electrons at the surface. This charge oscillations are accompanied by a mixed transversal and longitudinal electromagnetic field which has its maximum at the interface to the adjacent media [20].

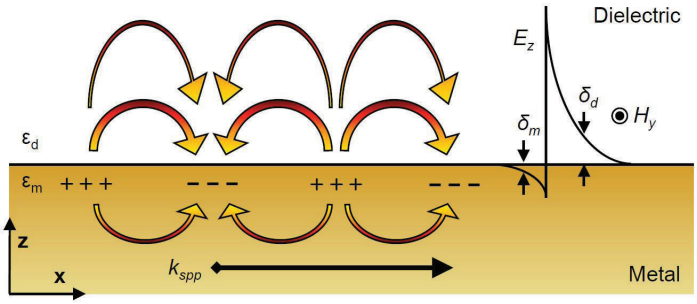

Figure 2.4 – Surface Plasmon located at a metal dielectric interface with ϵ_m and ϵ_d the dielectric functions respectively on the left side and penetration depths of the electric fields into the materials on the right side (taken from [21]).

For the existence of SPs at this interface the real part of the dielectric function has to change sign, which is satisfied for a metal at $\omega < \omega_p$ adjacent to a dielectric material. In this frequency range the dielectric function of the metal has negative and the dielectric a positive value. The resonance frequency for surface plasmons become $\frac{\omega_p}{\sqrt{2}}$ on a flat metal surface exposed to air and $\frac{\omega_p}{\sqrt{1+\epsilon_d}}$ if the interface consists of a metal and a dielectric material with ϵ_d the real part of its dielectric function.

A different situation is present if the surface is not flat. For example on a metallic nanoparticle surrounded by a dielectric material the SPs are localized and cannot propagate away from the nanoparticle due to the fixation to the metallic dielectric interface. That's the reason why this modes are called **Localized Surface Plasmons**. An illustration of such modes is shown in **Figure 2.5**.

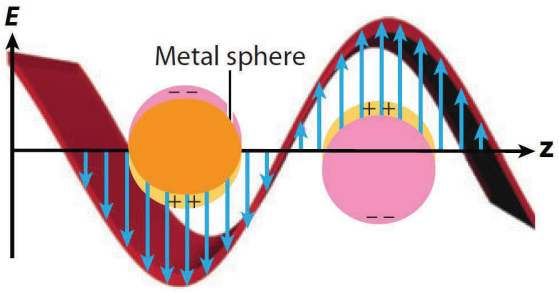

Figure 2.5 – Localized surface plasmons on a metallic nanoparticle excited by free-space light (taken from [22]).

In this work sub-wavelength hole arrays were fabricated. This means nanoscale dielectric holes are present in a metallic film and this is a quite similar situation, where localized modes in this holes are present [17].

2.4.1 Dispersion relation of Surface Plasmon Polaritons (SPPs)

When photons couple with SPs, hybrid waves are excited which are called Surface Plasmon Polaritons (SPPs). The dispersion relation can be deduced from the Maxwell equations by applying appropriate boundary conditions. The mathematical derivation can be found elsewhere [20]. Here only the solution, the dispersion relation is presented:

$$k_x = \frac{\omega}{c}\sqrt{\frac{\epsilon_d \epsilon_m}{\epsilon_d + \epsilon_m}} \tag{2.20}$$

k_x is the value of the wavevector in x-direction, which means along the metal dielectric interface. $\frac{\omega}{c}$ represents the magnitude of the light wave vector with ω the frequency and c the speed of light. ϵ_m and ϵ_d are the dielectric functions of the metal and the dielectric. The dispersion relation (2.20) is ploted in **Figure 2.6**.

There it can be seen that for small k_x the SPP is *photon like* approaching the light line and for large k_x, it is *SP like* approaching the horizontal doted lines representing the surface plasmon resonance frequencies. The dispersion relation is shown for a dielectric with ϵ_d and the case of a metal surface exposed to air ($\epsilon_d = 1$).

Generally the dispersion relation (2.20) is a complex quantity since the dielectric functions

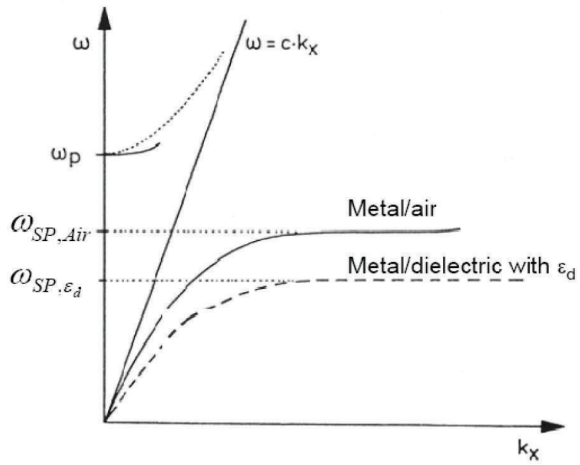

Figure 2.6 – Dispersion relation of Surface Plasmon Polaritons (SPPs) at a metal-air and a metal-dielectric interface. The straight solid line is the dispersion relation of light. (taken from [20] and modified)

are complex. With the assumption of a real ω and ϵ_d and additionally $\epsilon_m'' < |\epsilon_m'|$ for the metal dielectric function $\epsilon_m = \epsilon_m' + i\epsilon_m''$, which is fulfilled for metals with low damping, the dispersion relation for the complex wavevector $k_x = k_x' + ik_x''$ becomes [20]:

$$k_x' = \frac{\omega}{c}\sqrt{\frac{\epsilon_m'\epsilon_d}{\epsilon_m' + \epsilon_d}} \tag{2.21}$$

$$k_x'' = \frac{\omega}{c}\left(\frac{\epsilon_m'\epsilon_d}{\epsilon_m' + \epsilon_d}\right)^{\frac{3}{2}} \frac{\epsilon_m''}{2(\epsilon_m')^2} \tag{2.22}$$

2.4.2 Length scales for SPPs

For the design of devices using SPPs some important length scales have to be known. These length scales provide limits for the device dimensions. The interesting length scales for SPPs are the wavelength λ_{spp} of SPPs, the propagation length δ_{spp} and the penetration depth of the electric fields δ_m into the metal and δ_d into the dielectrics.

The wavelength can be easily obtained from the real part of the SPP wave vector (2.21) by applying $\lambda_{spp} = \frac{2\pi}{k_x'}$:

$$\lambda_{spp} = \lambda_0\sqrt{\frac{\epsilon_d + \epsilon_m'}{\epsilon_d\epsilon_m'}} \tag{2.23}$$

With λ_0 the free space wavelength.
The propagation length δ_{spp} on a smooth surface is the length after which the intensity

decreases to $\frac{1}{e}$ and is given by (2.22) the imaginary part of SPPs [20]:

$$\delta_{spp} = \frac{1}{2k''_x} \tag{2.24}$$

If the metal is low loss and the condition $|\epsilon'_m| \gg |\epsilon_d|$ is satisfied the propagation length can be approximated (more details in [23]):

$$\delta_{spp} \approx \lambda_0 \frac{(\epsilon'_m)^2}{2\pi\epsilon''_m} \tag{2.25}$$

It can be seen that for a long propagation length a large negative value of the real part and a small value of the imaginary part is necessary. This again is satisfied with a low loss metal, that is a noble metal. Here non radiative SPs and a perfect dielectric medium ($\epsilon''_d = 0$) was assumed and the only damping mechanism thus are ohmic losses in the metal.
The penetration depths of the fields in the dielectric δ_d and in the metal δ_m refer again to the distance at which the fields fall to $\frac{1}{e}$ [23]:

$$\delta_d = \frac{\lambda_0}{2\pi} \left| \frac{\epsilon'_m + \epsilon_d}{\epsilon_d^2} \right|^{\frac{1}{2}} \tag{2.26}$$

$$\delta_m = \frac{\lambda_0}{2\pi} \left| \frac{\epsilon'_m + \epsilon_d}{\epsilon_m'^2} \right|^{\frac{1}{2}} \tag{2.27}$$

An illustration of the length scales, spread over several orders of magnitude, can be seen in **Figure 2.7** for silver as metal and air as the dielectric medium.

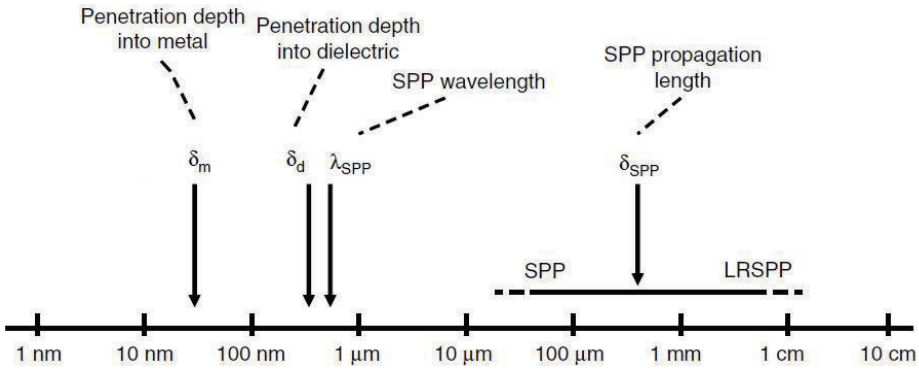

Figure 2.7 – Different length scales for surface plasmon polaritons are indicated on a logarithmic scale for silver as metal and air as dielectric medium. The propagation length for Long Range Surface Plasmon Polaritons (LRSPP) can reach centimeters. (taken from [23] and modified)

2.4.3 Coupling mechanism for SPPs

Surface Plasmons (SPs) can be excited either by electrons or photons. First SPs were recognized excited by electrons in Electron Energy Loss Spectroscopy (EELS) measurements. In contrast, photons as excitation source don't provide enough momentum to excite SPs on a flat surface. In the dispersion relation of SPPs in **Figure 2.6** it can be seen that at a given ω the wavevector of the SPP lies always to the right of the light line $\omega = ck_x$ resulting in a higher quantum mechanical momentum $p = \hbar k$. This means that due to conservation of momentum a coupling mechanism is necessary to excite a SP with a photon.

In the case of thin metals a total internal reflection mode called 'Kretschmann configuration' can be used. This configuration is often used for bimolecular sensing, where the shift of the surface plasmon resonance frequency is detected which occurs due to the change in the dielectric environment [24].

As alternative for thicker metal films or incident light impacting perpendicular to the surface a coupling with a periodic grating like shown in **Figure 2.8** is possible. The x-component of the wavevector, representing the incident light, $k_x = \frac{2\pi}{\lambda} sin\theta$ can be increased by the reciprocal lattice vector of the grating. In this 1 dim example the reciprocal lattice vector is $k_a = \frac{2\pi}{a} m$ with a the period and m the order of the grating.
The momentum match condition to excite a SPP in general is:

$$\vec{k}_{spp} = \vec{k}_x + \vec{k}_a \tag{2.28}$$

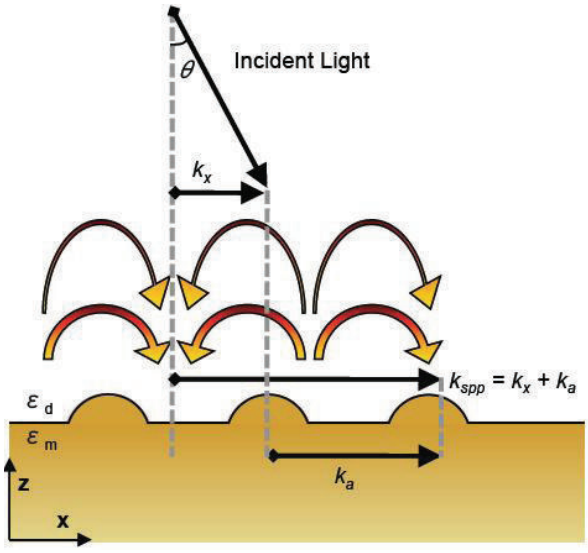

Figure 2.8 – SPP coupling geometry for excitation of SPPs with Photons. Momentum matching condition: $\vec{k}_{spp} = \vec{k}_x + \vec{k}_a$ (taken from [21])

2.4.4 Resonance wavelength of SPPs on sub-wavelength hole arrays

For a square array of nanoholes a formula can be deduced by applying the momentum matching condition (2.28).

Spectra recorded in this work are zero order transmission spectra, that is the incident and the recorded beam are collinear. The samples were placed into the beam perpendicular to the film surface (details in section 3.5.4). This means that the component of the incident wavevector parallel to the film surface $\vec{k}_x$ is zero, which reduces the momentum match condition to:

$$\vec{k}_{spp} = \vec{k}_a \tag{2.29}$$

With $\vec{k}_a$ the reciprocal lattice vector. For a 2 dim square array the absolute value of the reciprocal lattice vector is

$$k_a = \frac{2\pi}{a}\sqrt{n^2 + m^2} \tag{2.30}$$

With a the period, n and m the grating orders. Inserting the dispersion relation (2.20) and the reciprocal lattice vector (2.30) in (2.29) leads to the expression for the wavelength where SPPs are resonant on a 2dim periodic square array:

$$\lambda = \frac{a}{\sqrt{m^2 + n^2}}\sqrt{\frac{\epsilon_m \epsilon_d}{\epsilon_m + \epsilon_d}} \tag{2.31}$$

It has to be noted that this is only a rough estimation, since no metal thickness and the diameter of the holes is taken into account. Only the periodicity of the lattice is considered. Also it has to be kept in mind that the dielectric function ϵ_m is dependent on the wavelength of the exciting radiation ($\epsilon_m = \epsilon_m(\lambda)$). For solving this equation an appropriate model for ϵ_m has to be used, for example the Drude-Sommerfeld expression (2.15) or experimental data can be utilized and the equation (2.31) has to be solved in an iterative manner. In this work the dielectric function from **Figure 2.2** was used.

In section 5.2.2.2 formula (2.31) is applied to a transmission spectrum of a optical thick sub-wavelength structured metal film and agrees with the minimums of the spectrum. The resonances for optical thin metal films did not agree with the measured data in this work due to the simplicity of this model. With thin metal films, a strong interaction of the electromagnetic fields of both surfaces occur [27].

Chapter 3

Experimental methology

The first part of this chapter introduces fundamentals of nanostructuring methods especially the used Electron Beam Lithography (EBL). This includes the sample and its interaction with the electron beam leading to the proximity effect. Furthermore fundamentals concerning the lift-off with EBL will be given and sample preparation will be explained. In the last part the methods to characterize fabricated structures will be mentioned.

3.1 Fabrication methods - Introduction

The discovery and application of semiconducting materials established the field of Electronics. This field had a very fast evolution in the last decades with the aim of miniaturization and integration to minimize material expenses. Investigation and development in structuring methods were additionally pushed. In the standard tool of Microelectronics, which is photolithography the lateral resolution is limited by the wavelength of the used radiation due to diffraction. Using state of the art systems with deep ultraviolet excimer lasers (e.g. ArF:193nm) makes it possible to create structures smaller than 100nm [28]. Such equipment is very complex and expensive. To overcome the diffraction limit, structuring with particles instead of photons is used. Since 1924 when Louis Victor de Broglie postulated the wave-particle duality, which nowadays is a central concept of quantum mechanics, it is known that all matter and not just light have a wave nature. The wavelength λ of matter is called the de-Broglie wavelength and is calculated via the momentum p and the Planck constant h:

$$\lambda = \frac{h}{p} \tag{3.1}$$

Charged particles accelerated in a high-voltage have a higher momentum than photons. This goes along with a shorter de-Broglie wavelength. It follows that the lateral resolution is not limited by diffraction. Limits are present because of big lens errors of electro-magnetic

lenses and in particular because of scattered particles in the sample. However, with particles it is possible to fabricate structures with lateral dimensions down to the nm regime.
Generally Structuring methods can be classified in serial and parallel methods. Serial methods are flexible in terms of changing the exposure pattern, but their serial nature implies very slow processing and therefore they are not applicable for large area production. This means those serial methods will be most likely used where flexibility and precision is needed and not where high output is the goal. There are various methods for sub-wavelength structuring, often employed are the following:

Serial methods:

- Electron Beam Lithography (EBL)
- Focused Ion Beam milling (FIB)

Parallel methods:

- Colloidal lithography with polystyrene spheres
- Stamping and transfer techniques: Nanoimprint or Direct Metal Transfer
- Deep UV lithography

3.2 Electron Beam Lithography (EBL)

In EBL an electron beam is deflected in a patterned fashion across a substrate covered with a polymer film. This film is called the resist and changes its physical properties due to the interaction with the electrons. Thus a selective remove of either exposed or unexposed regions, called the development, is possible.

Advantages of EBL are the beat of the diffraction limit of light and it is a maskless structuring method and therefore it offers a high flexibility in designing patterns. Disadvantages are low throughput i.e. long exposure times for areas $>1\text{mm}^2$ as well as the scattering of electrons in the sample which limits resolution.

3.2.1 Components

The system at the NTC-Weiz is the e-Line system by Raith GmbH. An EBL system consists of a Scanning Electron Microscope (SEM) and a laser interferometric stage (**Figure 3.1**).

Scanning Electron Microscope (SEM):
The electron gun is a Schottky Thermo field emitter that is a thermally assisted field

emission gun. It consists of a tungsten (W) dip covered with Zirconium oxide (ZrO) in order to lower the work function of the dip. Consequently electron emission is enhanced, since the work function is the minimum energy needed to remove an electron from a solid. The whole system is under ultra high vacuum to prevent collisions of the electrons with gas molecules. Different apertures with diameters from 7,5μm to 120μm allow the adjustment of the beam current respectively the spot size of the beam. Since electrons cannot be focused like photons with ordinary lenses because they would be absorbed by the lens material, an electromagnetic-electrostatic lens system deflects the electrons. The latter are charged moving particles and the Lorentz force acts as a deflection force to focus the beam on a spot. The deflection system redirects the beam to scan the sample and Secondary Electrons (SE), backscattered electrons, characteristic x-rays or light are the main signals which can be captured. Since the SEM at the NTC-Weiz is simply equipped with SE detectors, only low energy electrons can be detected. The low energy causes a high interaction probability with matter resulting in a small mean free path of SE in matter. For atoms with a high atomic number like platinum the mean free path is approximately 2nm, for low density ceramics it is approximately 23nm [41]. This means that only SE from the sample surface can be detected.

Laser interferometric stage:
The sample is fixed at the interferometric stage. Here the electron beam can only be deflected to a certain extend (max. 1mm^2). This area is called the Write Field (WF). If the exposed pattern is larger than the WF, the interferometric stage has to be moved to the next field and there again deflect the beam with the deflection system. The interferometric stage has a position accuracy of 2nm.

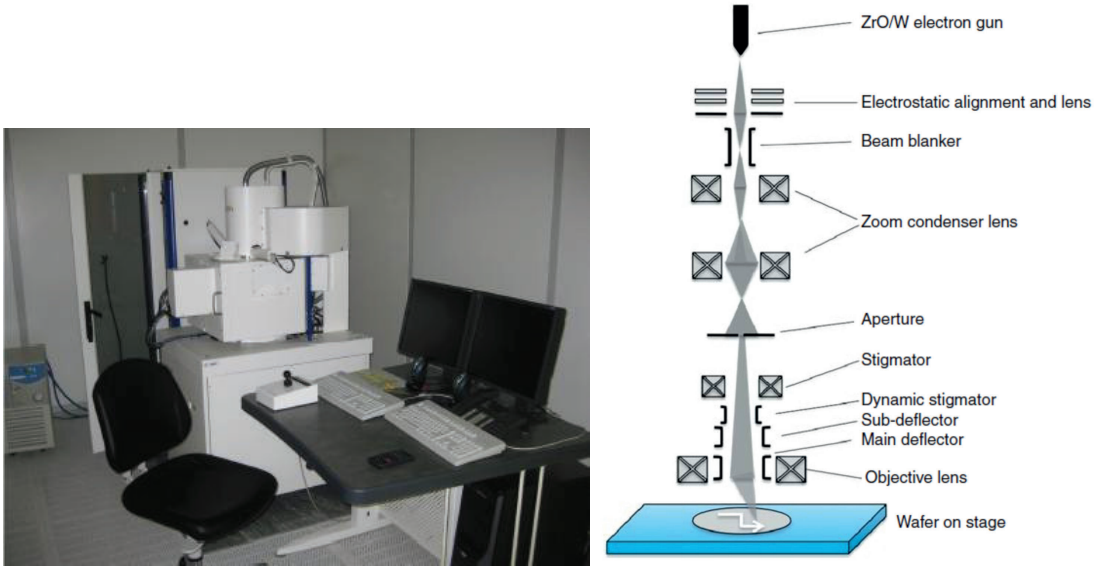

Figure 3.1 – Left: EBL system at the NTC-Weiz (taken from [30]), right: Scematic of a simple EBL column (taken from [32])

3.2.2 Write field alignment and stitching error

The WF exists of a fixed amount of points that can be exposed, but an adjustable size. Consequently the size of the WF determines the resolution. In this work the WF size was usually 100x100μm^2 which leads to a grid of possible exposure points with a distance of 1,6nm. If the pattern extends over various WFs the interferometric stage has to be moved and the WFs have to be stitched together as illustrated in **Figure 3.2**. The stage and the deflected beam are two different coordinate systems. To stitch the WFs precisely together, the transformation between the two coordinate systems has to be known. The system calculates the transformation via a WF alignment with input about pattern positions from the operator. How this is done is explained elsewhere [31]. This WF alignment has to be executed prior to every exposure because the signal to deflect the beam is passing through several electronic components with rounding errors and more or less long term drifts. An automated WF-alignment uses an image recognition software to determine the position of the pattern. Though it is important that the pattern is well pronounced and unique, which can be done by burning contamination dots.

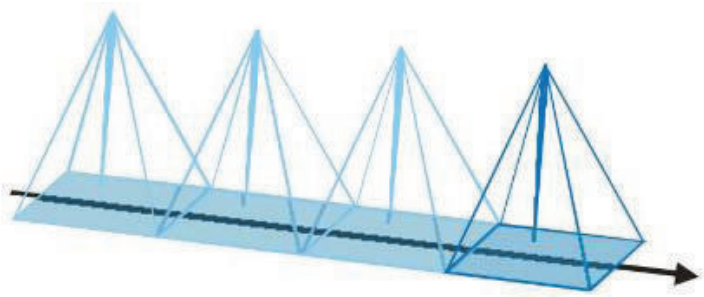

Figure 3.2 – Scematic drawing of stitching write fields together (taken from [36]).

The stitching error is the positional error made by placing one WF next to the other resulting in an overlap of the WFs or space in between. This can be due to bad or inaccurate WF-alignment, charging effects or the thermal drift. For long exposures with a high accuracy the appliance of an automatic WF-alignment during the exposure is a possible software option.

3.2.3 Beam drift

The positional drift of the Raith e-Line system was measured over 16 hours to be about 2μm and therefore a drift of about 2nm/min. Similar results were published for a Raith 150 system, at which the drift was found to be less than 6nm/min with a thermal stability of better than 0,3°C. There the largest drift of >20nm/min was found directly after loading the sample and after a stabilization period the drift was less than 2nm/min [29]. This reflects the importance of sufficient stabilization time for the system. As a rough rule it can be said,

that the system has to stabilize at least 3 days after turning on the electron gun and 1 hour after switching on the acceleration voltage.

3.2.4 Exposure and development of resists

Exposure of a resist in EBL means the deposition of energy by the electron beam. The deposited energy depends on the energy of the electrons i.e. the acceleration voltage and the number of charges applied to a certain area. The number of charges is described by the applied dose. For an area A this is the product of the beam current I and the dwell time t, which is the interaction time of the sample and the beam.

$$D = \frac{I \cdot t}{A} \tag{3.2}$$

D ... applied dose, I ... beam current, t ... dwell time, A ... exposed area

A sample for EBL is a substrate coated with a resist film. To expose small features the aspect ratio (height of resist/lateral elongation) has to be small. Consequently the thickness of the resist should be less than in photolithography. Standard is a resist thicknesses in the sub-μm. Positive and negative resist types are used. The physical process during exposure are cross-linking for exposed areas in a negative resist and a chain scission for these areas in a positive resist. In the following development step polymer chains of molecular weight below some critical value are dissolved. Changed molecular weights due to exposure lead to different development rates. In summary exposed areas of a positive resist get dissolved and with a negative resist only this areas remain after the development step (**Figure 3.3**).

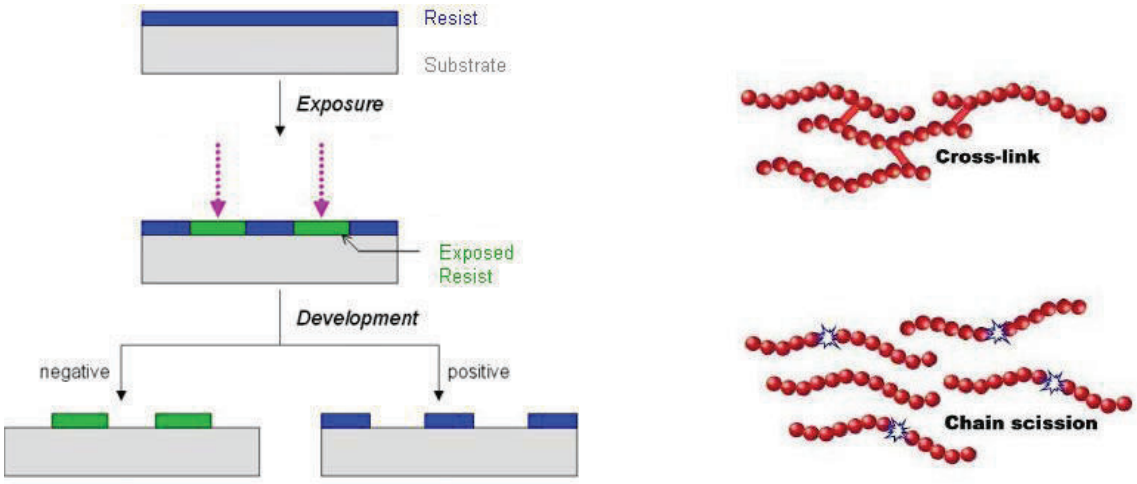

Figure 3.3 – Left: Difference between positive and negative resist (taken from [37] and modified), right: Cross-linking for exposed areas of negative resist and chain scission for positive resist (taken from [38])

3.2.5 Electron - sample interaction

The electrons are accelerated toward the sample (**Figure 3.4**). Penetrating electrons first interact with the resist, that is a low dense material and therefore the main scattering event is *forward scattering*. This is an inelastic interaction resulting in a small scattering angle. If the kinetic energy of the electrons is high enough to transmit the resist, they interact with the substrate. Normally the substrate is a higher dense material, for that reason the main scattering event is *backscattering*. This is an elastic interaction and has a large scattering angle. Especially this backscattered electrons makes the structuring difficult. Areas assumed not to be exposed, get exposed with the long range backscattered electrons.

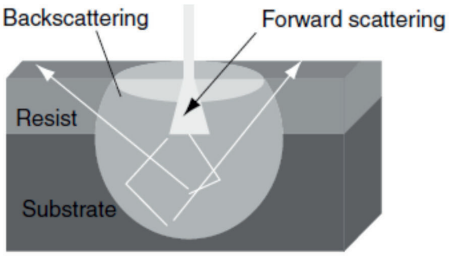

Figure 3.4 – Illustration of the short-range (forward scatter) and long-range (backscatter) interaction of electrons with a resist-coated substrate (taken from [32]).

3.2.6 Proximity Effect

The proximity effect is the result of the electron - sample interaction explained in the last section. Especially the long range backscattered electrons produce a background exposure around the incident beam. This leads to deformations and rounding effects of edges in an exposed object, the so called *Intra Proximity Effect*. If the distance between the exposed objects is smaller than the scattered electrons reach the background exposure of neighboring objects superpose and add up, which is called *Inter Proximity Effect*. In the case of a negative resist if the critical value for the developer is exceeded by this superposition, also areas where no direct exposure was applied, withstand the developing process. In **Figure 3.5** SEM images are presented to demonstrate the intra proximity effect. To the object on the right side, a too high dose was applied leading to this unwanted 'feet' of remaining resist near the substrate to both sides of the exposed area. In the inset the cross section of the object is pictured.

The dashed red line in **Figure 3.6** shows the expected deposited energy in a resist of an electron beam with a Gaussian-shaped intensity cross section. The actual deposited energy, represented by the blue solid line, diverges significantly due to the backscattering of the electrons. The model function of the actual deposited energy can be approximated by a double Gaussian function. With this model function a proximity correction can be made.

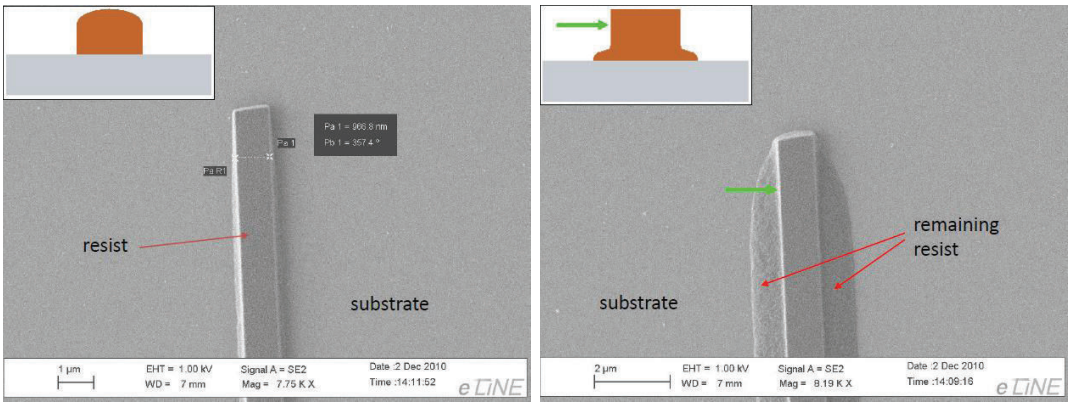

Figure 3.5 – SEM images to illustrate the intra proximity effect with an inset of the cross section of the resist profile. Left: correct dose and no proximity effect, right: strong proximity effect. The green arrows indicate same positions.

Thereby an adopted dose is calculated and applied, leading to a minimization of the proximity effect. For structures fabricated in this work a proximity correction with the included e-Line software by Raith was pointless because mainly of two circumstances:
The proximity correction software fractures objects in smaller elements and allocates them an adopted dose value. If an object approaches small lateral dimensions the proximity correction software is not able to place this fractured elements side by side without an positioning error. This leads to deformed objects. Further a proximity correction increases the number of exposed elements and therefore the overall exposure time. This is a critical value for structures fabricated in this work. However, the proximity correction for small objects and thin resist thicknesses can be done by adjusting the correct dose values, to keep the background exposure below a certain limit.

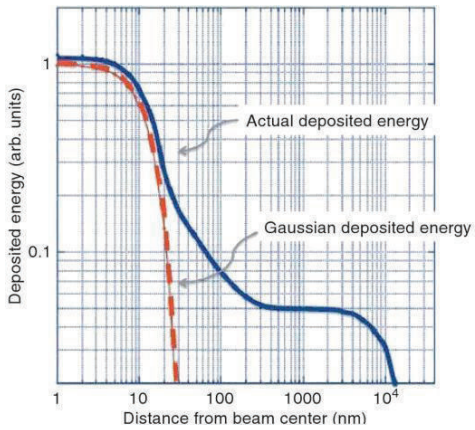

Figure 3.6 – Comparison of a Gaussian exposure (dashed line) and the actual energy deposited (solid line) in a resist on a bulk substrate. The added long-range exposure is due to electron scattering. (taken from[32])

3.2.7 Exposure modus

There are different exposure modes available within the Raith software. The exposure with the EBL-system is point by point, which means that the electron beam stays at the same point during exposure.

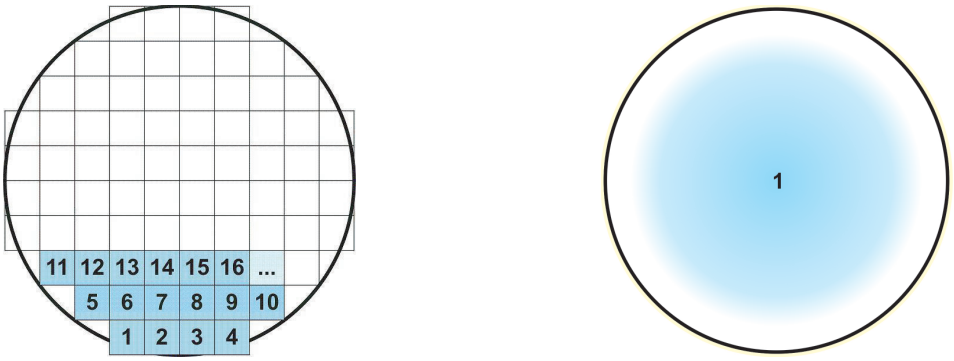

Figure 3.7 – Demonstration of the difference between an area exposure (left) and a dot exposure (right) using the example of exposing a circle.

Area exposure:
In the area exposure mode a designed object is fractured in smaller pieces with an adjustable size of the grid (**Figure 3.7**). As a standard this is a 10nm grid, but the adjustment depends on the size of the object. The lower limit of the grid size is given by the minimal dwell time of the system of 400ns. Every one of this fractured elements gets a dot exposure. The superposition of these dots produces the desired object due to electron scattering and the spot size of the beam.

Dot exposure:
An alternative exposure mode is the dot exposure. Especially for structures produced in this work (arrays of circles with a diameter in the sub-wavelength range) this fast method can be used. Instead of fracturing the designed object like in **Figure 3.7** on the left side, only one dot in the middle of the circle is exposed, demonstrated on the right side. The diameter of the circle is adjusted via the applied dose.

3.3 Lift-off from EBL structured negative resists

The developed resist get coated with a metal layer. The removement of the remaining metal covered resist is called the lift-off. This can be done with a liquid chemical which dissolves the remaining resist. Therefore the profile of the resist has to have a certain shape like in **Figure 3.8a)** or **c)**. A bad profile is pictured in **b)**. Here the metal totally covers the resist and the remover is not able to enter from the side to dissolve it.

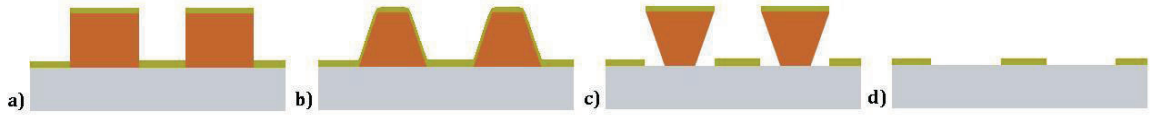

Figure 3.8 – Different profiles of a structured resist, a) vertical flanks, b) bad profile, c) undercut profile, d) structure after the lift-off

The ideal case would be the case in **Figure 3.8c)**, here the remover can enter easily to dissolve the resist resulting in a clean structured metal surface like in **d)**.

In EBL the scattering processes with the substrate generate backscattered electrons which produce the proximity effect (cf. 3.2.5 and 3.2.6). This leads to a trend of the profile of a negative resist with increasing exposure dose like illustrated in **Figure 3.9**.

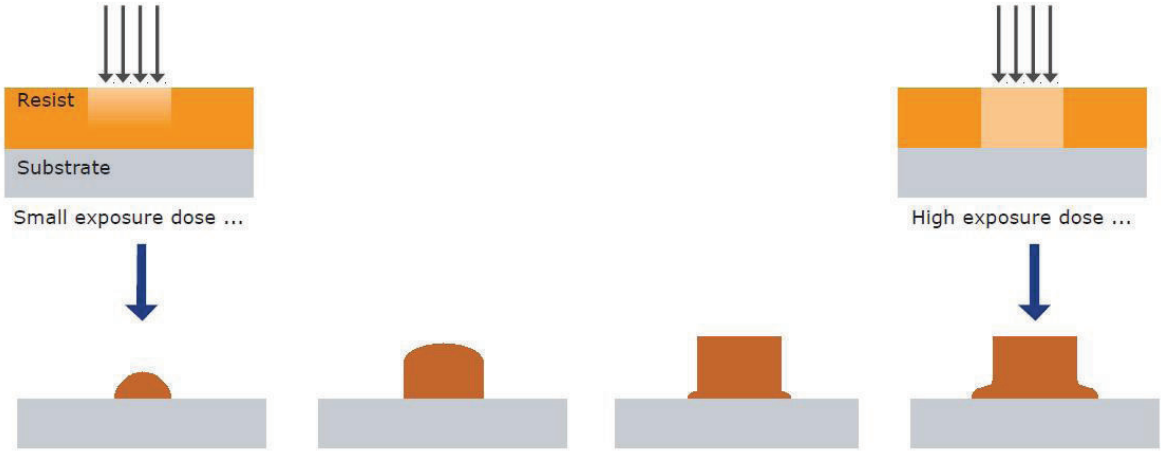

Figure 3.9 – Trend of the profile with increasing exposure dose in EBL for a negative resist (taken from [47] and modified).

With the exposure dose adjusted too high, the large amount of backscattered electrons cross-link the resist near the substrate in areas where the electron beam actually should have never exposed it. This indirect exposure leads to 'feet', coming out from the side making the lift-off problematic or even impossible. In the case of a negative resist for EBL it is not possible to adjust an undercut for a single layer system. Therefore bilayer systems are used [48]. Since the lift-off with vertical sidewalls like in **Figure 3.8a)** worked for the produced structures, no bilayer system was used in this work.

The results of a lift-off with a vertical sidewall structure and a bad structure are compared in **Figure 3.10**. On the left side a good working lift-off is shown. This is the result of vertical sidewalls of the object after the development step due to an exact applied dose, evident in the bottom left inset. In the right image a structure with a too high exposure dose applied is shown. The 'feet' visible in the bottom left inset lead to an increased width of the line after

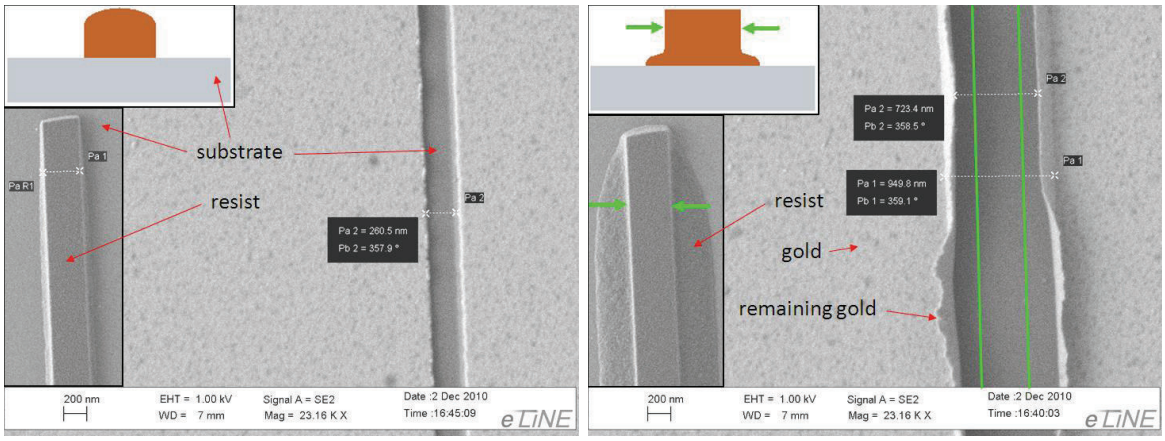

Figure 3.10 – SEM image after the lift-off step with vertical sidewalls (left) and a bad profile (right). Each with a SEM image after the development step in the inset in the bottom left corner and a schematic drawing of their respective cross sections in the upper left corner. The green arrows and green lines indicate same points.

the lift-off, indicated by the green lines and arrows. The metal on these feet is connected with the metal on the substrate. The remover dissolves the resist underneath and in the ultrasonic bath in the removing step this remaining metal flaps out. The resulting metal flanks are visible in the SEM image on the right side.

3.4 Sample preparation

The preparation of the samples for the EBL exposure and the spin coating process of organic layers on float-glass as well as on Au is the content of this section.

Substrate preparation for EBL exposure

The final objective of the structured metal films is the use as front electrodes in OSCs. Therefore the substrate should be transparent to the visible range (380-780nm) and infrared radiation (>780nm) of the electromagnetic spectrum. Glass fulfills this requirements but as it is an electrical insulating material negative charges placed on with the electron beam are not able to discharge to the ground and accumulate on the sample. This results in an electric field which influences the electron beam and leads to problems with focusing and the necessary alignment procedures shortly introduced in section 3.2. To overcome these problems, the samples need an electric conducting area connected to the stage, at which a discharge to the ground is possible.

The substrates used in this work were float-glass covered with Indium Thin Oxide (ITO) (**Figure 3.11**). To obtain only a small conducting area for the electron beam the ITO layer was structured with Hydrochloric Acid (HCl). Additionally this area can be used

as reference ITO electrode on the same sample. As a result differences in process conditions between the samples can be avoided.

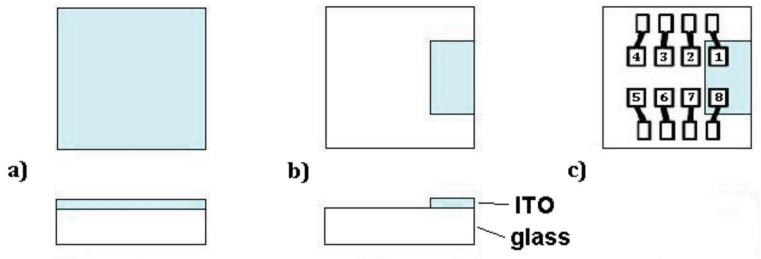

Figure 3.11 – Structuring of the ITO layer, a) ITO covered float-glass; b) Partly etched ITO layer; c) Pad 1 and 8 as reference ITO electrode;

Substrate cleaning

First the substrate were pre-cleaned with acetone and isopropanol in the laboratory. To prevent contaminations the following work was done in a laminar-flow box in an ISO class 6 cleanroom at the NTC-Weiz:
The substrate was rinsed with acetone and dried with the N_2 gun. This steps were repeated with isopropanol. Afterwards the sample was further cleaned with an ultrasonic bath in isopropanol for 15 min at level 4. Then the sample was dried again with N_2 and after a rinsing step with deionized water, every impurity should be removed. Subsequently the sample was dried with N_2 and the spin coater at 5000rpm for 100s. A dehydration bake was applied at 200°C for 5 minutes in N_2 atmosphere to ensure that the surface is free of water.

Resist and HMDS coating

The cleaned substrate was oxygen plasma activated at about 0,4mbar to turn the surface hydrophilic. Directly afterwards a layer of HMDS (Hexamethyldisilazan) was evaporated. The HMDS molecule chemically bonds with its Si atom to the oxygen of the oxidized surface by releasing ammonia. The remaining methyl groups of the HMDS fragment form a hydrophobic surface [33]. This hydrophobic surface improves the resist wetting and adhesion. The used resist was a NLOF 2070-500nm grade from MicroChemicals [34]. It was spin coated on the surface treated sample with 4000rpm and a ramp of 2 for 60 seconds, leading to a resist thickness of 400nm. In order to further improve adhesion the remaining solvent was reduced by a thermal treatment at 100°C for 60s, called *Softbake* [44].

The resist above the ITO was wiped away and polystyrene spheres with a diameter of 100nm were applied. These spheres facilitates the alignment procedures of the electron beam.

PEDOT:PSS coating

Float-glass substrates coated with Au were covered with PEDOT:PSS (Poly(3,4-ethylenedioxythiophene) poly(styrenesulfonate)). Since the PEDOT:PSS is dissolved in water the hydrophilic or hydrophobic nature of the Au surface is important for the wetting

property. The surface property of Au surfaces was discussed over decades in the scientific community. This controversy in literature resulted from different 'clean' Au surfaces. Clean Au surfaces can only be obtained under Ultra High Vacuum (UHV) and under this conditions the surface is hydrophilic [39]. An exposure to atmospheric air reduces the high surface free energy of gold by adsorption of organic molecules [40].
To establish defined conditions the Au covered substrates were plasma activated with oxygen plasma for 10min at about 0,4mbar. Directly afterwards PEDOT:PSS were spin coated with 2500rpm for 40s and a ramp of 4, leading to a 55nm thick PEDOT:PSS film on Au. Without this plasma activation the PEDOT:PSS film was not wetting and in some cases no uniform film was established. To remove any residual solvent, the layer was annealed at 120°C with an ambient pressure of about 10^{-4}mbar for 20min.

PTB7 coating
The following work was performed in an argon-box. The PTB7 (Poly[[4,8-bis[(2-ethylhexyl) oxy]benzo[1,2-b:4,5-b']dithiophene-2,6-diyl][3-fluoro-2-[(2-ethylhexyl)carbonyl]thieno[3,4-b]thiophenediyl]]) was dissolved in chlorbenzene with a concentration of 10g/l. This solution was stirred first 20min at 50°C and then 1h at room temperature. The cleaned float-glass or the Au covered float-glass were plasma activated for 10min in an oxygen plasma to establish surface activated and therefore defined surfaces. Then the PTB7/chlorbenzene solution was spin coated with 1200rpm for 120s and a ramp of 4 resulting in the same thickness of the organic layers of around 32nm.

3.5 Characterization methods

To obtain the optical and structural properties of the fabricated structures a variety of analysis tools were used:

3.5.1 Profilometer

The layer thicknesses were measured with a DEKTAK150 Profilometer. To estimate the layer thickness the mean of 3 different positions on the sample were taken.

3.5.2 Scanning Electron Microscope (SEM)

The SEM at the NTC-Weiz is a part of the Electron Beam Lithography (EBL) system, which is the Raith e-Line introduced in section 3.2.

3.5.3 Atomic Force Microscope (AFM)

The AFM measurements were performed by Alexander Blümel on a VECCO Nanoman VS atomic force microscope. The working principle is, that a cantilever with a sharp tip scans the surface. Forces between the tip and the surface deflect the cantilever. This deflection is measured with a laser spot that is reflected from the top of the cantilever. The forces between the tip and the surface depend on the operational mode of the AFM and can be mechanical contact forces, Van der Waals forces, capillary forces, chemical bonding, electrostatic or magnetic forces.

3.5.4 Transmission measurements

The transmission measurements were performed with a PERKIN ELMER UV/VIS/NIR LAMBDA 900 spectrometer. In this spectrometer 2 radiation sources a deuterium lamp and a halogen lamp cover the working wavelength range UV/VIS/NIR. The light is monochromated before the beam interacts with the sample. Spectra recorded for this work are *zero order transmission spectra* that means the incident and the detected light are collinear. The samples were always placed into the spectrograph in such a way that the incident beam enters perpendicular to the sample surface, first passing through the substrate and leaving the sample at the side where the structured metal and/or the polymer was coated (**Figure 3.12**). To illuminate only the structured area, a relative small quadratic aperture of about 1x1mm^2 was used in the incident beam directly in front of the sample.

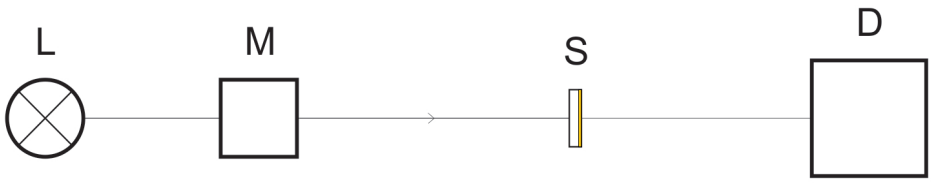

Figure 3.12 – Principle setup of zero order transmission measurements with the main components: lamp (L), monochromator (M), sample (S) and detector (D).

The absorbance of a polymer layer was calculated as:

$$Abs = ln\left(\frac{I_0}{I}\right) \tag{3.3}$$

With I_0 the intensity of the reference beam through the glass substrate and I the intensity after passing through the polymer covered glass sample.

To measure additionally the scattered light and not only the zero order beam a setup with an Integrated Sphere (IS) was used which is schematically pictured in **Figure 3.13**.

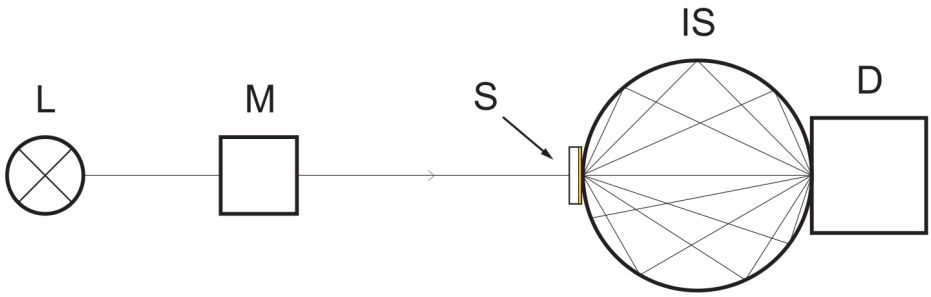

Figure 3.13 – Principle setup of measurements with an integrating sphere and the main components: lamp (L), monochromator (M), sample (S), integrating sphere (IS) and detector (D).

3.5.5 Photoluminescence (PL) measurements

PL measurements were done with a SHIMADZU RF-5301PC Spectrofluorometer. The samples were inserted in the sample holder like demonstrated in **Figure 3.14**. The incident beam hits first the polymer layer, then the substrate or underlying coatings. In the schematic drawing of the setup it is indicated that the exciting beam hits the sample in a different angle as the recorded beam gets detected. The exciting beam angle α is about 36° and the recording beam β about 56°. This means direct reflected light can only reach the detector due to diffuse reflection e.g. because of surface roughness. An aperture with a quadratic opening of about 4x4mm^2 was used directly in front of the sample.

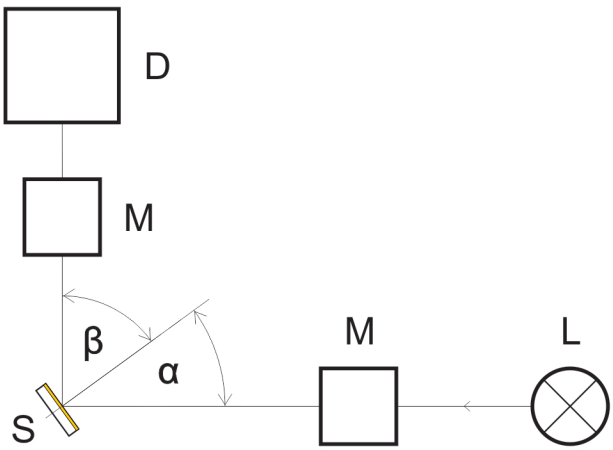

Figure 3.14 – Principle setup of photoluminescence measurements and the main components: lamp (L), monochromator (M), sample (S), detector (D)

Chapter 4

EBL fabrication of plasmonic electrodes

Besides the excitation of Surface Plasmons (SPs) by light or electrons it is also possible to excite SPs by electroluminescence in OLEDs on their metal electrodes [42]. With respect to the light emission of OLEDs, this can be a mayor loss channel. Alternatively this effect is used to emit SPs in a controlled way by an organic plasmon-emitting diode [43].

If this effect can be used in the opposite direction i.e. SPs increase the exciton generation, an improved light incoupling is possible for OSCs. To excite SPs by photons a grating is necessary to compensate the mismatch of the momentum (cf. section 2.4.3). The plasmonic electrodes fabricated in this work are optical thin metal films with a periodic sub-wavelength hole array as coupling element (**Figure 4.1**). The structure is produced via EBL and a lift-off technique. Since the exposure is time optimized structuring of a 3x3mm^2 area in about 10h is possible.

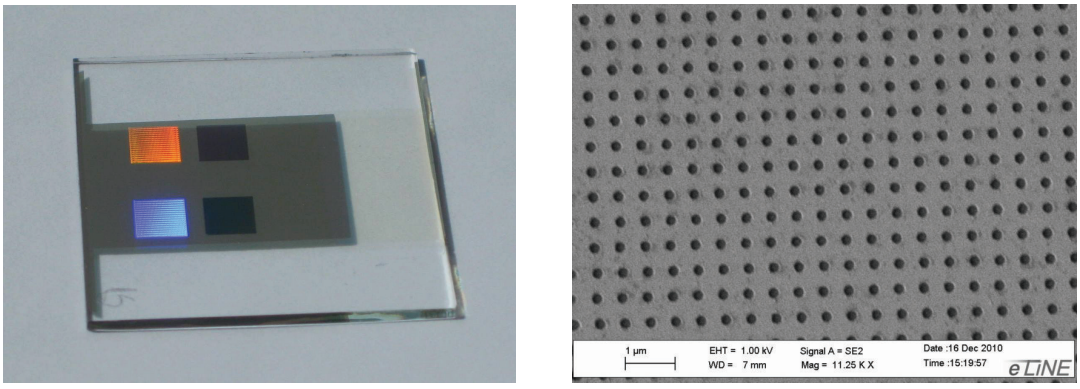

Figure 4.1 – Left: Gold film with plasmonic electrodes illuminated with white light. Right: SEM image of plasmonic electrode.

4.1 Lithographic process

The main steps of the lithographic process include: sample preparation, exposure with the electron beam, development of the resist, thermal evaporation of a metal film and the removement of the remaining metal covered resist the so called lift-off (**Figure 4.2**).

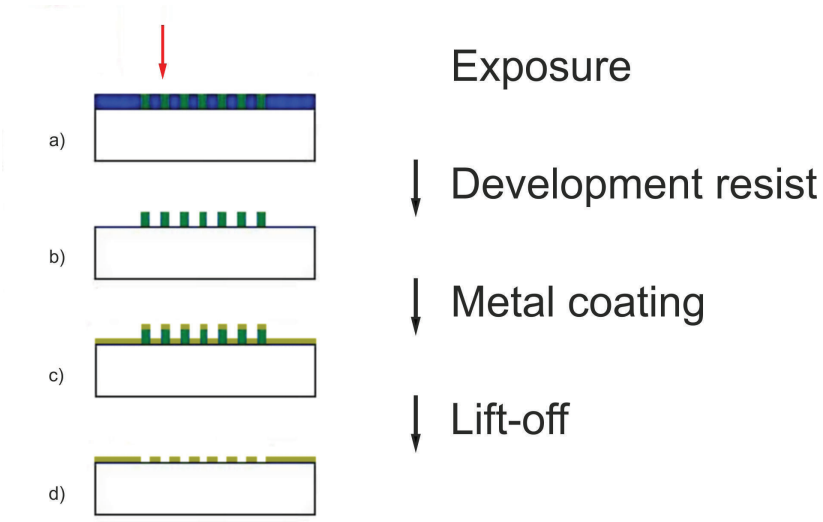

Figure 4.2 – Lithographic process with a negative resist. a) Exposure of the sample; b) Sample after the development step; c) Sample after thermal evaporation of a metal film; d) Sample after the lift-off process;

The *sample preparation* includes substrate cleaning, applying an adhesion promoter and a 400nm thick negative resist (NLOF 2070-500nm [34]). This steps are explained in the sample preparation section (3.4).

The *exposure* was done via a time optimized exposure procedure with the e-Line. To complete the cross-linking a Post Exposure Bake (PEB) at 110°C for 60s was applied.

In the *development* step, the resist is selective dissolved. Therefore the sample was immersed into the developer AZ826MIF [34] for 70s, rinsed with deionized water, dried with N_2 and the spin coater (2000rpm for 50s).

The step from **b)** to **c)** in **Figure 4.2** is the *metal coating*. In this work different thick Au films were thermally evaporated. Due to bad adhesion between Au and the substrate, a Cr layer was used to improve adhesion [35].

For the final *lift-off* step two methods were used. Primary a wet chemical lift-off with the remover NMP (N-Methyl-2-pyrolidone) [34] was done by immersing it into the remover 5min with an ultrasonic bath, level 2 at 65°C. To complete the step, the sample was

rinsed with deionized water, dried with N_2 and the spin coater (5000rpm for 50s).
For structures exposed with the EBL dot exposure mode, a polymer was applied and the remaining metal covered resist was stripped off.

4.1.1 Exposure with EBL system

As mentioned in the first chapter, the final objective of this work, was to incorporate the structures in organic optoelectronic devices. The standard dimension for OSC and OLED at the NTC-Weiz is 3x3mm^2. Therefore it was beneficial to fabricate as well such large structures to enable an easy incorporation.

4.1.1.1 Time optimized parameters

Structuring an area of 3x3mm^2 with sub-wavelength features via EBL is a high technical effort, since the EBL-system is a single beam system and the features have to be exposed one by one in a serial manner. This makes an optimization of all the time dependent parameters necessary and will be discussed in this section.

To quantify the overall exposure time, a particular example will be used. The exposed pattern is a sub-wavelength circle array, which finally leads to the sub-wavelength hole array (**Figure 5.5**) thus the plasmonic electrode. The period, which is the distance between the circles is 500nm and the diameter of the circles are 200nm with the structured area extending over 3x3mm^2. Consequently there are 36 million circles to be exposed.

Principally exposure time was reduced by optimizing the settling time, the dwell time and a change of the exposure modus.

4.1.1.1.1 Settling time

For stabilization of the electron beam this waiting period is applied before exposing a new object. The settling time is adjusted in the ms range, for non time critical exposures. Since the unit waits the settling time before exposing individual objects, with an adjustment of 20ms and the aforementioned example of 36 million circles this time adds up to a total time of 200h. In the same way 20μs settling time add up to only 12min, which points out the importance of optimizing this adjustment.

The influence of the settling time adjustment on the resulting pattern was analyzed by a circle array test pattern with a variation in the applied dose as well as the circle diameters (**Figure 4.3**). The results were analyzed concerning the magnitude of the

stitching error. By exposing the pattern with a constant settling time, it was noted that the stitching error depends on the circle diameters and dose values. More precisely this error is reduced with smaller dose values and smaller diameters of the circles. This means that fewer electrons were put on the sample and it seems likely that this stitching error is mainly produced by charging effects.

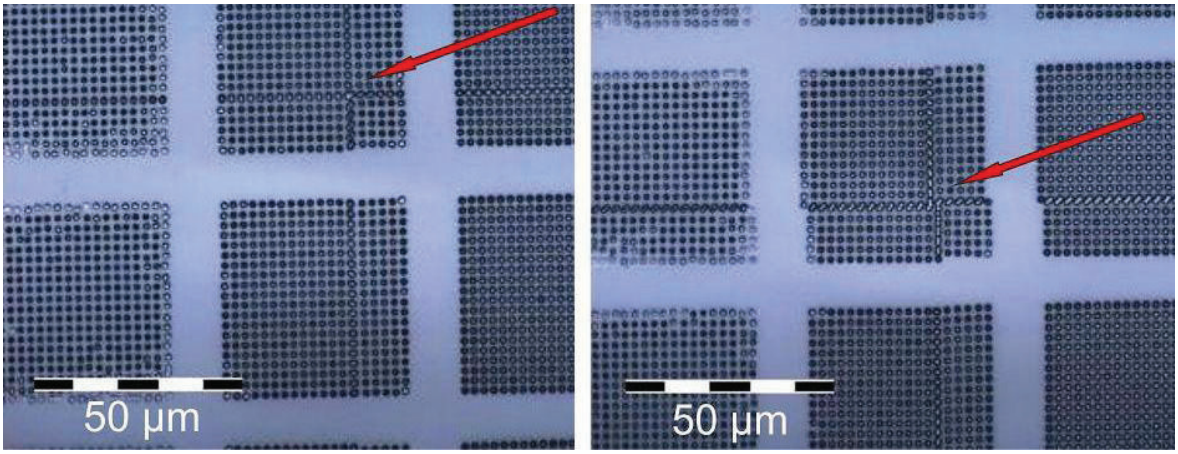

Figure 4.3 – Optical microscope image to demonstrate the influence of the settling time on the stitching error. Sample: 400nm thick AR-N 7520.18 from Allresist on glass after the development, left: 20ms settling time and a very small stitching error, right: 20μs settling time with increased stitching error. The arrows indicate same points of stitching errors.

By exposing two patterns, with different settling times an additional dependency of the stitching error on the settling time was noted (**Figure 4.3**). In the left image the pattern was exposed with a settling time of 20ms in the right image a settling time of 20μs was adjusted. It can be seen that with the shorter settling time a more pronounced stitching error is present. This can also be explained through charging effects:
During the longer settling time, the charges have time to distribute better in the resist or even partly discharge, therefore lower local charging is present, which reduces the stitching error.

A compromise between time and accuracy was made and consequently *the settling time was adjusted to 0,2ms.*

4.1.1.1.2 Dwell time

The actual time the electron beam is exposed to the sample i.e. the dwell time, depends on the applied dose, the beam current and the exposed area. In formula (3.2) it appears to be the following possibilities to reduce the dwell time:

- **Minimization of the exposed area A**:
  As explained in section 3.2.4 positive and negative resists can be used. For this kind of application, a positive resist implies more complicated techniques. This can be a mix-and-match technique where photolithography and EBL are combined [45].

Figure 4.4 – Illustration of the difference in exposed area of a positive resist (right side) and a negative resist (left side). The pigmented area represents the area to be exposed by the electron beam for obtaining the same results.

However exploring these options more in detail is not necessary, as demonstrated in **Figure 4.4** the exposed area is much larger with a positive resist. Using the geometric values of the above mentioned example results in a 8 times larger area to be exposed. This points out, that for the fabrication of a metal film with sub-wavelength holes by a lift-off technique, a *negative resist* has to be used in order to keep the dwell time within a certain limit.

- **Maximization of the beam current I**:
  The beam current can be adjusted by the aperture of the SEM. To understand the relation between the aperture, the beam current and the total exposure time, a test pattern with different circle arrays was designed. The pattern was exposed several times using the same applied dose but different apertures. The beam current and the total exposure time were measured (**Figure 4.5**).

  A polynomial fit was made with the data of the beam current and it reflects the r^2 behavior, since the beam current is proportional to the area of the aperture.

  The total exposure time first drops radical, increasing the aperture. With 20μm to 120μm diameter apertures only little changes in the total exposure time are present. This means that system relevant times (i.e. settling times or stage move time) are much larger than the dwell time itself. As a result an aperture with a diameter larger than 20μm is not a potential time saving adjustment. Furthermore alignment procedures can be challenging, using bigger apertures. Accordingly a *20μm diameter aperture* was used.

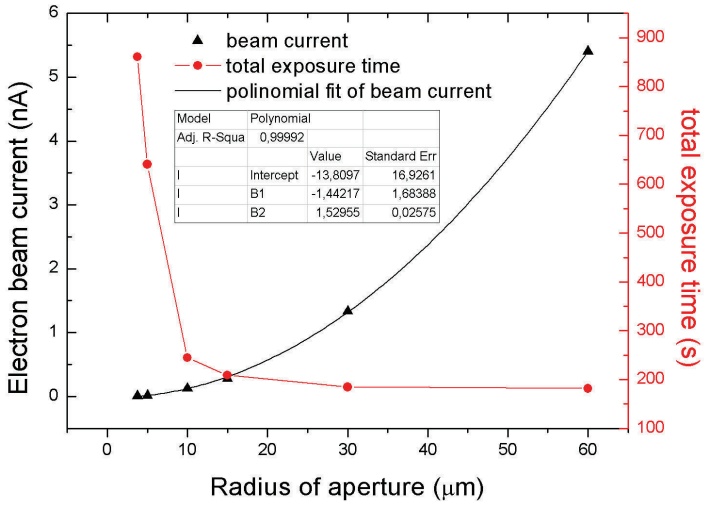

Figure 4.5 – Beam current and total exposure time for a test pattern of different circle arrays exposed with the EBL dot exposure mode as a function of the aperture size.

- **Minimization of the applied dose D**:
  There is the possibility to use a very *sensitive resist* and therefore a less applied dose is necessary to cross-link the polymer. Another option would be to use a *lower acceleration voltage*. With a lower acceleration voltage the electrons have less kinetic energy and the interaction probability between molecules of the resist and electrons is higher. Hence a lower applied dose is necessary. The drawback of a lower acceleration voltage is a reduction in lateral resolution since the higher interaction probability causes a higher fraction forward scattered in relation to backscattered electrons. This broadens the beam in the resist and consequently, as the beam energy is reduced, the smallest producible feature increase [46]. The acceleration voltage used in this work was usually 20kV.

4.1.1.1.3 Exposure modus

There is the possibility of an area exposure or a dot exposure (cf. section 3.2.7). For sub-wavelength circle arrays exposed with the area exposure not only millions of circles have to be exposed, as well every circle is fractured into about 100 pieces where the e-beam has to be positioned. Therefore the overall exposure time increase exorbitantly. Alternatively in the dot exposure mode one circle gets one exposure in the center of the circle. With the dot dwell time the diameter of the circle can be adjusted. The huge reduction of overall exposure time is evident in **Table 4.1**.

Table 4.1 – Comparison of the overall exposure time for different exposure modes and different periods of a 3x3mm^2 sub-wavelength circle array with a circle diameter of 200nm
p ... period of the hole array
t_D ... overall exposure time for the dot exposure mode
t_A ... overall exposure time for the area exposure mode

p / nm	t_D / h	t_A / h
500	10,3	124,8
1000	3,6	31,2

4.1.1.1.4 Summary time optimized parameters

The time optimized parameters and settings for the fabrication of plasmonic electrodes via a EBL system are summarized in **Table 4.2**.

Table 4.2 – Essential parameters for the fabrication of plasmonic electrodes

Parameter	Value
Settling time	0,2ms
Resist	negative
Aperture	20μm
Acceleration voltage (EHT)	20kV
Exposure modus	dot exposure

Additionally it has to be noted that for patterns with repeating objects, *Structure References* should be used. A structure reference is a reference to a object. This can be a single object like a circle, or a structure which is a group of objects, like a circle array. This way repeating structures can be transfered to the lithographic system only by a reference, which saves transfer time and minimizes the chance that an error in the EBL system occurs. Mostly such errors occur during long exposures with the only message: "EXPOSURE ERROR".

4.1.1.2 Exposure dose for sub-wavelength circle arrays

According to the results of **Table 4.1** the EBL dot exposure mode should be used for the fabrication of sub-wavelength circle arrays to limit the exposure time. To know which dot dwell time is necessary for a desired diameter of the circles, the dose-diameter relation has to be measured. Therefore a dose test pattern was designed, pictured in **Figure 4.6a)** after the development step.

An important property is the dependency of the dose-diameter relation on the period of the circle array. This means that a dose test pattern with different periods is necessary. Therefore arrays of 20x20 circles with a period of 1000, 750, 500 and 400nm were designed.

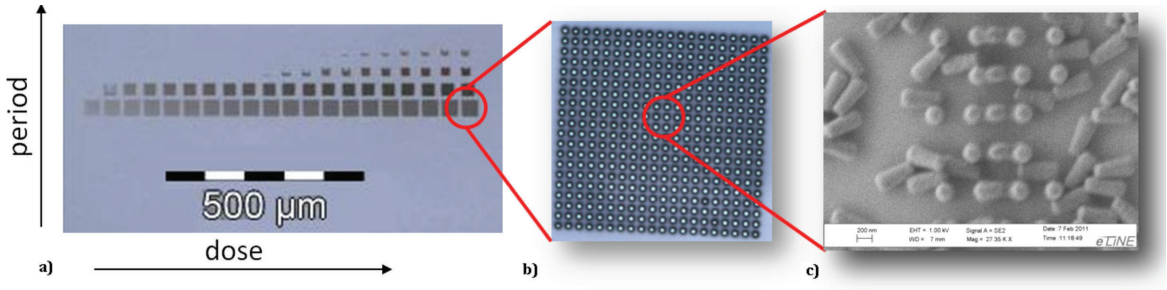

Figure 4.6 – Dose test pattern to obtain the dose-diameter relation. Sample: 400nm thick NLOF2070-500nm grade on glass after the development; a) Optical microscope image after development of the entire dose test; b) More detailed optical microscope image of one of the 20x20 circle matrices; c) SEM image of partly tilted pillars;

In **Figure 4.6a)** this variation can be seen in the vertical direction. In the horizontal direction the variation of the dwell time was done by applying different exposure doses at each of the 20x20 matrices highlighted in **Figure 4.6b)**. The SEM image in **Figure 4.6c)** shows tilted pillars to get a topographic impression and to remind that this circles in **a)** and **b)** are pillars of resists standing on a glass substrate.

The entire lithographic process as explained in section 4.1 was carried out, resulting in different metal hole arrays. All the diameters of the holes were measured via the SEM and the results are shown in **Figure 4.7**

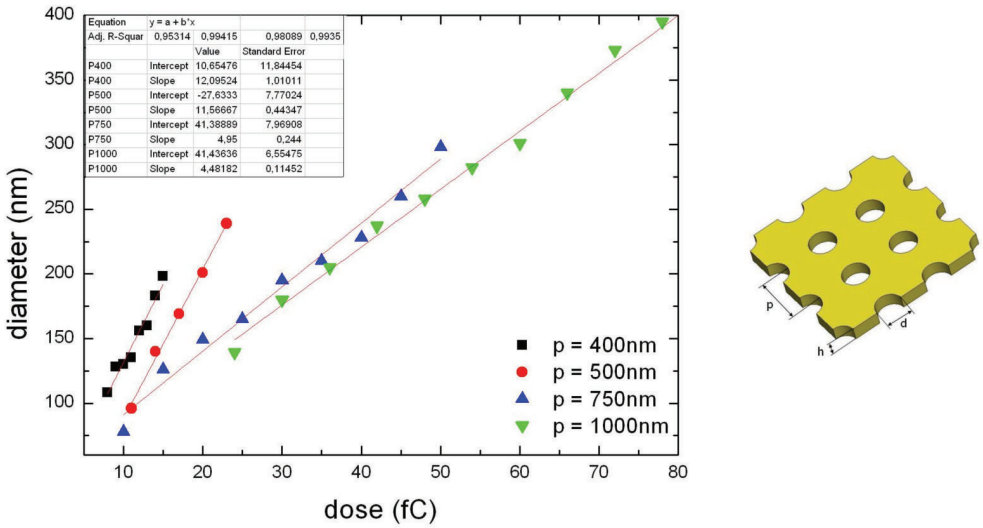

Figure 4.7 – Dose-diameter relation (left) for different periods of the hole array exemplary pictured on the right side

In this graph the dependency of the dose diameter relation on the period can be seen. To analyze the dependency, dose values for a 200nm hole diameter array are listed in **Table 4.3**.

Table 4.3 – Dose values for a 200nm hole diameter array for different periods

Period p / nm	Applied dose D / fC
400	15,7
500	19,7
750	32,0
1000	35,4

It can be seen, that with increasing period the applicable dose increases as well. This increase of the dose gets smaller with increasing period and seems to come to a level where it stays the same. That is, the dependency of the applied dose vanishes at a certain distance. Since the period is in the range were backscattered electrons are expected (cf. section 3.2.6), electrons are scattered in the entire resist. This means as well in between the direct exposed circles. As a consequence the superposition of the backscattered electrons produce a more or less strong background exposure in the resist (inter proximity effect). The strength depends on the period of the array. In between the circles only this small background exposure is not enough to cross-link the polymers sufficient to reach the molecular weight to withstand the development process (cf. section 3.2.4). In the area of the direct exposed circles the polymer has already cross-linked and reached this critical molecular weight and a further cross-linking due to the background exposure don't change the result. In contrast at the border of these circles this small background exposure can be enough to exceed the critical value. As a result, circle diameters increase with decreasing periods by applying same dose values. Hence, to obtain the same circle diameters with reduced periods the applied dose values have to be decreased.

In **Figure 4.7** it can be seen that the diameter is only adjustable in a certain window. The minimum diameter is limited by the fact that these resist pillars on the substrate tilt due to bad adhesion, if the aspect ratio gets too high. This could be reduced by reducing the resist thickness. The maximum diameter is limited by the intra proximity effect. Due to the large diameter i.e. high exposure dose the resist near the substrate is cross-linked, producing a bad profile of the structure and the following lift-off step is impossible.

4.1.2 Development

The not exposed parts of the resist were dissolved with the developer AZ826MIF [34] by immersing the sample for 70s. Afterwards it was rinsed with deionized water, dried with N_2 and the spin coater (2000rpm for 50s).

After the development step, resist pillars are standing on the sample, which after the lift off step represent the holes of the metal hole array. These standing pillars form a 2dim

Photonic Crystal (PhC). A PhC has a photonic bandgap, which is a forbidden energy range for photons in the crystal. Illumination of the PhC with Photons of this energy results in reflection of the photons. Since this are 2dim PhC the energy of the bandgap depends on the incidence angle of the beam. In the 3dim case this can be compared with a semiconductor and the bandgap for electrons.

In **Figure 4.8** a sample with three different structured areas after the development step can be seen. This areas form 3 different 2dim PhCs, which are illuminated with white light. Due to the different periods of the PhCs, different wavelength of the white light are forbidden in the crystal i.e. get reflected outward.

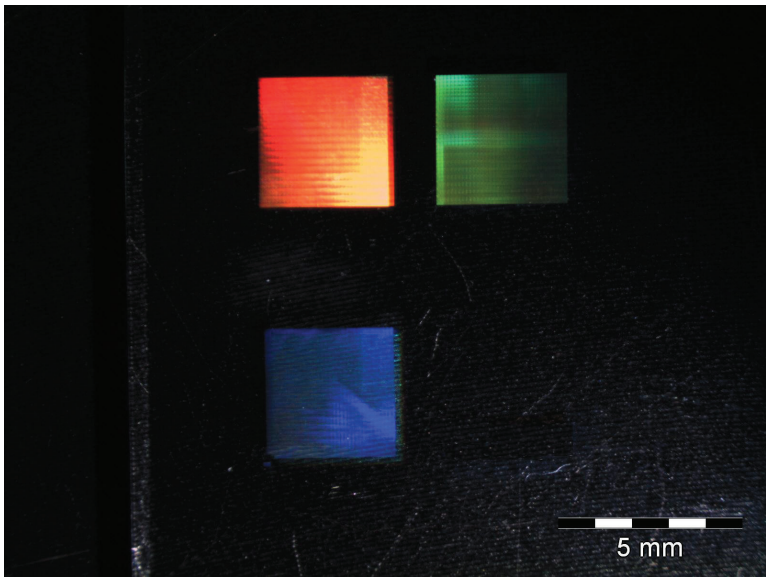

Figure 4.8 – Sample after the development step, illuminated with white light under the stereo microscope. The 3 structured areas with a period of 500nm, 750nm and 1000nm form different 2dim photonic crystals.

4.1.3 Metal coating and lift-off

The exposed and then developed samples were coated with a metal layer in an evaporation chamber, which was evacuated to a pressure of $< 10^{-6}$mbar. Primary a 2nm Cr adhesion layer with a deposition rate of 0,2Å/s and secondary a 30nm Au layer with a deposition rate of 2Å/s was evaporated.

Illumination of such metal coated, 2dim photonic crystals with white light results in a reflection of different colors at certain angles due to different periods of the structure. Pictures of a sample, captured at different angles can be seen in **Figure 4.9**.

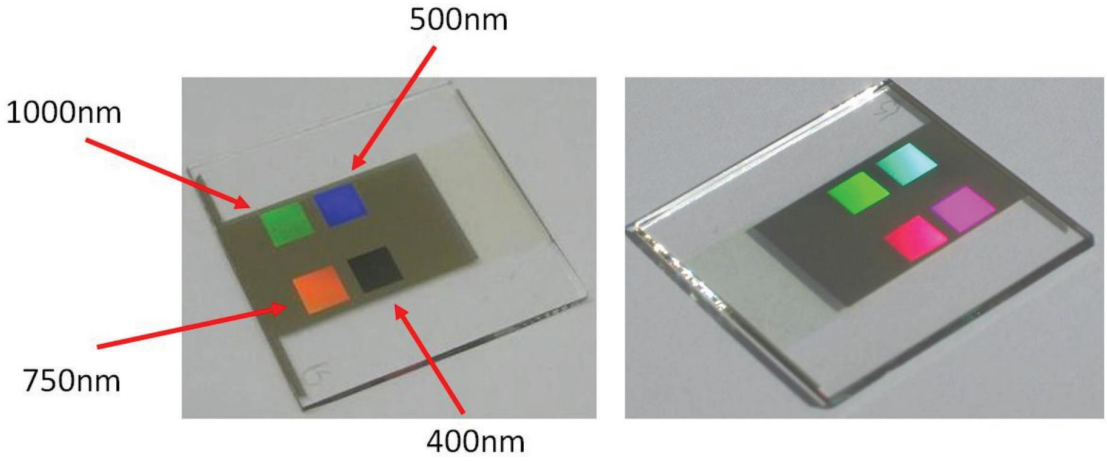

Figure 4.9 – Sample after evaporation of 2nm Cr / 30nm Au, illuminated with white light. The different structured areas are indicated with its periods of 400nm, 500nm, 750nm and 1000nm. They form different 2dim photonic crystals covered with a metal layer.

4.1.3.1 Lift-off process: Wet chemical vs. First Contact^{TM} polymer

Two different methods for the lift-off process were used. In the first place a wet chemical lift-off with the remover NMP (N-Methyl-2-pyrolidone) [34] was done by immersing it into the remover 5min with an ultrasonic bath, level 2 at 65°C. To complete the step, the sample was rinsed with de-ionized water, dried with N_2 and the spin coater (5000rpm for 50s). The second method with a polymer was used for structures exposed with the EBL dot exposure mode (section 3.2.7). The wet chemical lift-off worked well for arrays fabricated with the area exposure, in contrast with the dot exposure the metal was not lifted over the entire areas. This can be seen in **Figure 4.10** in the optical microscope image.

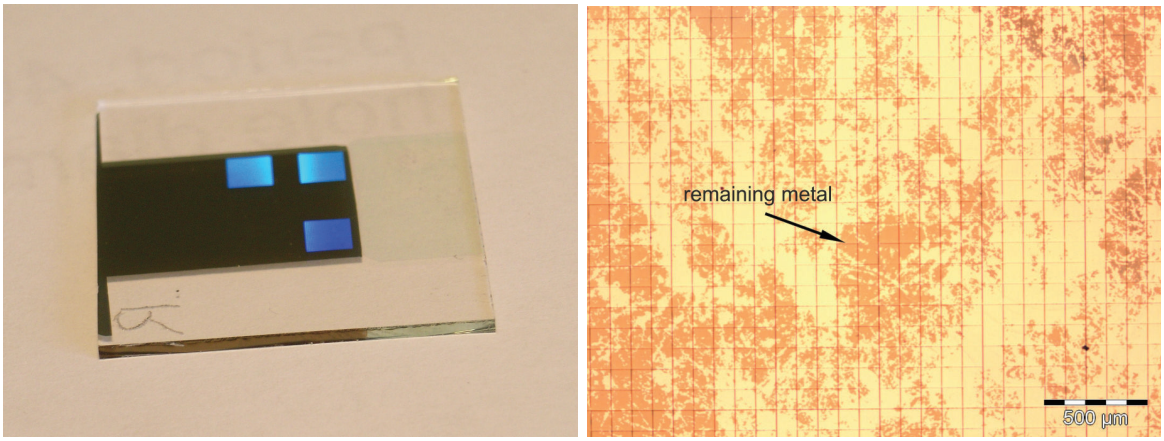

Figure 4.10 – Left: Sample with 3 structured areas with the dot exposure mode after thermal evaporation of 2nm Cr / 30nm Au. Right: Optical microscope image of one of these structured areas after the lift-off. The metal was not lifted completely represented by darker areas, emphasized by the arrow. The grid with the distance of 100μm are stitching errors of the 100x100μm^2 write fields.

In the SEM images in **Figure 4.11** it can be seen that the brighter areas of the optical microscope image in **Figure 4.10** represent a good working lift-off and in the darker areas the lift-off was not working well.

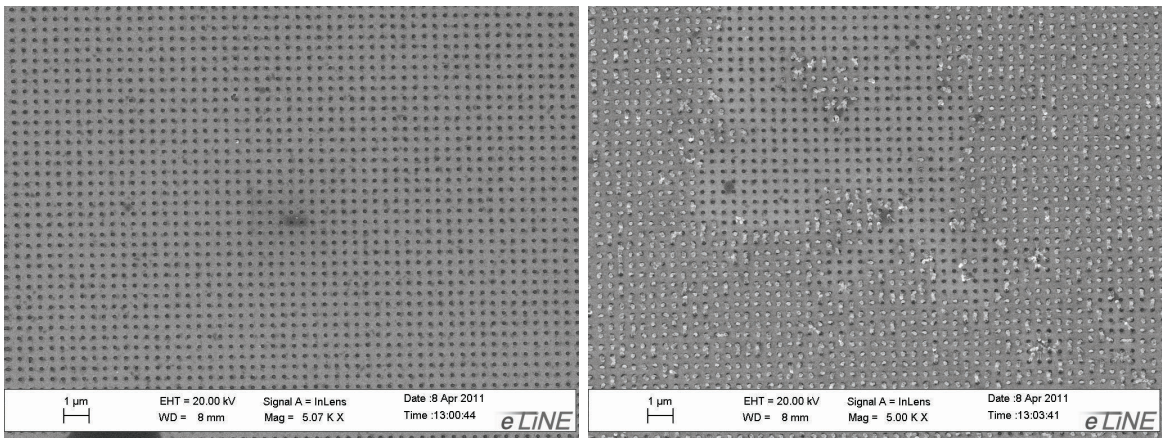

Figure 4.11 – SEM images of the different bright areas from the optical microscope image in **Figure 4.10**. Left: Working lift-off expressed by the bright areas. Right: Not working lift-off expressed by dark areas.

The first suspicion was that with the dot exposure, the profile of the structure is not vertical enough, and therefore the metal covers the entire resist in some areas and consequently cannot be dissolved by the remover. The SEM at the NTC-Weiz is not equipped with a tilting stage. To get an impression of the structures profile, the sample was put in tilted like it is shown in **Figure 4.12** on the left side.

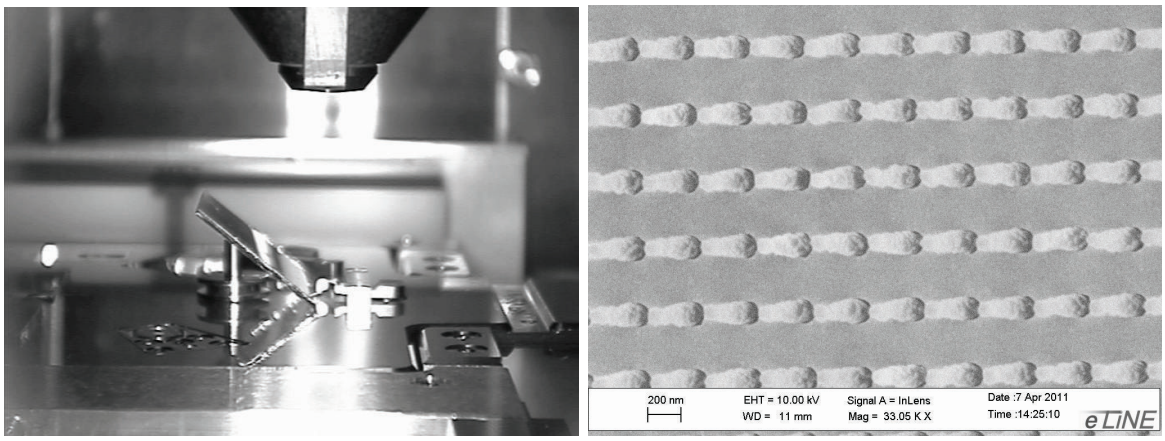

Figure 4.12 – Left: Image of the tilted sample in the vacuum chamber. Right: Perspective blurred SEM image of a dot exposed structure after thermal evaporation of 2nm Cr / 30nm Au.

The SEM image in **Figure 4.12** was captured after the thermal evaporation step of the metal to get better images avoiding charging effects. It shows the profile of the structure, which was the same over the complete structured area. As well the distributor of the

resist-developer-remover system, MicroChemicals confirmed that the lift-off with this resist profile should not cause any problems.

Therefore more tests were done with structured resists directly after the development step, i.e. without the metal on it. The removing steps were performed with increasing process times and the samples were inspected, if the complete resist was lifted. With this tests it turned out that the remover was not able to dissolve the resist even after 2h for samples exposed with the dot exposure mode. MicroChemicals explained the circumstance through a too strong cross-linking of the polymer in the resist as a consequence of the unusual exposure method. As a result, the resist gets hard baked during exposure and the remover is not able to dissolve the polymer. To overcome this problem a different lift-off technique with a polymer was elaborated.

First Contact Polymer is a product for cleaning and protecting precision optics and surfaces. It is a specially formulated polymer solution on acetone base that has been chemically optimized to minimize the surface adhesion. This polymer was used for the lift-off by putting a drop of this solution on the structured area. A waiting period of about 2h was enough to totally evaporate the solvent. Then the lifting was carefully started at one edge. Once the edge has started lifting, the entire film was coming off. It has to be noted that this method was not working always well. Sometimes the complete metal film was removed from the substrate. An improvement of the procedure was achieved, while putting the sample into the fridge for about 20min, before dropping the polymer on it. Here an additional condensed water layer between the metal and the polymer further reduced adhesion. A further surface treatment could also be a plasma activation.

The lift-off with the polymer worked most times, but only with an increased chrome layer thickness compared to the wet chemical lift-off. Probably with a alternative resist the problem of hard baked resist during exposure don't occur and the wet chemical lift-off can be used.

4.1.3.2 Minimization of the chrome layer

Always a chrome layer under the gold film is necessary to establish adhesion to the glass substrate. Unfortunately the optical properties of chrome in terms of semi-transparency are worse than for gold and SPP propagation is damped in chrome. This properties will be discussed more detailed in section 5.2.1.2. Accordingly the chrome layer has to be minimized if such a metal compound is used as semitransparent plasmonic electrode. Therefore 3 float-glass samples coated with 30nm Au were prepared with a variation of the chrome layer from 0 to 1nm. These films were prepared without any structure. After the thermal evaporation

of the metals they were immersed in the remover NMP at 65°C for 5min with an ultrasonic bath at level 2 to simulate the wet chemical removing process. After these steps the samples looked like it is shown in **Figure 4.13**.

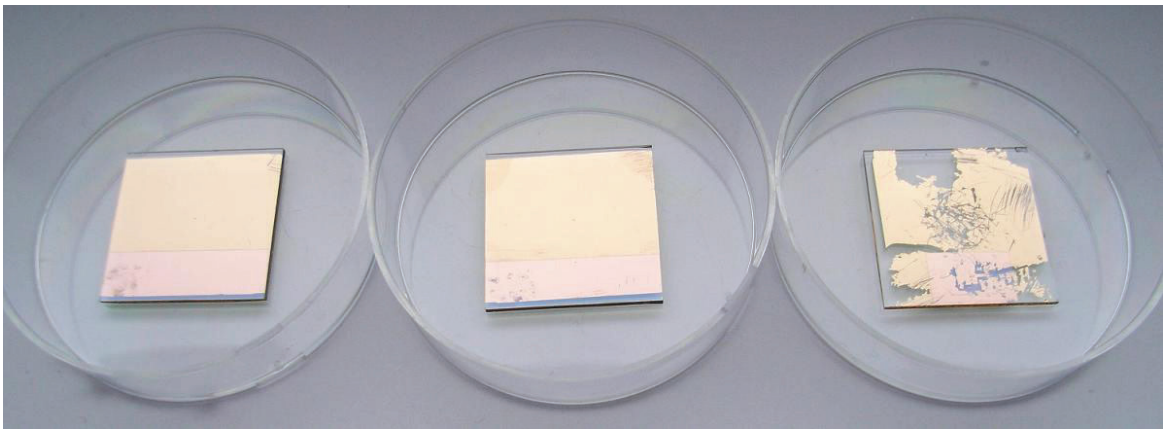

Figure 4.13 – Au coated glass substrates with (left) 1nm, (middle) 0,5nm and (right) without a chrome adhesion layer, after being in the remover NMP for 5min at 65°C in an ultrasonic bath at level 2.

The force of the ultrasonic vibrations in the bath partly removed the Au layer from the sample without the Cr adhesion layer. The conclusion of this small experiment was that the chrome layer of 0,5nm is enough for the defined wet chemical removing step.

For the lift-off with First Contact^{TM} polymer a similar experiment showed that a 2nm chrome layer is necessary to establish sufficient adhesion.

4.2 Thermal treatment

To get a topographic information, structures exposed with the dot exposure method and lifted-off with the First Contact^{TM} polymer were investigated with the Atomic Force Microscope (AFM). A 2x2μm^2 AFM image of a metal hole array with a period of 400 and 500nm is shown in **Figure 4.14**.

Some metal spikes up to 50nm in height were observed. These are residuals of metal adhered on the side of the resist pillars which were standing on the substrate. The cross section of one particular spike in **Figure 4.14** left side, shows a height of 32nm. Holes were still partly filled with resist, observable in the cross section on the right side of the figure. One partly filled hole had a depth of 22nm. To reduce the metal spikes an annealing step at 300°C for 3h at an ambient pressure of 100mbar was applied. After the annealing step the height of this particular metal spikes reduced down to 9nm and the hole was deepened down to 30nm (**Figure 4.15**).

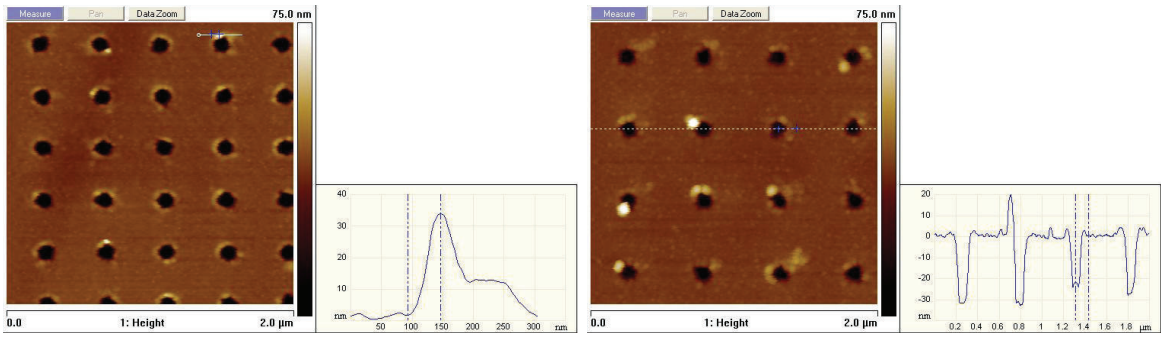

Figure 4.14 – AFM image of a hole array in 2nm Cr / 30nm Au with a period of 400nm (left) and 500nm (right) before the thermal treatment.

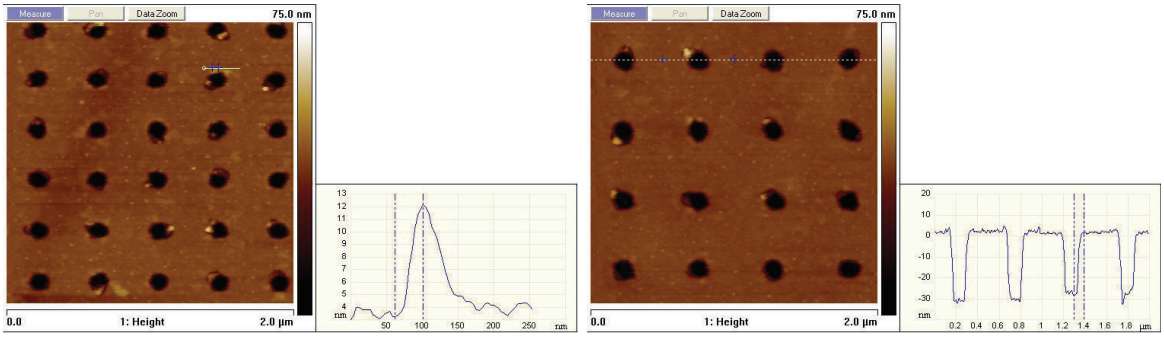

Figure 4.15 – AFM image of a hole array in 2nm Cr / 30nm Au with a period of 400nm (left) and 500nm (right) after the thermal treatment.

The investigation with the AFM showed that an additional thermal treatment improves the quality significantly.

4.3 Concluding remarks

It was shown, that structuring areas with sub-wavelength features, extending over mm^2 by means of EBL is possible if all time critical adjustments are optimized. Applying the standard area exposure, is very time consuming but feasible. If the feature is a circle array the elaborated dot exposure is preferable due to the enormous reduction of exposure time (cf. **Table 4.1**). Via a lift-off technique, plasmonic electrodes i.e sub-wavelength hole arrays in metal films extending over $3x3mm^2$ with a period down to 400nm and hole diameters down to 100nm are feasible. For arrays fabricated with the area exposure a wet chemical lift-off can be performed. In contrast for structures fabricated with the dot exposure mode the lift-off with a polymer has to be used, due to bad performance of the resist. The minimum Cr layer for a wet chemical lift-off was determined to be 0,5nm and for the lift-off with the polymer 2nm. Due to the enormous reduction in exposure time with the dot exposure mode, this was the method of use for structures characterized in the next section, unless otherwise specified. The additional annealing step yields a significant quality improvement of the structures.

Chapter 5

Characterization results of fabricated structures

In this chapter the fabricated metal films are characterized by AFM, SEM and optical spectroscopy. The metal films with hole arrays were fabricated with the dot exposure EBL mode, unless otherwise specified. The optical characterization was done by transmission and photoluminescence measurements also in combination with the polymer PTB7 (**Figure 5.1**).

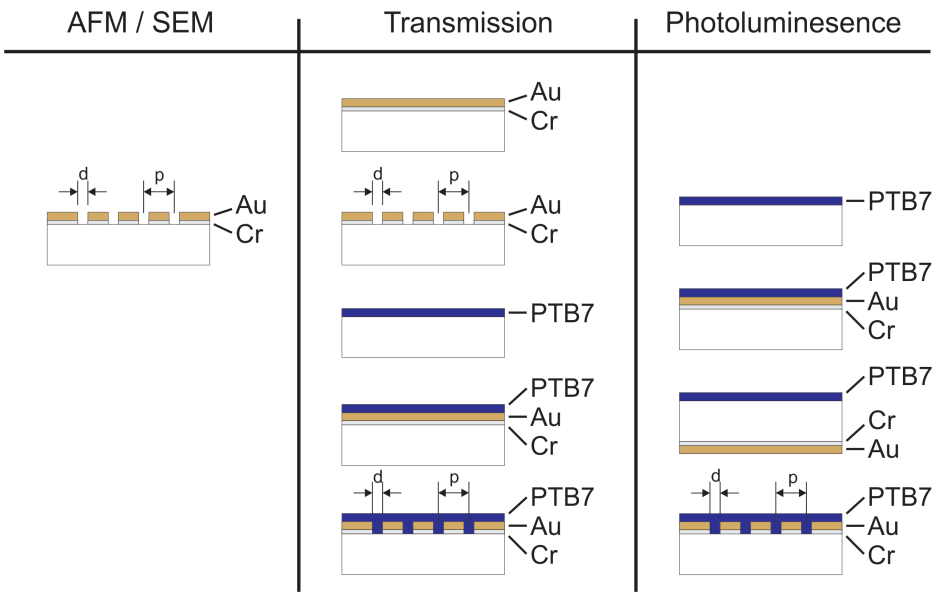

Figure 5.1 – Outline of different device configurations investigated in this chapter via AFM, SEM, transmission and photoluminescence measurements.

5.1 Topographical properties

The topographic profile of a metal hole array was investigated with the AFM. Different scan areas of a structure with 500nm period can be seen in **Figure 5.2**.

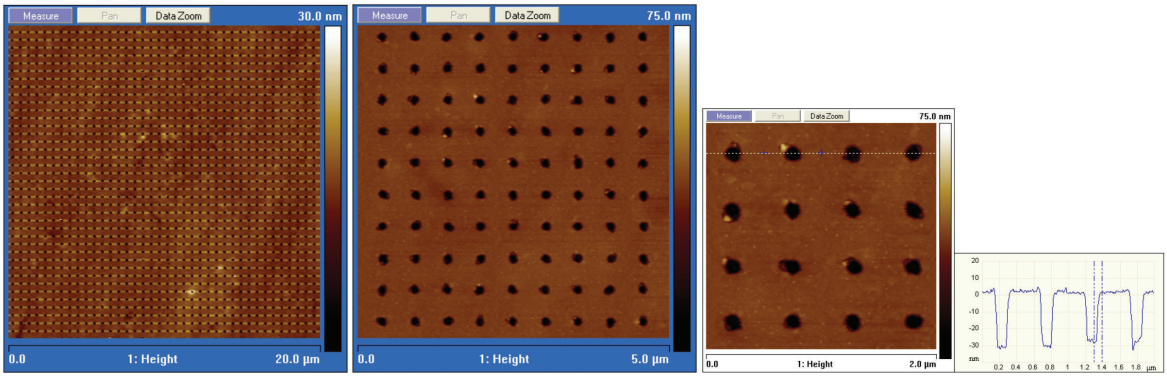

Figure 5.2 – 20x20μm^2, 5x5μm^2 and 2x2μm^2 scanned area with the AFM and a topographic profile over 4 holes in the 2x2μm^2 area.

In summary it can be seen, that the resist was removed in the lift-off process, confirming that the fabrication of this structures worked.

5.2 Transmission properties

The zero order transmission measurements were performed as explained in section 3.5.4 with the principle experimental setup illustrated in **Figure 3.12**. For measurements of scattered light the principle experimental setup with an integrating sphere was used (**Figure 3.13**).

5.2.1 Unstructured gold/chrome coatings on glass

Unstructured Au/Cr coatings of different thicknesses are the subject of investigation in this section. First the Au film thickness is varied with a constant thick Cr glue layer underneath. Second the influence of the Cr layer is shown by changing the Cr layer thickness.

5.2.1.1 Gold layers of different thicknesses

Different thick gold layers were prepared on glass by thermal evaporation. The glass first was coated with a 0,5nm thick chrome layer to promote adhesion between glass and Au. The transmission spectra of these Au coatings are compared with the transmission of glass covered with and without an Indium Thin Oxide (ITO) layer.

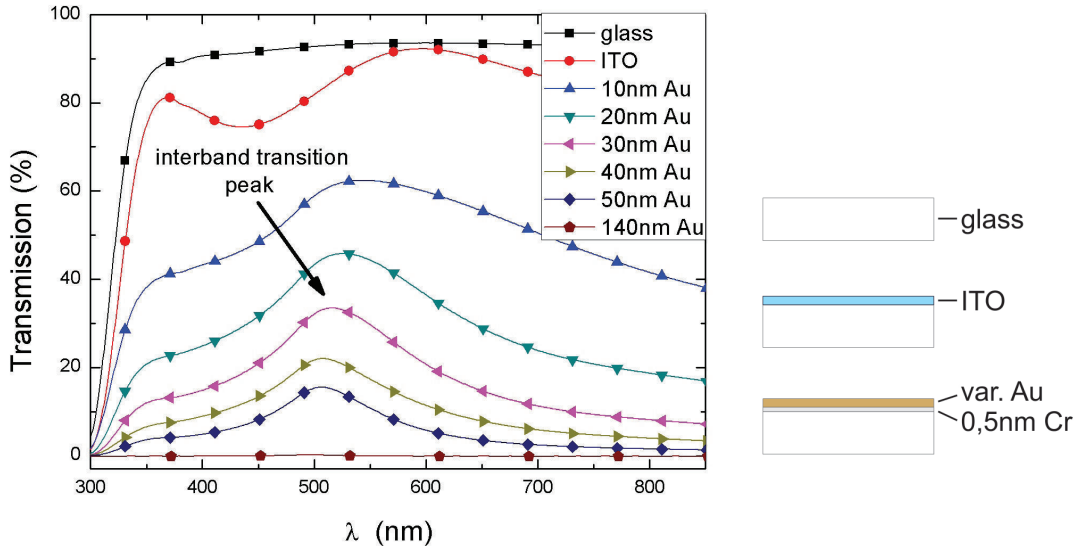

Figure 5.3 – Zero order transmission spectra of different Au coatings with a 0,5nm Cr adhesion layer on glass with the interband transition peak.

In **Figure 5.3** it can be seen that the glass has a constant transmission of about 90% in the visible range. In the ultraviolet (UV) region the glass strongly absorbs the photons, evident in the low transmission at a wavelength of λ=300nm. Two peaks are present in the spectrum of the ITO covered glass, one in the UV region and the other at about λ=600nm, but the average transmission can be specified to be about 80%. The gold coatings are all less transparent than the ITO. The transmission intensity has a characteristic peak at about 500nm. Almost no transmission was observed for the 140nm Au layer and therfore it is called optical thick. The peak positions and intensities of the optical thin layers are listed in **Table 5.1**. It can be noted, that the peak shifts to the red with decreasing layer thicknesses.

Table 5.1 – Peak positions and transmission intensities for the Au coatings from **Figure 5.3**
d ... Thickness of the Au layer on 0,5nm Cr / glass
p ... Peak position
T ... Transmission intensity at the peak

d / nm	p / nm	T / %
10	543	63
20	526	46
30	516	33
40	507	22
50	506	16

Peak position:
Mooradian et al. measured 1968 photoluminescence of metals [51]. This was explained by a radiative recombination between electrons in conduction-band states below the Fermi level and holes in the d-bands generated by optical excitation. Various authors explain this Peak with the interband transition of gold [54, 55].
An interband transition from the filled d-bands to empty states above the fermi level has for gold a minimum energy of 2,3eV [52]. This corresponds to a wavelength of 539nm which is in the blue part of the spectrum and suits well to the peak positions observed in this measurements. This results show that for thin Au layers the blue part of the spectrum interacts less with the material or its surface. Consequently in the bulk material the blue part can penetrate further into the material and thus can not be reflected out of it, leading to a stronger absorption in the bulk. The stronger absorption of the blue part gives gold its specific yellowish color since the complementary color of blue is yellow. This is the reason why gold mirrors are only used in the infrared region, preferable for the visible is silver which has its interband transitions at 3,9eV [52], that is in the UV and thus no strong absorptions in the optical occur.

Shift of the peak:
This peak is explained by other authors with the bulk plasmon resonance of a gold film [57]. The bulk plasmon resonance of Au has an energy of 9,01eV [52] which correspond to light in the UV region. Although this is based on a very simple model (formula 2.14) it doesn't account for contributions of the valence band. This contribution from the valence band are the aforementioned interband transitions and a more complex model of the bulk plasmon resonance would include an additional expression in the formula to describe a resonance at the interband transition energy. The shift of the bulk plasmon resonance peak with decreasing layer thickness to longer wavelength i.e. a decrease of the plasma frequency is known in metallic films [53]. There is no commonly accepted interpretation of this thickness dependency. It might be caused by a dependency of the electron density or the electron mass, the large number of surface atoms or maybe the influence of the substrate.
Since the shift of the bulk plasmon resonance is known it is not surprising that the interband transition peak shifts as well.

5.2.1.2 Influence of the chrome layer

As mentioned before gold has a low adhesion to glass surfaces. A glue layer of chrome is commonly used to promote adhesion [35]. The influence of different thick chrome layers under a 30nm Au layer on the transmission spectrum is presented in **Figure 5.4** and the spectral positions and intensities of the peaks are listed in **Table 5.2**.

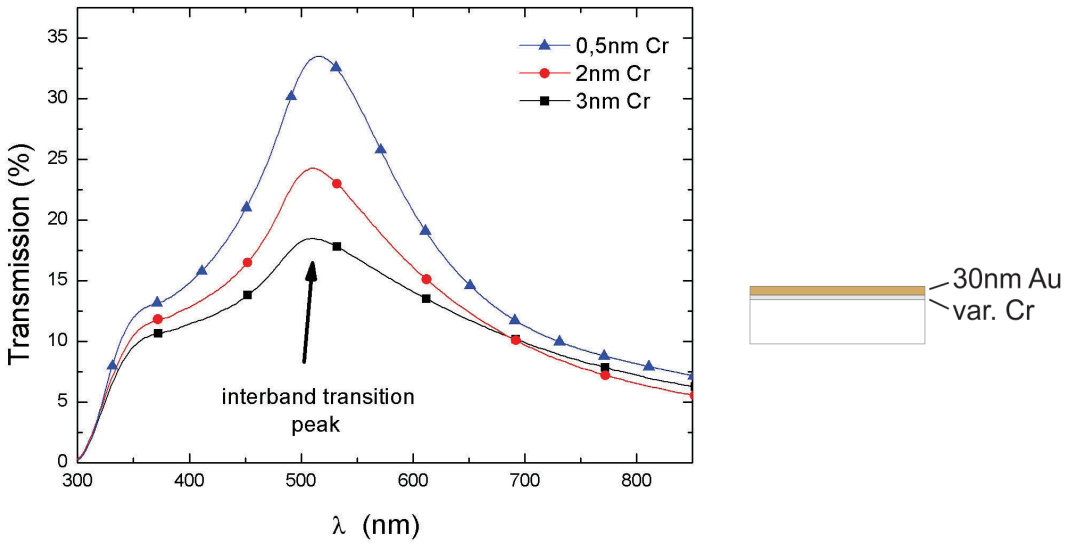

Figure 5.4 – Transmission spectra of different Cr layers on glass under a 30nm Au layer with the interband transition peak.

Table 5.2 – Peak positions and transmission intensities for different Cr coatings under a 30nm Au layer from **Figure 5.4**

d ... Thickness of the Cr layer
p ... Peak position
T ... Transmission intensity at the peak

d / nm	p / nm	T / %
0,5	516	33
2	511	24
3	509	18

It can be seen, that with an increased chrome layer, less light is transmitted and this is not an integral loss over the spectral region. The peak of transmission in the gold film coming from the interband transition is decreased. A shift is observable to shorter wavelength with increasing chrome layer.

The lower transmission can be explained by comparing the extinction coefficients from **Figure 2.1** which has a higher value for chrome. If using such a compound as semitransparent plasmonic electrode the chrome layer should be minimized to increase transparency of the electrode. An additional reason to minimize the chrome layer is that chrome is a bad material for SPPs, which can be seen in formula (2.25), the propagation length of SPPs. This propagation length is reduced due to the high imaginary part of the dielectric function of chrome visible in **Figure 2.2**. Alternatively and more conceivable the electrical resistivity of chrome is 125nΩm [49], which is much higher as for gold 22$n\Omega$m [50], therefore SPPs

which represent charge oscillations at the surface, thus moving conduction electrons, are more damped in chrome.

The minimization of the chrome layer is described in section 4.1.3.2. For a wet chemical lift-off a layer of 0,5nm Cr is sufficient and for a lift-off with the polymer a chrome layer of 2nm has to be applied to establish sufficient adhesion.

5.2.2 Sub-wavelength structured metal films

Sub-wavelength structured metal layers were fabricated as explained in chapter 4. The structure was a hole arrays with different geometric values as demonstrated in **Figure 5.5**.

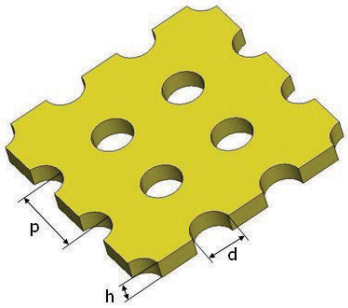

Figure 5.5 – Hole array in a metal film with the geometric values, p ... period, d ... hole diameter, h ... height of the metal film.

To know the fraction of hole area from the total area the Fill Factor (FF) in % is defined:

$$\mathrm{FF}(\%) = \frac{\text{area of holes}}{\text{total area}} \tag{5.1}$$

5.2.2.1 Optical thin gold/chrome coatings

The difference between optical thin and optical thick gold films can be made at a thickness of about 50nm. Thicker films reflect the major part of the incident beam and the film changes from semitransparent to opaque behavior.

5.2.2.1.1 Influence of the hole diameter on the far field

Structures with the same period of 500nm and height h=2nmCr/30nmAu, but different hole diameters d=160nm and d=250nm were produced, with the particular SEM image in **Figure 5.6**.

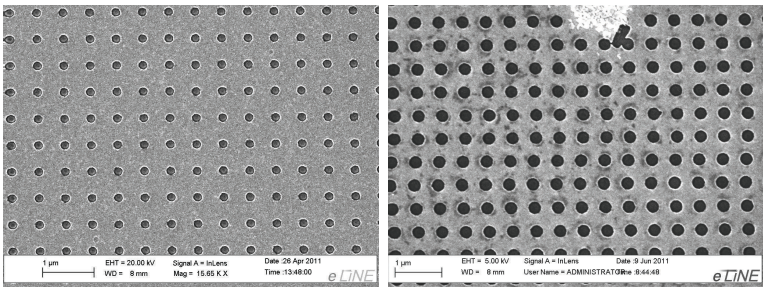

Figure 5.6 – SEM images of structures with the corresponding transmission spectra in **Figure 5.7**, left: d=160nm, right: d=250nm

In the SEM image on the right side at the top an error can be seen. A contamination can be identified by the bright areas, which may have occurred prior to the spin coating process. Most likely that's why the resist pillars at this points were not able to establish a good adhesion to the substrate and were tilted during development. Near this bright areas, one tilted pillar got stuck at the surface and the profile were transferred in the metal coating.

In **Figure 5.7** the transmission spectra are compared. It can be seen, that a characteristic peak appears with the structured samples at about 740nm and it stays at the same position with changing hole diameter. Further there is an integral increase of transmitted light for the structure with larger holes visible.

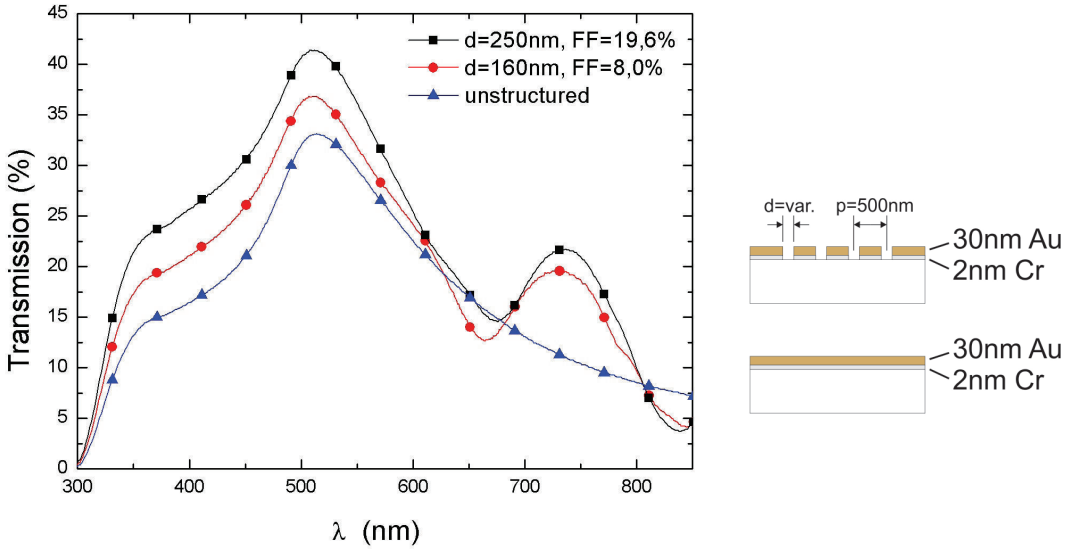

Figure 5.7 – Transmission spectra of hole arrays with a period of 500nm and different hole diameters of d=250nm and d=160nm in a metal coating of 2nm Cr and 30nm Au on glass and the spectrum of the unstructured metal coating.

This increase is caused by the larger fraction of hole area resulting in a higher FF for the structure. The latter has an increased value of 19,6% compared to 8%. Consequently

the characteristic peak at 740nm is not influenced by the hole diameter. In the next section it will be seen that the general shape of the transmission spectrum depends on the period.

The hole diameter changes the modes of the Localized Surface Plasmons (LSPs) located in the holes, which can be compared to the LSPs on nanoparticles shortly introduced in section 2.4. These localized modes are characterized by a high field strength within the holes making them a promising candidate for sensing and non-linear optical applications [58].

5.2.2.1.2 Influence of the period on the far field

First structures with a period larger than the wavelength of visible light were produced. These structures were fabricated in the beginning of this work and therefore fabricated with the area exposure. Since the period is quite large the overall exposure time was acceptable. A wet chemical lift-off was applied.
The SEM images of the fabricated structures with the same hole diameter d=200nm and a period of 1μm and 2μm can be seen in **Figure 5.8**. In the vicinity of some holes, shadows are visible. This shadows in the SEM images are residues of resist due to a not optimized wet chemical lift-off used in the beginning of this work.

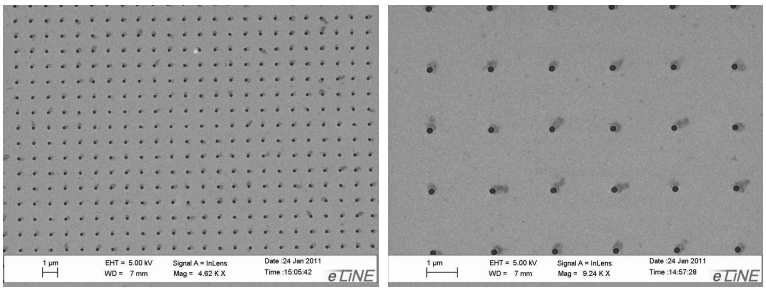

Figure 5.8 – SEM images of structures with the corresponding transmission spectra in **Figure 5.9**, left: p=1μm, right: p=2μm

The transmission spectra of the structured metal films as well as the spectrum of the unstructured film are shown in **Figure 5.9**. An integral increase of transmitted light can be observed for decreasing periods. Furthermore there is a slight modulation present for wavelength larger than 600nm in the spectrum of the 1μm period structure. The increase in transmission for the p=1μm structure is caused by the higher FF of 3,1% compared to 0,8% for the p=2μm structure. The slight modulation in the spectrum of the p=1μm structure indicates a spectral change if the period approaches the wavelength of the light used to investigate.

Structures with this periods didn't show significant changes in the transmission spectra in the optical range compared to the unstructured Au film. Thus no significant additional interaction of the electromagnetic wave and the structure is present. Therefore the period

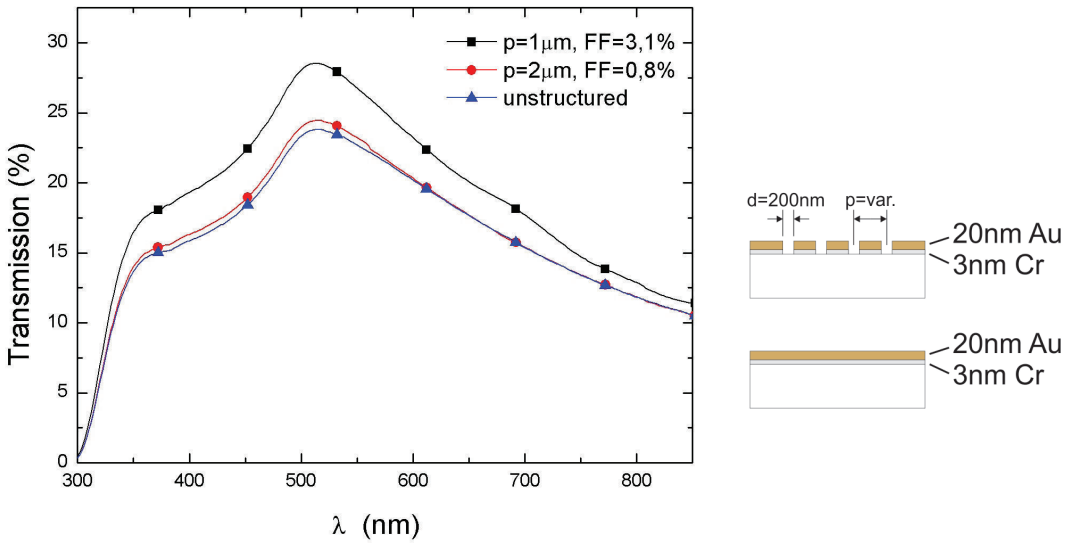

Figure 5.9 – Transmission spectra of hole arrays with 200nm diameter holes and different periods of $1\mu m$ and $2\mu m$ in a metal coating of 3nm Cr and 20nm Au on glass and the spectrum of the unstructured metal coating.

of the hole array was decreased down to the sub-μm range. This generated new problems concerning the overall exposure time. As explained in section 4.1.1 the exposure mode was changed to a dot exposure to reduce the overall exposure time to an acceptable limit. After overcoming all this technical problems and optimizations, structures with a period of 400nm, 500nm and 750nm were produced. SEM images are shown in **Figure 5.10**.

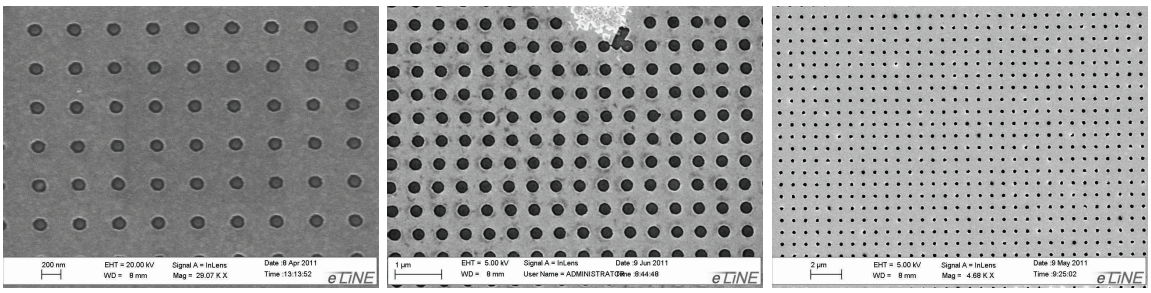

Figure 5.10 – SEM images of structures with the corresponding transmission spectra in **Figure 5.11**, left: p=400nm, middle: p=500nm, right: p=750nm

Transmission spectra of metal films perforated with hole arrays of periods in the sub-μm and additionally the unstructured film can be seen in **Figure 5.11**. Beside the characteristic gold peak at about 500nm several peaks are showing up. The spectral positions of these peaks are listed in **Table 5.3**.

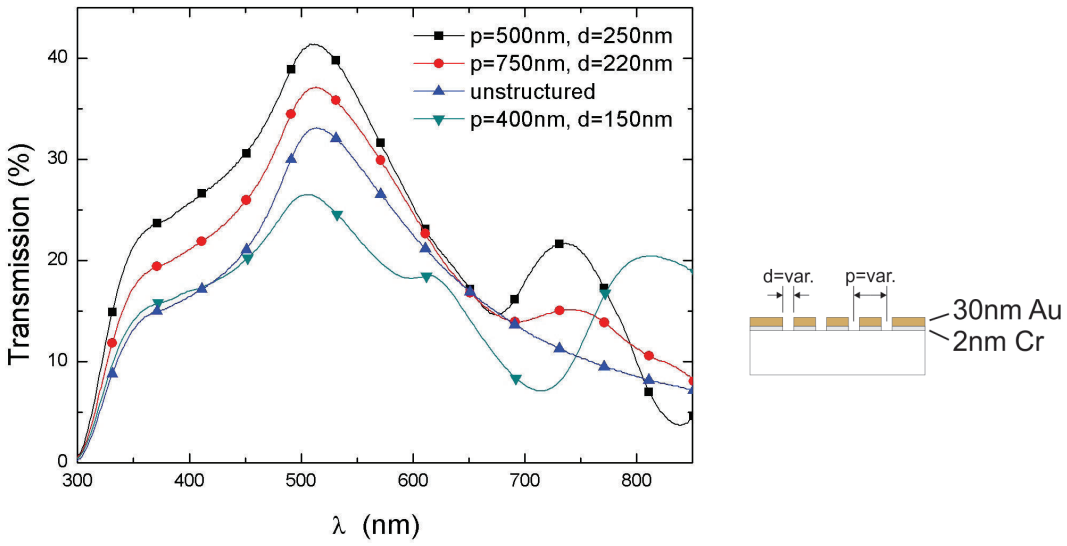

Figure 5.11 – Spectra of metal coatings (2nm Cr and 30nm Au) with and without a hole array of different periods and hole diameters on glass.

Table 5.3 – Peak positions and FFs for different structured Au coatings from **Figure 5.11**
p ... Period
FF ... Fill factor from (5.1)
P_x ... Spectral position of peak

p / nm	FF / %	P_1 / nm	P_2 / nm	P_3 / nm
400	11,1	505	616	812
500	19,6	513	736	-
750	6,8	512	743	835

The different peak positions of the spectra result from different periods, which is the same behavior as for optical thick metal films [1]. Conspicuous is the small transmission of the structure with the period of 400nm. Referring to the FF, the transmission intensity should be between the 500nm and 750nm period. The data in literature for optical thin metal films is rare, but one group published a suppressed transmission for ultrathin metal films with small periods. They produced hole arrays with an optical interference lithographic process. The geometric values were: p=300nm, d=200nm and h=20nm Au with 2nm Cr on glass. They explained the suppression of the transmission compared to the pristine metal film with an excitation of a short range surface plasmon and thus a strong absorption [59].

The formula for the resonances of SPPs (2.31) is not applicable for optical thin films. This approximation is only valid for optical thick films at which the SPPs on both side are independent. For thin films the electromagnetic fields of both sides of the film interact [27].

5.2.2.2 Optical thick gold/chrome coatings

In literature there are a lot of reports about optical thick sub-wavelength structured metal films. This all began in 1998 when Ebbesen *et al.* first reported Extraordinary Optical Transmission (EOT) through sub-wavelength hole arrays [1]. They measured zero order transmission spectra of metal films with square arrays of sub-wavelength holes, drilled by a focused ion beam. Extraordinary optical transmission was found in different metal films. So why is the transmission called extraordinary?
This is related to the current understanding of transmission through small holes, the standard aperture theory formulated by Bethe [60]. This theory predicts that the transmission for one hole scales like:

$$T(\lambda) \backsim \left(\frac{r}{\lambda}\right)^4 \tag{5.2}$$

$T(\lambda)$ is the transmission, r is the radius of the hole and λ is the wavelength. In the case of a hole array the multiplication with the FF, predicts the transmission of the sub-wavelength hole array.

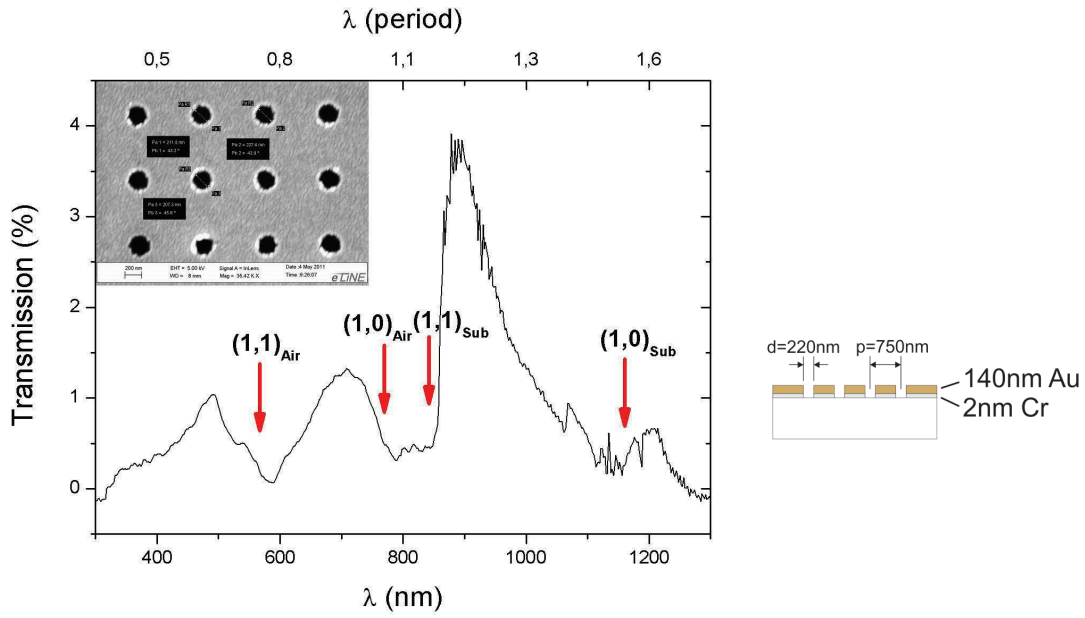

Figure 5.12 – Spectrum showing Extraordinary Optical Transmission (EOT) of a hole array with p=750nm, d=220nm (FF=6,8%) in a metal coating of 2nm Cr and 140nm Au on glass with the SEM image of the structure in the upper left corner. The arrows indicate the SPP resonance wavelength on a sub-wavelength hole array on the air and substrate interface with the grating orders (n, m).

In **Figure 5.12** a transmission spectrum of a perforated gold film with a thickness of 140nm above a 2nm thick chrome layer on glass can be seen. The hole diameter is 220nm with a period of 750nm. A characteristic property of such spectra is the small transmission at which the wavelength equals the period. Before and after this point two peaks are showing

up, although the last peak at about 1200nm is very small. The transmission at λ=900nm estimated with Bethe theory with (5.2) and the calculated FF from (5.1) of 6,8% leads to a transmission of only 0,0015%. But in **Figure 5.12** it can be seen that the transmission at 900nm is almost 4%.
The breakdown of Bethe theory points out that the array itself has to be treated as an active element and not just a geometrical object in the path of the beam. EOT was only observed in metal films and the angular dependency of the zero order transmission spectra behave like light coupling with SPs in reflection. Therefore Ebbesen assigned the EOT mechanism to SPs excited on one side, coupled through the holes to the other side and re-radiated. An investigation concerning the geometrical values of the array showed that the periodicity determines the position of the peaks and this position is almost independent of the kind of metal, the hole diameter d and the metal thickness h. The aspect ratio of the holes $\frac{h}{d}$ determines the width of the peak. For $\frac{h}{d} = 0,2$ very broad peaks were seen and for $\frac{h}{d} \approx 1$ the maximum sharpness was observed [1].

Various different transmission spectra can be found in literature of optical thick sub-wavelength hole arrays. This high diversity is due to the dependency on a lot of variables like the main geometrical values, the period p, the hole diameter d and the metal thickness h, as well as the hole shape, the type of lattice (square, hexagonal,...), the kind of metal and the dielectric environment on both sides of the metal [61, 62, 63, 64].

In section (2.4.4) the resonance wavelength of SPPs on a 2dim periodic array is deduced. The calculated wavelength through formula (2.31) for different grating orders are listed in **Table 5.4** with the spectral positions indicated by arrows in **Figure 5.12**.

Table 5.4 – Calculated resonance wavelength (2.31) of SPPs by interaction with a 2dim periodic array in a gold film
(m,n)$_{Interface}$ ... grating orders m, n at the substrate or air interface
λ ... expected wavelength

SPP	λ / nm
(1,0)$_{Sub}$	1160
(1,1)$_{Sub}$	842
(1,0)$_{Air}$	769
(1,1)$_{Air}$	567

The calculation was done with the dielectric constant of air set to $\epsilon_d = 1$. For the substrate $\epsilon_d = n^2$, with the refractive index $n = 1,517$ of the substrate was used [65]. The dielectric function of gold ϵ_m was described by the data plotted in **Figure 2.2**. The chrome layer was neglected in this calculation since it is only 2nm thin.

In literature there are different interpretations of formula (2.31). Some authors correspond this wavelength to the peak positions of the transmission spectrum [21, 22], others predict transmission minimums [25, 26]. This controversy reflects that this simple analytical expression is not capable to describe the complicate processes involved. Only computer simulations can produce a precise image of the electrodynamics which is going on when photons interact with nanostructured materials. This can be for example Finite Difference Time Domain (FDTD) simulations, which are computational electrodynamic modeling techniques where the time dependent Maxwell equations are solved.
In summary it can be said that formula (2.31) is a very simple model upon other totally excluding the thickness of the metal. However, in **Figure 5.12** it can be seen, that the excitation wavelength of SPPs corresponds to the minimums of the transmission spectrum. For the optical thin metal films no conclusion can be made with this formula because the electromagnetic fields of both surfaces interact strongly [27].

5.2.2.3 Concluding remarks optical thick and thin coatings

Sub-wavelength structured optical thick metal coatings give rise to EOT-peaks as shown in the last section. These peaks are extraordinary only by comparison with the expected transmission from standard aperture theory for small holes. The maximum transmission of 4% at λ=900nm is low compared to the thin metal films (**Figure 5.13**).

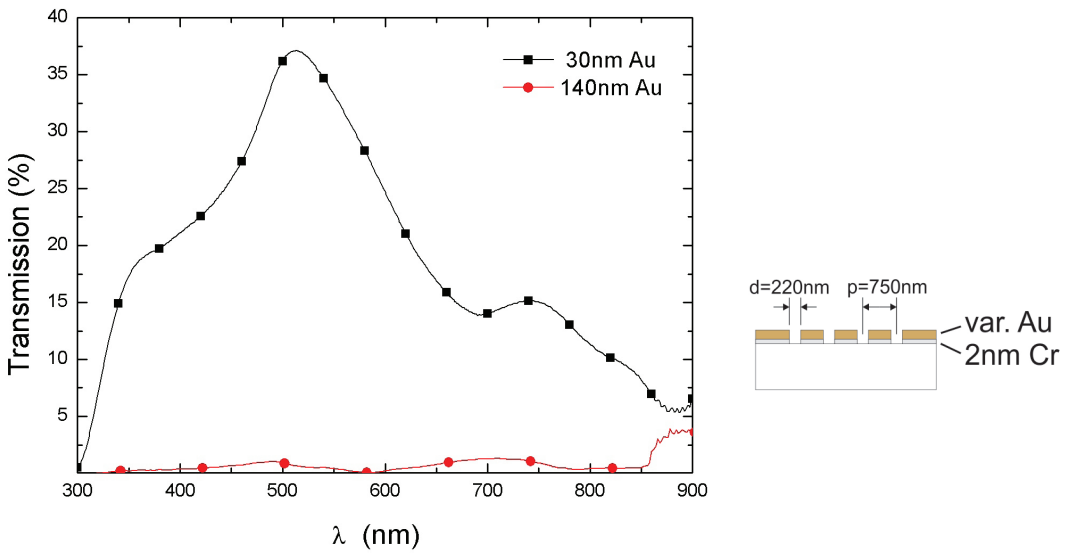

Figure 5.13 – Comparison of optical thick and thin perforated gold/chrome coatings: Hole arrays with p=750nm and d=220nm (FF=6,8%) in 30nm and 140nm thick Au coatings with 2nm Cr adhesion layer on glass.

Concerning transparency, thin metal coatings are preferable for the use as transparent

electrode due to the higher transmission. Optical thin films show high transparency as well without a structure (cf. **Figure 5.3**). With the advantage of a low sheet resistance compared to ITO they were used as semitransparent electrode for organic solar cells [66]. To have a similar sheet resistance as ITO coatings, the Au layer can be as thin as 10nm [67].

With transmission measurements only far-field effects can be considered. Within the use in thin film devices the role of SPs and near-field effects are also important. Optical thin metal films structured with a sub-wavelength hole array show characteristic peaks at wavelength larger than 600nm. (cf. **Figure 5.11** and **Table 5.3**).

5.2.3 Scattering of structured and unstructured metal films

To get an idea how much transmitted light get scattered from a sub-wavelength hole array, measurements with an Integrating Sphere (IS) were performed. Therefore the sample was placed directly in front of the IS, as schematically shown in **Figure 3.13**. This means that not only the zero order beam was detected, but rather all the light which was leaving the sample in directions up to 90° with respect to the zero order beam. In **Figure 5.14** the spectra of an unstructured and a structured film with the geometric values p=500nm, d=250nm and h=2nmCr/30nmAu, with and without an IS in the detected beam is compared.

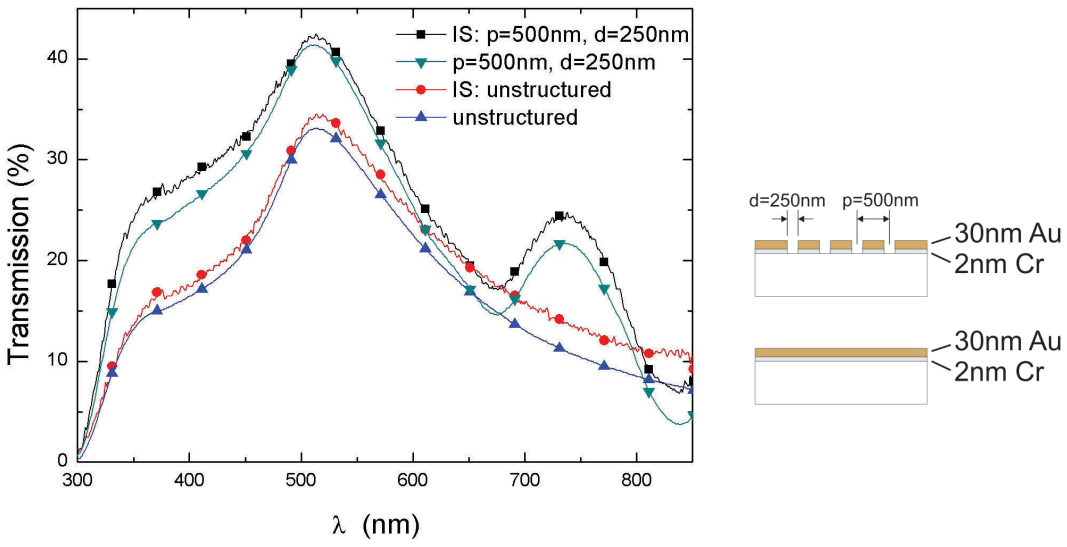

Figure 5.14 – Transmission spectra of an unstructured and a structured (p=500nm, d=250nm, FF=19,6%) metal film of 2nm Cr and 30nm Au on glass with and without an Integrating Sphear (IS).

A small integral increase of transmission can be seen with the IS for the structured as well as for the unstructured film.

The increase of transmission with the unstructured film is generated from scattering at the metal interfaces i.e. surface roughness or as well scattering in the metal. Thinking about the millions of holes in the perforated film one could expect an increase of scattering of the incident beam, with the perforated film. But the results lead to the conclusion, that the sub-wavelength hole array in optical thin films doesn't scatter the incident beam noticeable more than unstructured films.

5.2.4 Absorbance PTB7

To investigate the metal films in combination with a polymer, PTB7 (Poly[[4,8-bis[(2-ethylhexyl)oxy]benzo[1,2-b:4,5-b']dithiophene-2,6-diyl][3-fluoro-2-[(2-ethylhexyl) carbonyl]thieno[3,4-b]thiophenediyl]]) was used. The samples were prepared as explained in section 3.4 and the chemical structure of PTB7 can be seen in **Figure 5.15**.

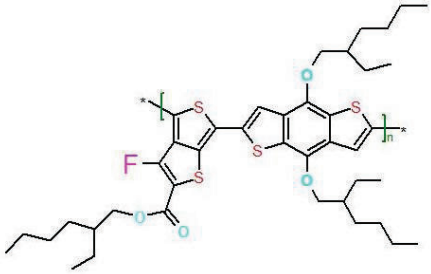

Figure 5.15 – Chemical structure of PTB7 (taken from [68])

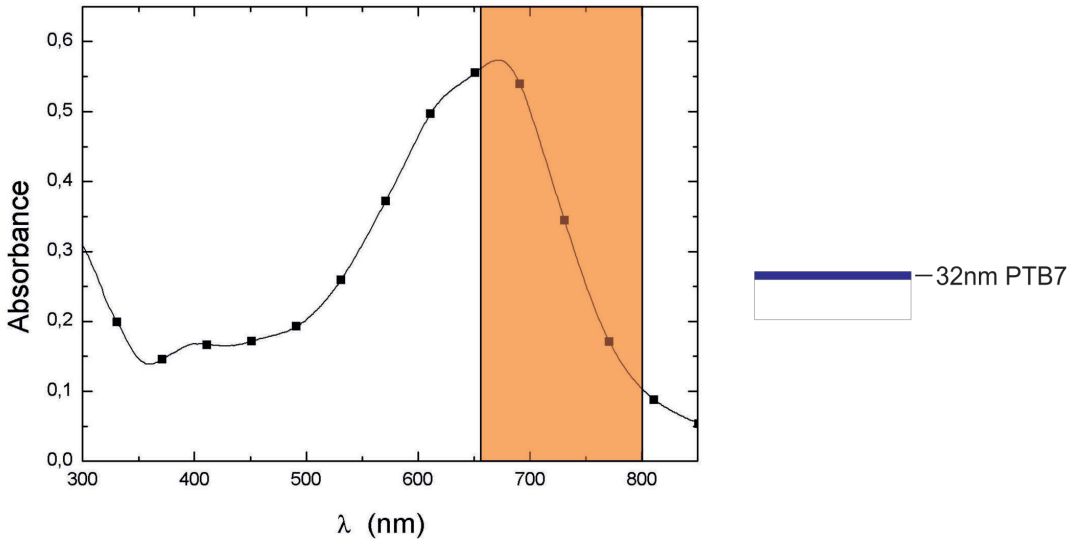

Figure 5.16 – Absorbance of a 32nm PTB7 layer on glass. The shaded area demonstrates the spectral range of resonances from a 500nm period sub-wavelength hole array.

To calculate the absorbance with (3.3) the transmission I of a 32nm thick PTB7 film on a glass substrate and the transmission I_0 only through the substrate were measured and can be seen in **Figure 5.16**. Resonances due to the periodic hole array of thin metal films investigated in section 5.2.2.1 appear at wavelength larger than 600nm. The area where resonances of a 500nm period sub-wavelength hole array appear is shaded in the figure. To overlap the resonances of the metal structure and the polymer an active material with absorption in this energy range is required. PTB7 fulfills this requirements because it is a low-band-gap polymer with a bandgap of 1,6eV [69]. This leads to a strong absorption from 550nm to 750nm, with the peak of absorption located at 672nm.

5.2.5 Unstructured metal film vs. glass coated with PTB7

Transmission through a 2nm Cr / 30nm Au film on glass with and without a 32nm thick PTB7 layer was recorded. **Figure 5.17** as well includes the transmission spectrum of a 32nm PTB7 layer on glass. The transmission through the PTB7 coating on the Au film shows a interesting property. One would expect that an additional layer of a substance on the Au film weakens the transmission, since the additional layer itself absorbs.

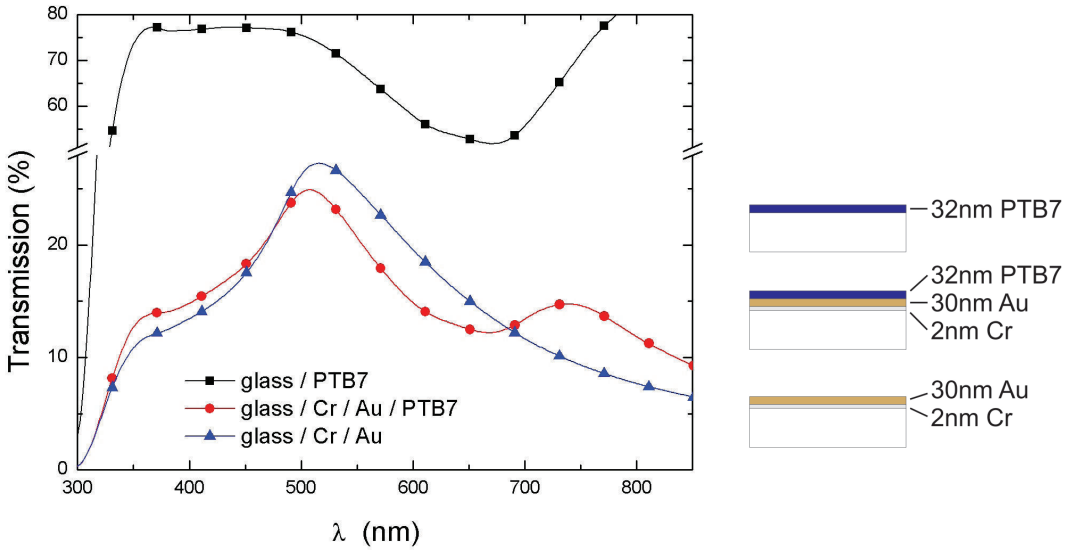

Figure 5.17 – Transmission spectrum of a 32nm PTB7 film on glass and the transmission through a 2nm Cr / 30nm Au covered glass, coated with and without a 32nm PTB7 film.

In the spectrum it can be seen that in the region below 475nm and above 684nm the Au / PTB7 composite transmit more light compared to the bare Au film. An additional peak of transmission appears at 738nm. The interband transmission peaks shifts from 515nm to 507nm with the additional PTB7 layer.

In literature similar data for adsorbed AGFAII dye molecules on an optical thin Au film can be found. It was shown that the transmission spectra of such composite systems are in general determined by coherent light scattering of the molecules in the layer and an interference of this scattered light with the incident beam [70]. From this it follows, that not only the imaginary part of the dielectric function determines the transmission, but the shape of both, the imaginary and the real part determines the transmission through the composite. Such spectra cannot be constructed from the transmission spectra of the initial system and the deposited film alone [71]. In conclusion it can be seen that the transmission of the gold film can be increased in a limited spectral range close to the resonances of the PTB7 layer. In [70] it is shown by means of electromagnetic theory of the optics of stratified media that the excitation of SPs is not a necessary ingredient as discussed by other authors for metallic nanoparticles coated with dye molecules [72].

To visualize the enhancement induced by the interdependency of the two layers, the relative transmission $\frac{I}{I_0}$ is displayed in **Figure 5.18**. This refers to the transmission I through a sample covered with a PTB7 layer normalized to the transmission of only the underlying layers I_0. In this illustration the intensity I_0 of the underlying layer is in one case the transmission through a glass substrate and in the other case the transmission through a glass covered with a 2nm Cr / 30nm Au layer.

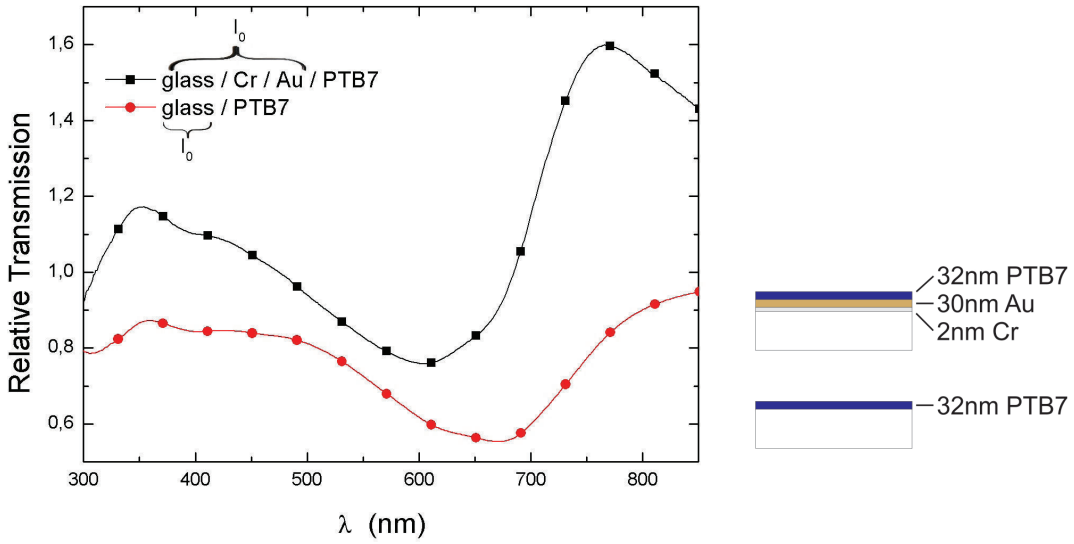

Figure 5.18 – Transmission spectrum of a 32nm PTB7 film on a glass substrate, normalized to the transmission of the glass and transmission spectrum of a 32nm thick PTB7 film on a metal film, normalized to the transmission of the metal film on glass.

It can be seen that the PTB7 layer enhances the transmission of the bare Au-film at 765nm about 1,6 times.

To calculate the absorbance from the polymer layers of **Figure 5.18** formula (3.3) is used and the results are presented in **Figure 5.19**. The absorbance for the PTB7 layer on glass is, like it should be the same as in **Figure 5.16** with the highest absorbance at 672nm. In contrast the peak of absorbance of the Au / PTB7 composite on glass is at 604nm. Conspicuous are the negative values of the absorbance. This is the result of its logarithmic nature caused by the relative transmission, which exceeds 1. In the composite system there are two resonances present, the first in the Au film coming from the interband transition located at 515nm and the second is the absorption maximum of the PTB7 film at 672nm. The resonance of the composite system is located at about the middle of these two resonances at 604nm. The absorbance with negative values cannot be physically correct since this would be an amplification in the layer which would be a brilliant material, but physically it is not possible, due to the energy conservation law. Physically correct can only be considered the absorbance of the PTB7 film on glass. The glass is macroscopically thick and can be assumed as independent to the PTB7 layer.

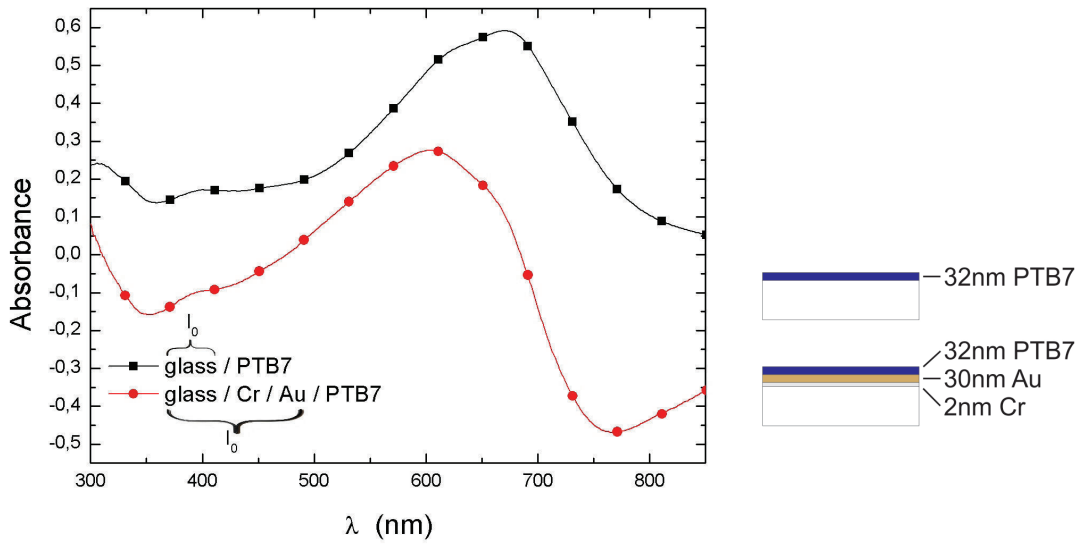

Figure 5.19 – Absorbance of a 32nm thick PTB7 film on glass and absorbance of a 32nm PTB7 film on a 2nm Cr / 30nm Au layer on glass with negative values due to interdependency of the Au film and the PTB7 film.

These measurements and illustrations as well as the above mentioned publications [70, 71], show that the Au and the PTB7 layer are not independent of each other. As a consequence the absorbance of the PTB7 with the gold layer underneath shown in **Figure 5.19** is **not correct**. With this kind of measurements, conclusions about the absorbance of only the polymer layer above the Au layer cannot be made because apparently the properties of the layers when interacting with light change in the compound system.

To make a statement about the absorbance in the layer a device would be necessary, i.e. an organic solar cell (OSC), where the generated current of the OSC as a function of the wavelength can be recorded. This is the Internal Quantum Efficiency (IQE) of an OSC. Even in this case the conclusion can only be made about the collected charge carriers and not about the absorbance itself.

5.2.6 Sub-wavelength structured metal films coated with PTB7

Two of the already presented sub-wavelength structured metal films in section 5.2.2.1.2 were coated with a 30nm PTB7 film.

Transmission through a 2nm Cr / 30nm Au sub-wavelength structured film with the geometric factors p=500nm, d=250nm, with and without a 30nm PTB7 film on it, are shown in **Figure 5.20**. The transmission in a certain wavelength range is enhanced with the additional PTB7 layer on it. This is a similar behavior as it was seen for unstructured metal films as presented before. The spectrum shows a shift of the interband transmission peak from 513nm to 507nm. This agrees also with the shift of the unstructured PTB7 covered sample shown before. In contrast the second transmission peak of the PTB7 coated sample appears at 782nm, which is an increased value compared to the unstructured metal film.

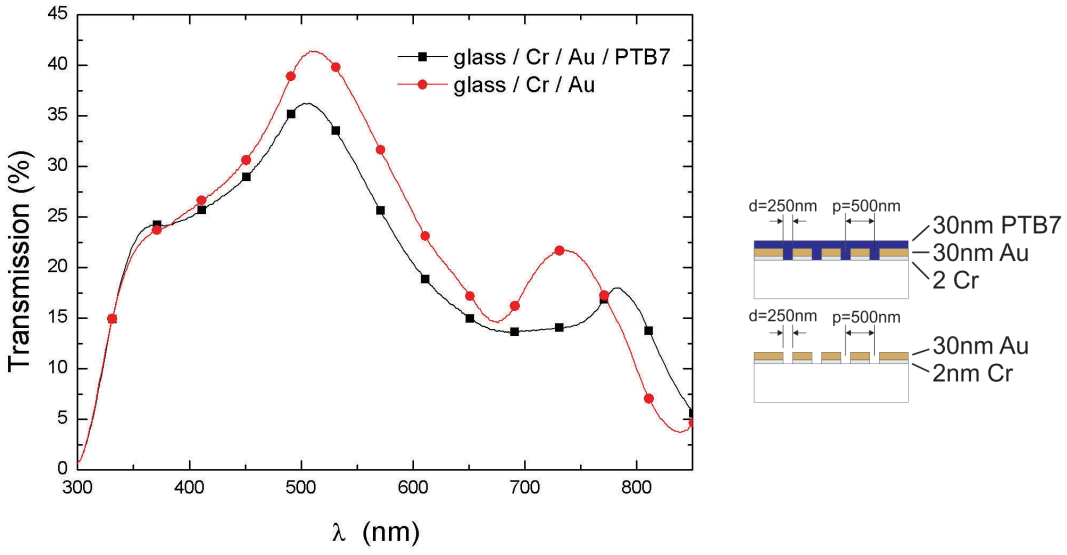

Figure 5.20 – Transmission through a sub-wavelength (p=500nm, d=250nm, FF=19,6%) structured 2nm Cr / 30nm Au layer on glass and transmission through this structure coated with a 30nm PTB7 layer.

The same metal film with a hole array of p=750nm, d=220nm was measured and the transmission is shown in **Figure 5.21**. As well this structure was coated with a 30nm PTB7 film. The 750nm period structure shows almost the same interband transmission peak shift from 512nm to 507nm. Further the second transmission peak of the PTB7 coated sample appears at 810nm, which is a further increased value.

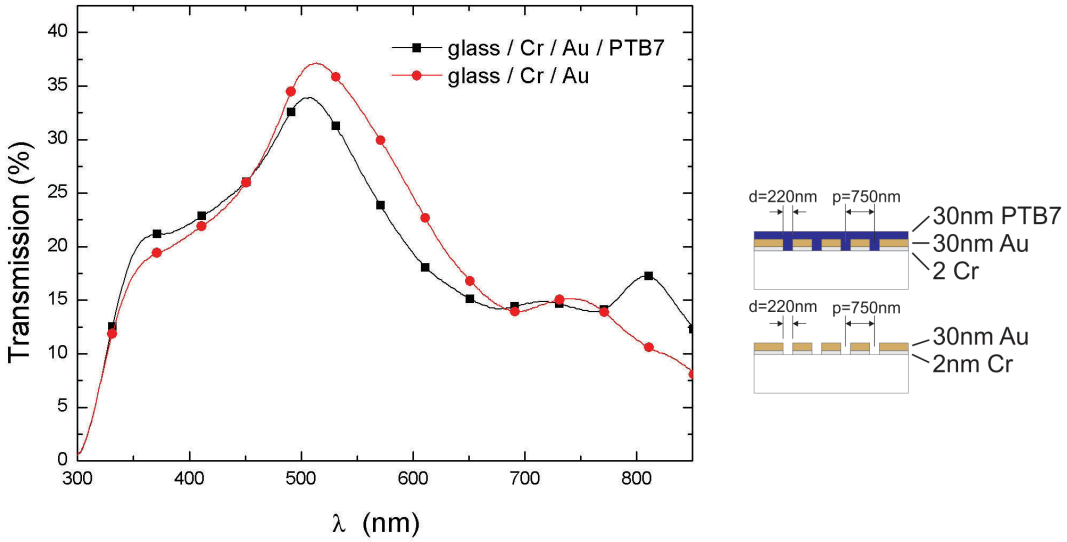

Figure 5.21 – Transmission through a sub-wavelength (p=750nm, d=220nm, FF=6,8%) structured 2nm Cr / 30nm Au layer on glass and transmission through this structure coated with a 30nm PTB7 layer.

In literature only data for optical thick sub-wavelength perforated metal films coated with dye molecules was found. Additional to the EOT peaks arising from the hole array a peak at wavelength at which the molecule absorbs strongly appear. The phenomenon is called *Absorption-Induced Transparency* (AIT) [75]. To investigate the system they placed the sample between 2 crossed polarization filters and the AIT transmission peak was still present. This is a evidence of an additional mechanism that lose the polarization information. That can be a coupling of light to SPs. That SPs play a key role was further confirmed with structured tungsten films, which cannot support SPs in this wavelength range, due to its dielectric function [76]. With tungsten as metal the AIT transmission peak was almost not present. Further they showed that it is not necessary to provide a periodic arrangement of the holes, the AIT peak also appears with randomly distributed holes in the metal. This means that localized SP modes play a key role.

5.3 Photoluminescence properties

Photoluminescence measurements were performed as explained in section 3.5.5 with the principle experimental setup illustrated in **Figure 3.14**. The layer thickness of the polymer layer were determined with a profilometer by taking the average value of three different positions on the sample. All the samples were excited at a wavelength of 680nm which is near the peak of absorbance of PTB7 at 672nm. The second monochromator, in the recording beam, scanned a spectral region from 700nm to 900nm in which the PL peak of PTB7 arises.

5.3.1 Unstructured metal film vs. glass coated with PTB7

The PL were measured of a 32nm PTB7 film on glass with and without a 2nm Cr / 30nm Au layer in between. To exclude direct reflection at the Au layer, the PL of only a 2nm Cr / 30nm Au layer on glass was measured as well (**Figure 5.22**).

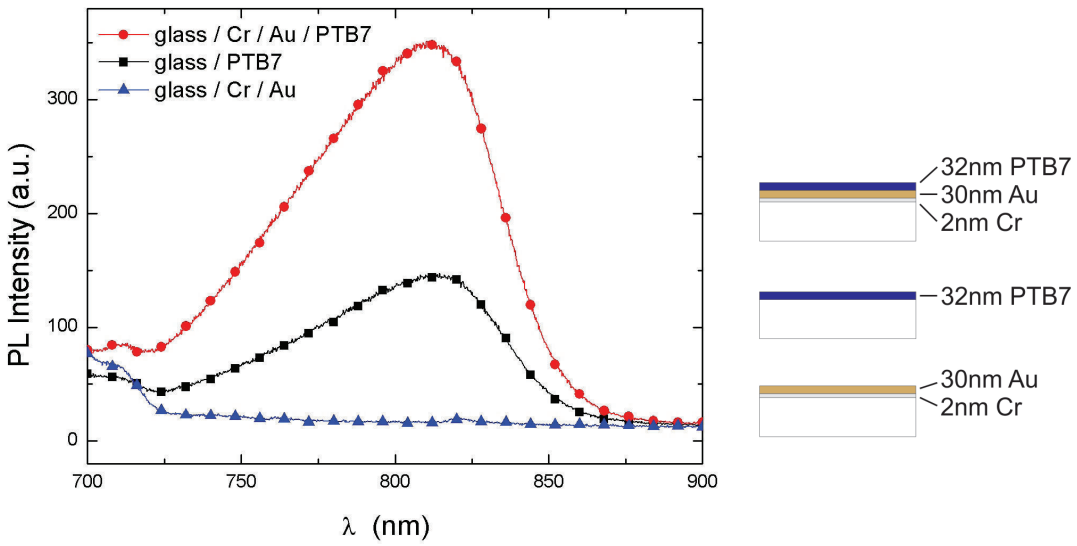

Figure 5.22 – Photoluminescence of a 32nm PTB7 film on glass with and without a 2nm Cr / 30nm Au layer in between and PL of the bare Au layer. All samples are excited at a wavelength of 680nm.

It can be seen that the bare Au layer doesn't generate a noticeable signal, confirming that almost no direct reflected light reaches the detector. The PL signal of the PTB7 film on glass peaks at 814nm with 147 counts in the detector. In contrast the PL signal of the PTB7 film above the Au layer peaks at 811nm with 352 counts. This is an enhancement of 2,4 times with the additional Au layer.
An enhanced PL signal was measured with an additional metal layer underneath. This can be for various reasons:

1. **Difference in the amount of fluorescent material**
   Due to an experimental error, different thick PTB7 films on glass and on the Au layer would lead to effective more fluorescent material. This means more molecules can be excited, which will radiate effectively more photons. This case can be excluded, since the PTB7 films have the same thicknesses of 32nm each.

2. **Reflection at the metal layer**
   The incident beam first passes the PTB7 film and one fraction gets absorbed, generating excitons in the PTB7 film. The excitation wavelength was chosen at 680nm, near to the maximum absorbance of PTB7. This means about half of the incident light (cf. **Figure 5.18**) gets absorbed by passing the first time through the PTB7 film. Since the Au layer is only 30nm thick, one part of the light is transmitted, another part is absorbed in the metal and another part gets reflected back. The reflection for bulk Au would be 95% for wavelengths bigger than 680nm [56]. This reflected light passes the PTB7 film once again and can excite PTB7 molecules. To estimate the exact proportions of reflected light additional experiments would be necessary.
   Since the molecules emit the PL isotropic in all directions, PL light reflected at the Au layer hits the detector as well.

3. **Changes in recombination rates**
   The decay of an excited state may take place as radiative Γ with emission of light or non-radiative k_{nr} with no emission of light. The recombination rate is the sum of both. The PL lifetime is the inverse of the recombination rate (i.e. $\tau_{PL} = \frac{1}{\Gamma + k_{nr}}$). The increase of the recombination rates, this goes along with the decrease of the PL lifetime can enhance the PL signal as well.

In the following it will be shown that the only remaining possibility is that the recombination rates change.

5.3.2 PTB7 coated metal films with and without a dielectric spacer

To understand the origin of the enhanced PL signal with the additional Au layer underneath, a further experiment was performed. This enhancement could arise from reflection at the metal surface or other effects due to the direct contact of the two layers. To separate these contributions, samples with and without a dielectric spacer were prepared. Microscope cover glasses were used as a spacer. This are 150μm thin glass slices, which are used in optical microscopy.

The cover glasses were thermally evaporated with 2nm Cr and 30nm Au. The metal covered side and on other samples the backside were plasma activated and then coated with a PTB7 layer as explained in section 3.4. To simplify the handling and prevent scratches

at the metal coating on the backside of the cover glass, the samples were fixed on ordinary glass substrates. These samples including a reference PTB7 film were excited at 680nm and the PL was recorded. Measurements with the cover glass samples fixed on glass resulted in not reproducible data. The removal of the glass and measurements of only the prepared cover glasses worked and the data recorded can be seen in **Figure 5.23**.

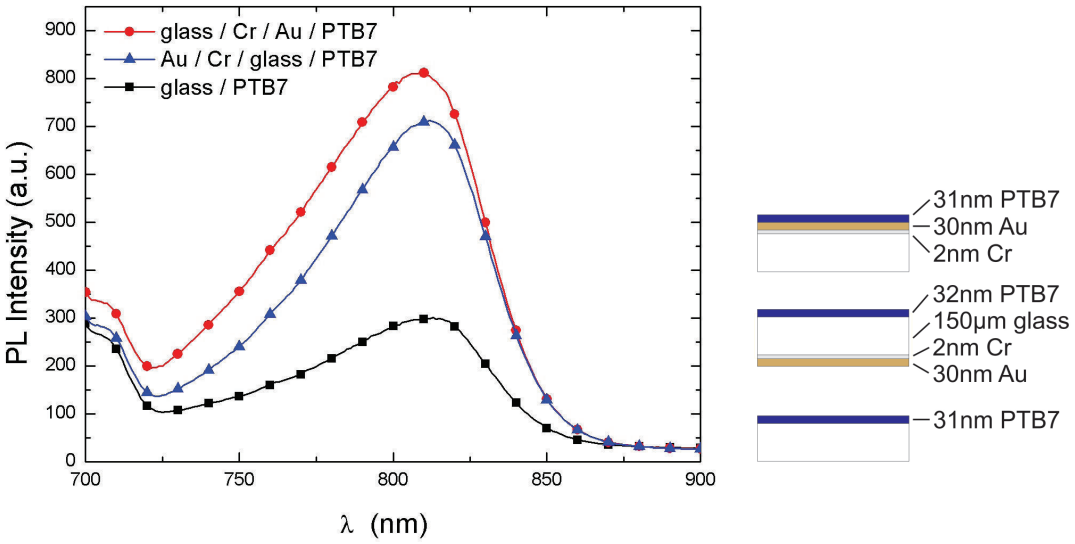

Figure 5.23 – Photoluminescence of a PTB7 film on a metal layer, with and without a dielectric spacer and the photoluminescence of a reference PTB7 film on microscope cover glass excited at a wavelength of 680nm.

The reference PTB7 film on glass shows a PL signal of 300 counts. The PTB7 film with the 150μm spacer produced a signal with 712 counts, which is a 2,4 fold enhancement. The PTB7 film with direct contact to the gold layer produced the highest PL signal of 813 counts, which is a 2,7 times higher signal with respect to the reference.

The amount of fluorescent material on the different samples is with 31nm and 32nm almost the same. The chrome layer is necessary for sufficient adhesion of gold to the glass substrate. This implies for the sample with the spacer, that the order of the metal films on the backside of the glass is changed. For this sample the transmitted light through the PTB7 film and the cover glass hits first the 2nm Cr film and afterwards the 30nm Au layer. This fact as well as absorption in the cover glass reduces intensity of light after reflection at the metal layer compared to the sample without the spacer. To estimate this quantities additional reflection and absorption measurements would be necessary, but it seems likely that the lower PL signal of the sample with the spacer arises because of the slightly different sample configuration. In summary it can be seen that the enhanced PL signal with the metal layer under the PTB7 film is mainly produced by diffuse reflection at the metal.

5.3.3 Sub-wavelength structured metal films coated with PTB7

The PL of samples characterized in section 5.2.6 was recorded with a excitation wavelength of 680nm and the results are shown in **Figure 5.24**.

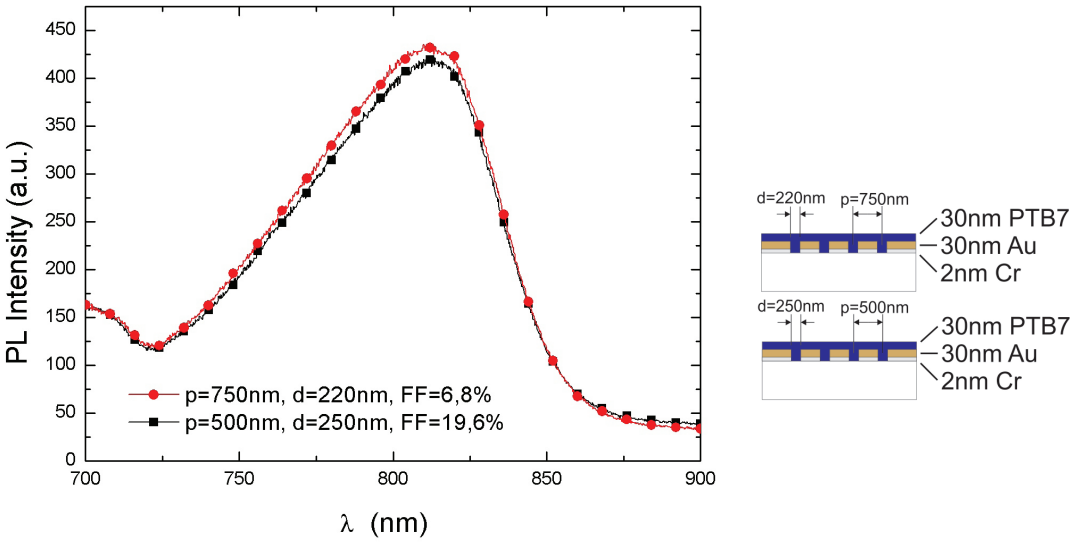

Figure 5.24 – Photoluminescence of a 30nm PTB7 film on different sub-wavelength structured 2nm Cr / 30nm Au layers on glass excited at a wavelength of 680nm.

The PTB7 film on the structure with the 500nm period generated a PL signal with 421 counts and the film on the 750nm period structure showed a higher PL signal of 435 counts.

With the assumption that the holes of the sub-wavelength structured layers get partly filled in the spin coating process, there should be more fluorescence material in the structured metal layers. Comparing the FFs of these structures of 19,6% for the 500nm period and 6,8% for the 750nm period structure, there should be more fluorescence material on the 500nm period structure. But as the results demonstrate, the PL is higher in the sample with the period of 750nm. This leads to the conclusion, that the amount of fluorescence material has only a marginal influence on the PL strength or the assumption that these holes are partly filled is wrong, but in any case there is no influence due to the amount of fluorescence material.

In the case of the 500nm period structure a FF of 19,6% means that 80,4% of the surface is covered with metal and the 750nm period structure has a 93,2% metal coverage. This higher metal coverage provides more metal surfaces for reflection leading to the higher PL signal.

5.3.4 Enhanced photoluminescence due to nanostructure

In **Figure 5.25** the PL signals of PTB7 films on sub-wavelength structured and unstructured metal layers, including a reference on glass are compared. The samples were measured with the same adjustments at the spectrometer and excited at a wavelength of 680nm.

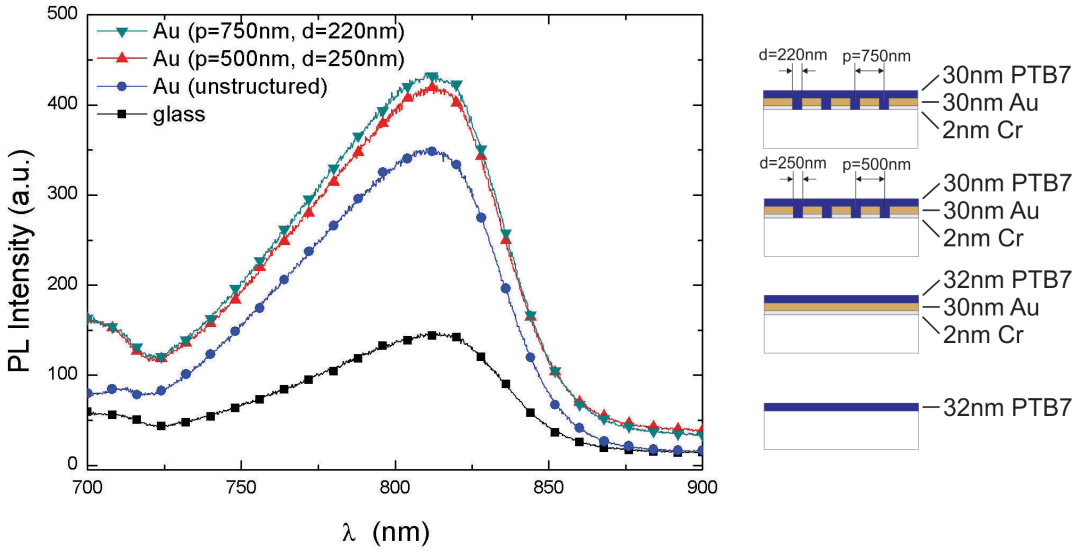

Figure 5.25 – Photoluminescence of PTB7 films on different structured and unstructured 2nm Cr / 30nm Au layers and only on glass excited at 680nm.

Compared to the PTB7 film on glass, the PL signal with a metal layer underneath is enhanced. This enhancement is for the unstructured Au layer 2,4 fold, the sub-wavelength hole array with the period of 500nm 2,9 fold and the structure with 750nm period resulting in a 3 fold enhancement. The thickness of the PTB7 film on the structured metal layers is 30nm, which is 2nm less than the PTB7 film on the unperforated layer. Although, it can be seen that the PL signals of the samples with the structured metal layers underneath show the highest PL values. The unstructured metal layers provide a 100% metal coverage and thus more metal interfaces for reflection. This means the enhanced PL signal cannot be explained through reflexion effects. The only remaining possibility is that the PL signal is enhanced due to increased recombination rates, hence the structure affects the photo physical properties. These results are in accordance with conclusions in literature about increased PL of conjugated polymers using silver nanostructures [77].

It was shown that sub-wavelength structured metal films in the vicinity of PTB7 can change their photo-physical properties. If the physical processes are understood, e.g. radiative and non-radiative decay rates can be changed in a controlled manner which is called Radiative Decay Engineering (RDE) [73]. The interaction of fluorophores with

metallic surfaces can have a number of useful effects, including increased quantum yields, increased photostability, increased distances for resonance energy transfer and decreased lifetimes [74].

Chapter 6

Application of plasmonic electrodes in Organic Solar Cells (OSCs)

Sub-wavelength hole arrays in 2nm Cr / 30nm Au films were incorporated in OSCs as semitransparent plasmonic front electrodes. The sub-wavelength hole arrays were prepared as explained in chapter 4. Bulk heterojunction solar cell composed of the electron-donating semiconducting polymer PTB7 and electron-withdrawing fullerenes PCBM as active layer were used.

To determine the optimal active layer thickness, a series with different spin parameters were prepared on ITO. The active layer consists of PTB7:PCBM blended in a ratio of 1:1, each a concentration of $9\frac{mg}{ml}$ in chlorobenzene. The sample with the spin parameters 1300rpm for 120s and ramp 4, leading to an active layer thickness of about 60nm, showed the highest efficiencies.

Next this configuration was built on a metal sub-wavelength hole array forming a plasmonic front electrode. OSCs with the device structure shown in **Figure 6.1** were prepared.

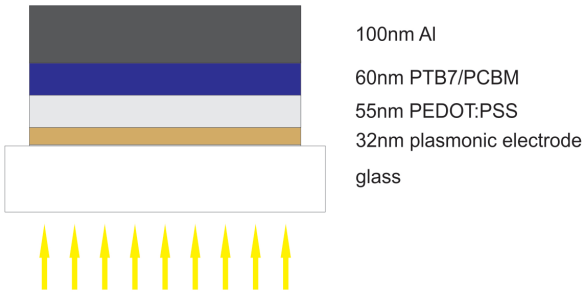

Figure 6.1 – Device structure of OSC with plasmonic front electrode.

The PEDOT:PSS layer on gold were prepared as explained in section 3.4 leading to a layer thickness of 55nm. Then the PTB7:PCBM blend was applied with the before determined spin parameter. Afterwards a 100nm thick Al cathode was thermally evaporated and finally the device was annealed in a tube furnace at 120°C for 10min. One of the fabricated samples can be seen in **Figure 6.2**.

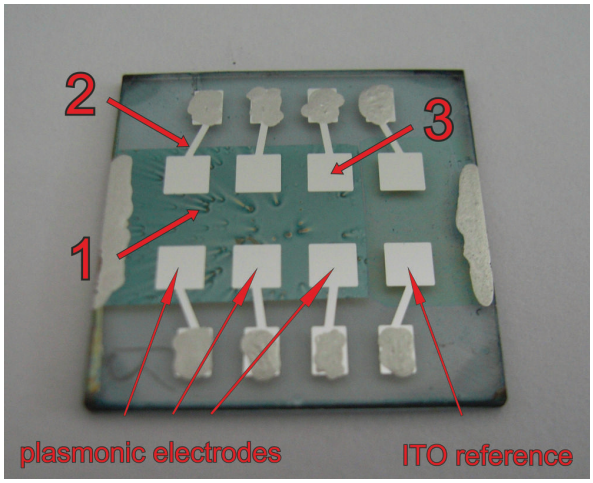

Figure 6.2 – Back side of a sample containing OSCs with plasmonic and ITO front electrodes, each with an area of 3x3mm^2. The possible short circuit reasons are indicated: 1) Impurities in the active layer; 2) Short circuit on the metal-glass intersection; 3) Residual metal on the structure

Unfortunately all OSCs with structured and unstructured Au anodes were short-circuited, but the reference ITO pads were working. This short circuit of the Au anode devices can have various reasons and are indicated in **Figure 6.2**:

1. **Impurities in the active layer**
   As it can be seen in **Figure 6.2** there are impurities in the active layer leading to a non uniform thick active layer. If the layer thickness at some points approaches zero, the Al cathode and the conductive PEDOT:PSS layer are in contact and the device is short circuited.
   On one side this impurities were also present in the PEDOT:PSS layer. This can come from adsorbed impurities prior to spin coating, possibly on the way to the thermal annealing step, which was applied outside the clean room. On the other side this non uniform layer was also seen on ITO. Since the ITO surface was clean this impurities are not dissolved parts of PTB7 due to bad solubility.

2. **Short circuit on the metal-glass intersection**
   The metal at the metal-glass intersection has a sharp edge. This could also produce a short circuit.

3. **Short circuit due to residual metal**
   Remaining metal on the structure, i.e. a residual from the lift-off could, if it is higher than the PEDOT:PSS and the active layer (115nm) produce a short circuit with the top electrode.

To determine the definitive reason why all the produced OSC with Au front electrodes were short circuited, more experiments have to be performed.

Chapter 7

Conclusion

A negative resist was structured by electron beam lithography from which hole arrays in metal films were produced via a lift-off technique. An optimized exposure concerning the time relevant adjustments and the implementation of a special dot exposure mode, made it possible to expose hole arrays with sub-μm periods extending over 3x3mm^2. This takes about 10h with the dot exposure mode compared to 5 days with the usual used area exposure. Metal hole arrays with a period down to 400nm and hole diameters down to 100nm can be fabricated with the dot exposure mode (**Figure 4.7**), but an alternative lift-off procedure has to be used. Further a thermal annealing step improved the quality of the structures (**Figure 4.15**) by reducing residual metal flanks. During the fabrication process of the metal films with sub-wavelength hole arrays, the structured resist forms a 2 dimensional photonic crystal with its special optical properties (**Figure 4.8**).

The optical characterization of the fabricated structures was done by transmission measurements. First unstructured gold coatings with a chrome adhesion layer were investigated. The characteristic interband transmission peak of gold could be identified and the influence of the chrome layer is shown in **Figure 5.4**. For sub-wavelength structured films the influence of the geometric values of the array was discussed. For optical thin metal films, resonances appear at wavelength larger than 600nm (**Figure 5.11**), by lowering the period of the hole array to the sub-μm range. The hole diameter has no influence to the spectral position of resonances. For a optical thick structured metal film, extraordinary transmission was measured and the minimums of the spectrum could be assigned to plasmonic resonances (**Figure 5.12**). With its maximum transmission of 4% the extraordinary transmission of optical thick films is not high compared to the transmission intensities of optical thin metal films. Therefore optical thin metal films should be used as transparent electrodes. However, with transmission measurements only the influence on the far field is measured and near field effects, which may play an important role in thin film devices were not considered.

The metal films were also investigated in combination with PTB7, which is a promising polymer for organic solar cells because of low energy photon absorbance. This is due to the low band gap of the polymer, with the peak of absorption around 670nm. To get an overlap with resonances seen in optical thin structured metal films, this polymer was chosen. First unstructured gold films covered with PTB7 were measured. They showed a higher transmittance as the bare gold film at certain wavelength (**Figure 5.17**). Sub-wavelength structured metal films covered with a PTB7 layer show also this higher transmittance at certain wavelength with the additional PTB7 layer. This wavelength are increased compared to the bare golf film.

Unstructured metal films covered with PTB7 show an enhanced photoluminescence signal. This can be explained mainly by reflection at the metal film. Sub-wavelength hole arrays in metal films coated with a polymer show a further enhanced photoluminescence (**Figure 5.25**). This is believed to originate from increased recombination rates. The change in the photo physical properties could be used in an organic light emitting diode application.

Bulk heterojunction solar cells with a PTB7/PCBM active layer were fabricated on the structured metal films. Unfortunately they were all short circuited. Anyway in the chapter outlook the positive effect of plasmonic structures for organic solar cells will be shown.

Chapter 8

Outlook

An easy way to produce plasmonic structures is to thermally evaporate a thin (<5nm) metal layer on a substrate. This metal forms a discontinuous film and after a thermal annealing step, metal nano-islands accumulate. With the temperature, the thermal deposition rate and specially the amount of evaporated material, the surface plasmon resonance wavelength can be tuned [78].

An experiment to demonstrate the positive effect of plasmonic structures in Organic Solar Cells (OSCs) was performed by Monika Jäger and Roman Trattnig. Therefore CIS Bulk HeteroJunction (BHJ) solar cells were fabricated. A 2nm Ag film was evaporated with a evaporation rate of 0,1 Å/s on a ITO covered float-glass substrate. Afterwards an annealing step at 225°C for 25min at an ambient pressure of 0,5mbar was performed. The resulting metal islands can be seen in the SEM image in **Figure 8.1**. Subsequently the plasmonic structure was coated with a 40nm PEDOT:PSS layer. As active material a polymer CIS blend with a thickness of 90nm was used. The thermally evaporated Al cathode of about 100nm thickness completes the device (**Figure 8.1**).

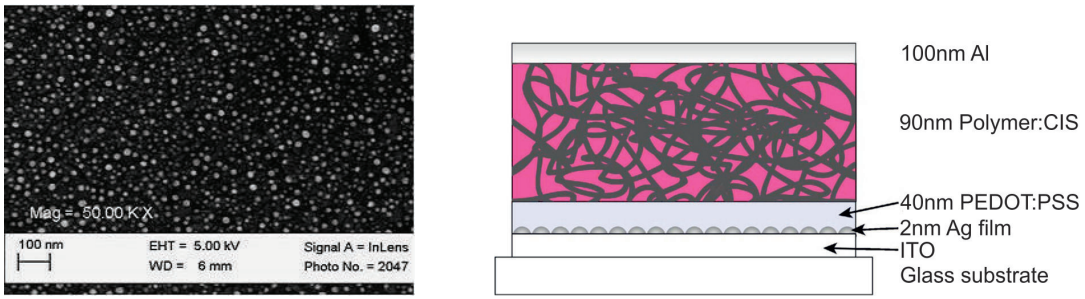

Figure 8.1 – Left: SEM image of 2nm Ag evaporated on ITO after thermal annealing at 225°C for 25min at an ambient pressure of 0,5mbar. Right: Organic Solar Cell (OSC) with plasmonic structure above the ITO layer. Taken from [79] and modified.

The two examples listed in **Table 8.1** demonstrate the enhancement of cell efficiencies. The OSCs are characterized by 4 parameters. The open circuit voltage V_{OC}, is the maximum output voltage without a load, the short circuit current J_{SC} represents the maximum output current with short external contacts and the fill factor FF describing the quality of the diode behavior. The power conversion efficiency PCE is the percentage of incident light power (Φ_e) that is converted to electric power ($PCE = \frac{P_{max}}{\Phi_e}$) with $P_{max} = V_{OC}J_{SC}FF$ the maximum power output of the solar cell.

Table 8.1 – Two examples of increased PCE with Ag plasmonic structures. The current-voltage curves of example 1 is illustrated in **Figure 8.2** and example 2 in **Figure 8.3**
V_{OC} ... Open circuit voltage
J_{SC} ... Short circuit current
FF ... Fill factor
PCE ... Power conversion efficiency

		V_{OC} / V	J_{SC} / $\frac{\text{mA}}{\text{cm}^2}$	FF / %	PCE / %
Example 1	Reference	0,52	5,72	38,53	1,15
	with Ag	0,52	7,32	44,23	1,68
Example 2	Reference	0,54	5,78	48,70	1,52
	with Ag	0,54	6,23	55,66	1,87

In both examples, it can be seen that V_{OC} has the same value with the additional thin Ag layer, but J_{SC} and the FF increase significant leading to a higher PCE. In example 1 the PCE increases from 1,15% to 1,68% with the plasmonic structure, which is an enhancement of 46% and in example 2 the PCE increases from 1,52% to 1,87% which is an enhancment of 23%. The current-voltage curves of example 1 are shown in **Figure 8.2**. Illustrated are the dark situation and illuminated with a solar simulator of a spectral irradiance AM1,5G with $100\frac{mW}{cm^2}$ respectively.

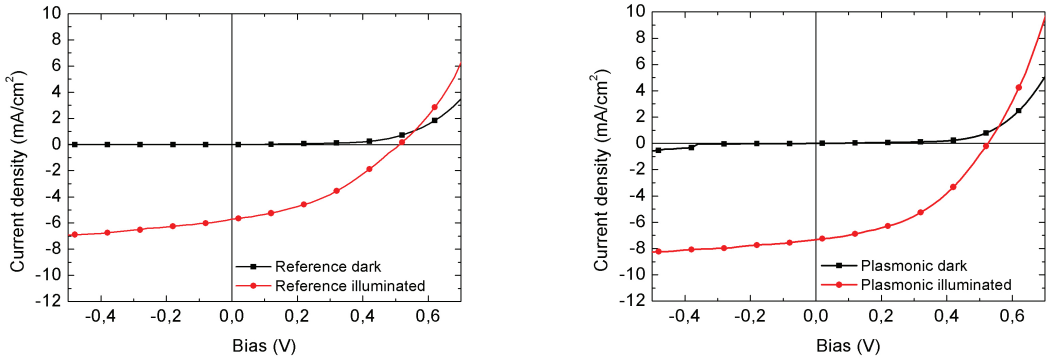

Figure 8.2 – *Example 1:* Current-voltage curves, dark and illuminated with AM1,5G and $100\frac{mW}{cm^2}$. Left: Reference, right: With additional Ag plasmonic structure.

The increased J_{SC} and FF can be for various reasons. This could be an increased absorption due to the high electric fields in the vicinity of plasmonic structures, as well as improved

charge transportation. If the light absorption in the active material is higher, a thinner active layer could further enhance efficiencies.
For the second example the current-voltage curves for the illuminated situation are compared and additional an Incident Photon to Charge Carrier Efficiency (IPCE) spectrum is shown in **Figure 8.3**. An IPCE spectrum shows the ratio between the number of generated charge carriers to the number of photons incident on a solar cell as a function of the wavelength.

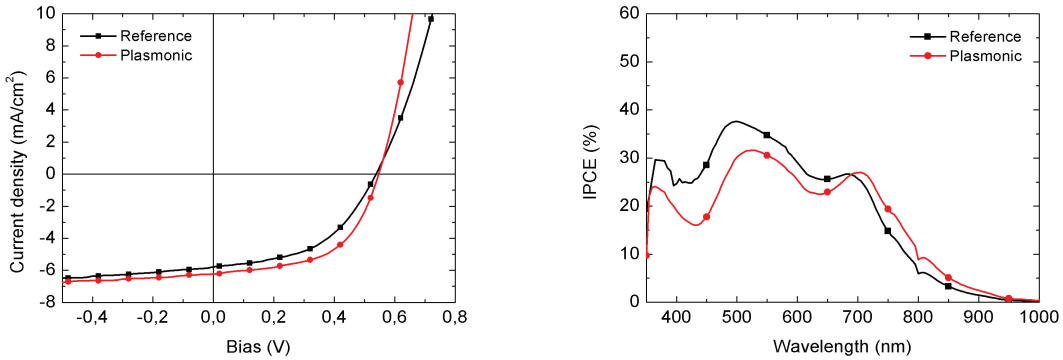

Figure 8.3 – *Example 2:* Left: Current-voltage curves of reference and plasmonic OSC illuminated with AM1,5G and $100\frac{mW}{cm^2}$ Right: IPCE of the reference and plasmonic OSC.

The increased I_{SC} and FF with the additional plasmonic structure can be seen in the current-voltage curves. The IPCE spectrum shows a higher fraction of generated charge carriers at wavelength larger than 690nm. This increased photoconversion in the red part of the spectrum leads to enhanced efficiencies.

It was shown that plasmonic structures incorporated in organic solar cells can lead to enhanced efficiencies. The physical processes involved are not completely understood yet and further experiments are necessary.

Bibliography

[1] T. W. Ebbesen *Letters to Nature*, **1998**, 391, 667-669

[2] F. J. Garcia-Vidal *Reviews of modern Physics*, **2010**, 82, 730

[3] Alexandre G. Brolo, *Langmuir*, **2004**, 20, 4813-4815

[4] John T. Bahns, *Journal of Physical Chemistry C*, **2009**, 113(26), 11190-11197

[5] Alexandre G. Brolo, *Journal of the Am. Chemical Society*, **2005**,127, 14936-14941

[6] C. Liu, *Applied Physics Letters*, **2005**, 86, 143501

[7] Thomas H. Reilly, *Applied Physics Letters*, **2008**, 92, 243304

[8] Gang Li, *Nature Materials*, **2005**, 4, 364

[9] B. Zimmermann, *Solar Energy Materials and Solar Cells*, **2007** , 91, 374

[10] C.G. Granqvist, *Thin Solid Films*, **2002**, 411, 2

[11] Y. Galagan, *Solar Energy Materials and Solar Cells*, **2010**, 95, 1339

[12] Izak Kapilevich, *Photovoltaic Specialists Conference 34th IEEE*, **2009**, 2060

[13] E.T. Yu, *Mrs Bulletin*, **2011**, 36, 427

[14] Ji Hwang Lee, *Organic Electronics*, **2009**, 10, 416-420

[15] Fang-Chung Chen, *Applied Physics Letters*, **2009**, 95, 013305

[16] Jyh-Lih Wu, *ACS Nano*, **2011**, 5(2), pp 959-967

[17] J. Parsons, *Physical Review B*, **2009**, 79, 073412

[18] P.B. Johnson *Physical Review B*, **1972**, 6, 4374

[19] Edward D. Palik *Handbook of Optical Constants of Solids II*, Academic Press Inc, **1998**, 384

[20] Heinz Raether, *Surface plasmons on smooth and rough surfaces and on gratings*, Springer, **1988**, 4-7

[21] Nathan Charles Lindquist, *Engineering metallic nanostructures for surface plasmon resonance sensing*, Dissertation University of Minnesota, **2010**, 12 and 16

[22] Joel Henzie, *Annu. Rev. Phys. Chem.*, **2009**, 60, 149

[23] William L Barnes, *J. Opt. A, Review Article*, **2006**, 8, 88

[24] Richard B. M. Schasfoort, *Handbook of surface plasmon resonance*, Royal Society of Chemistry, **2008**, 20

[25] Qing Cao, *Physical Review Letters* **2002**, 88(5) , 57403

[26] F. Przybilla, *Journal of Optics A*, **2006**, 8, 460

[27] J M Pitarke, *Reports on Progress in Physics*, **2007**, 70, 12

[28] Bruce W. Smith, *Proc. of SPIE*, **2009**, 7274

[29] James G. Goodberlet, *J. Vac. Sci. Technol. B*, **2001**, 19(6), 2500

[30] Johannes Kofler, *Fabrication and investigation of micro - and nano - fluidic devices: Fundamental aspects and sensor applications*, Master Thesis TU-Graz, **2011**, 12

[31] www.nanophys.kth.se/nanophys/facilities/nfl/manual/wfalign/align.html, 30.7.2011

[32] Gary Wiederrecht, *Handbook of Nanofabrication*, First Edition, Elsevier B.V., **2010**, 122-123

[33] http://www.microchemicals.com/technical_information/substrate_cleaning_adhesion_photoresist.pdf, 20.9.2011

[34] http://www.microchemicals.de/product_data_sheets.html, 20.9.2011

[35] Ronald R. Willey, *Practical Design and Production of Optical Thin Films*, Second Edition, CRC Press, **2002**, 283

[36] http://nanodevices.nl/facilities/equipment/123-raith-e-line-ebl, 20.7.2011

[37] http://pluggedin.kodak.com/pluggedin/post/?id=655003, 20.7.2011

[38] http://ebookbrowse.com/e-beam-lithography-pdf-d102696749, 20.7.2011

[39] Tennyson Smith, *Journal of Colloid and Interface Science*, **1980**, 75(1), 51-55

[40] Hannoch Ron, *Langmuir*, **1998**, 14, 1116-1121

[41] David Brandon, *Microstructural Characterization of Materials*, Second Edition, John Wiley and Sons, **2008**, 283

[42] D. M. Koller, *Applied Physical Letters*, **2008**, 92, 103304

[43] D. M. Koller, *Nature Photonics*, **2008** , 2, 684-687

[44] http://www.microchemicals.com/technical_information/softbake_photoresist.pdf, 30.7.2011

[45] Michael Wang, *Lithography*, First Edition, Intech, **2010**, 258

[46] T. J. Stark, *J. Vac. Sci. Technol. B*, **1993**, 11(6), 2367

[47] www.microchemicals.com/technical_information/lift_off_photoresist.pdf, 28.7.2011

[48] Haifang Yang, *Microelectronic Engineering*, **2008**, 85, 814-817

[49] http://en.wikipedia.org/wiki/Chromium, 21.9.2011

[50] http://en.wikipedia.org/wiki/Gold, 21.9.2011

[51] A. Mooradian, *Physical Review Letters*, **1969**, 22, 185-187

[52] Catherine Bréchignac, Philippe Houdy and Marcel Lahmani, *Nanomaterials and nanochemistry*, Springer-Verlag, **2007**, 208

[53] Tobby Bert Brandt, *Optische Leitfähigkeit dünner Goldfilme im infraroten Spektralbereich*, Dissertation Universität Stuttgart, **2008**

[54] David Richards, *Nano-optics and near-field optical microscopy*, Artech House, **2009** ,178

[55] O M Piciu, *IMechE Part N: J. Nanoengineering and Nanosystems*, **2008**, Vol.222

[56] Vladimir Kochergin, *Omnidirectional optical filters*, Kluwer Academic Publishers, **2003**, 71

[57] John A. Rogers, Hong H. Lee, *Unconventional nanopatterning techniques and applications*, John Wiley and Sons, **2009**, 524

[58] J. Parsons, *Proc. SPIE Nanophotonics II*, **2008**, 6988, 69880Y

[59] Julia Braun *Physical Review Letters*, **2009**, 103(20), 203901(4)

[60] H. A. Bethe, *Physical Review Letters*, **1944**, 66, 163-182

[61] James V. Coe, *Annual Review of Physical Chemistry*, **2008**, 59, 179-202

[62] K. J. Klein Koerkamp, *Physical Review Letters*, **2004**, 92(18), 183901

[63] K. L. van der Molen, *Applied Physical Letters*, **2004**, 85(19), 4316-4318

[64] J. Bravo-Abad, *Nature Physics*, **2006**, 2, 120-123

[65] http://www.delta-technologies.com/Products.asp?C=13, 11.9.2011

[66] W.H. Lee, *Thin Solid Films*, **2010**, 518, 7450-7454

[67] Brendan O'Conner, *Applied Physics Letters*, **2008**, 93, 223304

[68] http://www.1-material.com/node/48, 15.9.2011

[69] By Yongye Liang, *Advanced Energy Materials*, **2010**, 22, E135

[70] Ulrich C. Fischer, *Applied Physics Letters*, **2002**, 80(20), 3715-3717

[71] E. G. Bortchagovsky, *Applied Physics Letters*, **2002**, 117(11), 5384-5392

[72] Noritsugu Kometani, *American Chemical Society*, **2001**, 17, 578-580

[73] Joseph R. Lakowicz, *Analytical Biochemistry* , **2002**, 301, 261-277

[74] Joseph R. Lakowicz, *Principles of Fluorescence Spectroscopy*, Third Edition, Springer, **2006**, 841

[75] James A. Hutchison, *Angew. Chem. Int. Ed.* **2011**, 50, 2085-2089

[76] F. Przybilla, *Journal of Optics A*, **2006**, 8, 458-463

[77] Hong-Ju Park, *Applied Physic Letters*, **2007**, 90, 161107

[78] R. Gupta, *J. of applied Physics*, **2002**, 92(9), 5264

[79] Anthony J. Morfa, *Applied Physic Letters*, **2008**, 92, 013504-2